11-14-2019

Structural Basis for Chloroperoxidase Catalyzed Enantioselective Epoxidations and Mechanisms of Selected Anticancer Drug Induced Apoptosis

Yongjian Guo
Florida International University, yguo018@fiu.edu

FLORIDA INTERNATIONAL UNIVERSITY

Miami, Florida

STRUCTURAL BASIS FOR CHLOROPEROXIDASE CATALYZED

ENANTIOSELECTIVE EPOXIDATIONS AND MECHANISMS OF SELECTED

ANTICANCER DRUG INDUCED APOPTOSIS

A dissertation submitted in partial fulfillment of

the requirements for the degree of

DOCTOR OF PHILOSOPHY

in

BIOCHEMISTRY

by

Yongjian Guo

2019

To: Dean Michael R. Heithaus
     College of Arts, Sciences, and Education

This dissertation, written by Yongjian Guo, and Structural Basis for Chloroperoxidase Catalyzed Enantioselective Epoxidations and Mechanisms of Selected Anticancer Drug Induced Apoptosis, having been approved in respect to style and intellectual content, is referred to you for judgment.

We have read this dissertation and recommend that it be approved.

_____
Yuan Liu

_____
Stanislaw F. Wnuk

_____
Manuel Alejandro Barbieri

_____
Xiaotang Wang, Major Professor

Date of Defense: November 14, 2019

The dissertation of Yongjian Guo is approved.

_____
Dean Michael R. Heithaus
College of Arts, Sciences and Education

_____
Andrés G. Gil
Vice President for Research and Economic Development
and Dean of the University Graduate School

Florida International University, 2019

DEDICATION

I dedicate this dissertation to my mother Xia Liu and my father Qinglong Guo.

Without their patience, understanding, support, and most of all love, the

completion of this work would not have been possible.

ACKNOWLEDGMENTS

I would like to express my deep and sincere gratitude to my research supervisor, Dr. Xiaotang Wang, for giving me the opportunity to do research and providing invaluable guidance throughout this research. His vision, sincerity and motivation have deeply inspired me. He has taught me the methodology to carry out the research and to present the research works as clearly as possible. It was a great privilege and honor to work and study under his guidance.

I would also like to thank my other committee members, Dr. Stanislaw F. Wnuk, Dr. Yuan Liu, and Dr. Manuel Alejandro Barbieri, for their constructive advice, professional assistance, firm support and helping me to succeed in my personal life. I want to acknowledge my lab mates and friends, Dr. Elwood Kwong Lam, Dr. Qinghao He, Xiaoqing Tang, and Zifang Deng, for their helpful discussion and pleasant research environment. I want to give special thanks to my good friends, Cong Gu, Reipeng Lei and Li Mo, for their assistance during my time as graduate students.

Finally, I would like to acknowledge the Department of Chemistry and Biochemistry at FIU for the financial support.

ABSTRACT OF THE DISSERTATION

STRUCTURAL BASIS FOR CHLOROPEROXIDASE CATALYZED

ENANTIOSELECTIVE EPOXIDATIONS AND MECHANISMS OF

SELECTED ANTICANCER DRUG INDUCED APOPTOSIS

by

Yongjian Guo

Florida International University, 2019

Miami, Florida

Professor Xiaotang Wang, Major Professor

Chloroperoxidase (CPO), a member of the heme peroxidase family, has diverse catalytic activities toward a broad range of substrates. CPO also catalyzes reactions typical of traditional heme peroxidases, catalases, and cytochrome P450 enzymes. To overcome these shorting comings of the protein, we investigate the fabrication and characterization of chloroperoxidase (CPO) and glucose oxidase (GOx) on the surface of MGO. Chapter 2 of this dissertation demonstrates the feasibility of co-immobilizing CPO and GOx onto MGO and the potential of MGO-GOx-CPO in environmental applications. The heme active site structure has also been thought to be responsible for the enantioselectivity of CPO. Chapter 3 of this dissertation investigates the structural factors that contribute to CPO's stereoselectivity in catalyzing epoxidation reactions. The characterization of CPO-substrate complex will be carried out using UV-Vis

spectrophotometry and nuclear magnetic resonance (NMR) spectroscopy. We will focus on understanding the mechanism of CPO-catalyzed enantioselective epoxidation and structure-activity relationship of CPO.

Non-small-cell lung carcinoma (NSCLC) continues to be a vital human healthcare problem worldwide for its high incidence and consequent mortality rate. We investigated the anticancer effect of LZ-101, a novel derivative of danofloxacin, against non-small-cell lung cancer and the underlying mechanisms. We demonstrated that LZ-101 induced mitochondrial-mediated apoptosis by increasing Bax/Bcl-2 ratio, loss of mitochondrial membrane potential ($\Delta\Psi_m$), cytochrome c (Cyt c) release and apoptosis-inducing factor (AIF) transposition in A549 cells. Moreover, we found that LZ-101 increased the stability of FOXO3a by blocking autophagy-dependent FOXO3a degradation.

Enhanced energy metabolism plays important roles in the growth and survival of cancer cells. Here, we investigated the mechanisms of a newly synthesized flavonoid, GL-V9, in the inhibition of glycolysis and the induction of apoptosis of human breast cancer cell lines MDA-MB-231 and MCF-7 cells. GL-V9 not only downregulate the expression of HKII in MDA-MB-231 and MCF-7 cells, but also induce dissociation of HKII from voltage-dependent anion channel (VDAC) in mitochondria, resulting in glycolytic inhibition and mitochondrial-mediated apoptosis. Our work demonstrates the significance of metabolic regulator in cancer growth and offers fresh insight into the molecular basis for

the development of flavonoid as novel agents for the treatment of breast

carcinoma.

TABLE OF CONTENTS

LIST OF TABLES

LIST OF FIGURES

xviii

LIST OF ABBREVIATIONS

ABBREVIATION	FULL NAME
Ala	Alanine
Asn	Asparagine
COSY	Correlation spectroscopy
CPDO	1,3-cyclopentanedione
CPO	Chloroperoxidase
CYP1A1	Cytochrome P450, family 1, member A1
Cys	Cysteine
DSS	4,4-dimethyl-4-silapentane-1-sulfonic acid
ee	enantiomeric excess
ELISA	Enzyme-linked immunosorbent assay
ENDOR	Electron nuclear double resonance
EPR	Electron paramagnetic resonance
Glu	Glutamic acid
GROMACS	Groningen Machine for Chemical Simulations
GROMOS	Groningen Molecular Simulation
His	Histidine
Ile	Isoleucine
K_D	The dissociation constant
LC-MS	Liquid chromatography-mass spectrometry

Leu	Leucine
MCD	Magnetic circular dichroism
MD	Molecular dynamic
MM	Molecular Mechanics
MP2	Second-order Moller-Plesset perturbation theory
NMR	Nuclear magnetic resonance
NOE	Nuclear overhauser effect
P450 BM3	Cytochrome P450 BM3
P450	Cytochrome P450
Pca	Pyroglutamic acid
PDB	Protein data bank
Phe	Phenylaniline
PME	Particle mesh Ewald method
QM	Quantum Mechanics
RI	Resolution-of-the-identity
RMSD	Root-mean-square deviation
Rz	Reinheitzahl
SDS	Sodium dodecyl sulfate
SPC	Simple point charge
T_1	Longitudinal relaxation time
UV-Vis	Ultraviolet-Visible

Val   Valine

VPO   Versatile peroxidase

WT   Wild-type

CHAPTER I.

INTRODUCTION

1.1 Proteins and Peroxidases Containing Heme Prosthetic Group

Heme-thiolate proteins are a group of hemoproteins whose prosthetic group is protoheme (Figure 1) with a thiolate anion of a cysteine residue as the axial ligand. They constitute one of the two major hemoprotein groups found in living organisms; the other is the "heme–imidazole protein" group that includes hemoglobin [1].
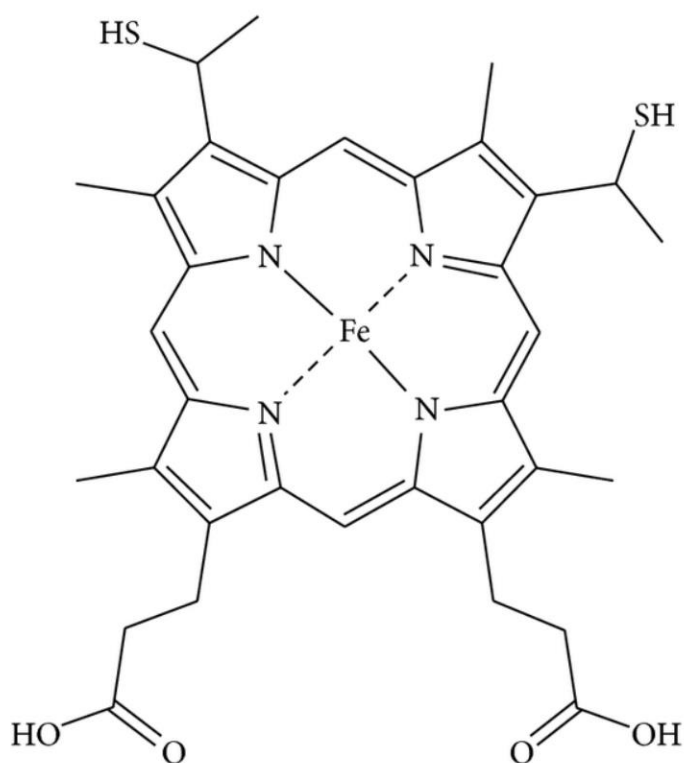
Figure 1.1 Structure of Heme-thiolate proteins (Iron protoporphyrin IX).

Cytochrome P450 was the first hemoprotein found to have a 450-nm absorption peak in the carbon monoxide-binding spectrum. However, we now know that cytochrome

1

P450 is a member of the growing family of heme-thiolate proteins, in which nitric oxide synthase is another important member. The major physiological function of heme-thiolate proteins is apparently the activation of molecular oxygen for a various of oxygenase reactions [2]. Chloroperoxidase (CPO), a member of the heme peroxidase family, has diverse catalytic activities toward a broad range of substrates. Peroxidase is a striking group of enzymes that can catalyzes the oxidation of many substrates using peroxide as a co-substrate. These enzymes have been discovered and used for decades. Among the peroxidases, CPO has attracted more attention for deciphering the mechanism of its unique reactions and for using this enzyme to serve humanity life. In addition to catalyzing halogenation reactions involved in the biosynthesis of halogen-containing compounds, CPO also catalyzes reactions typical of traditional heme peroxidases, catalases, and cytochrome P450 enzymes [3]. The versatility of CPO has long been attributed to the unique structural components of the protein environment that constitute the heme active site, particularly the identity of the axial heme ligand and amino acid residues distal to the heme iron. The heme active site structure has also been thought to be responsible for the enantioselectivity of CPO.

1.2 NMR of Paramagnetic Systems

The completion of the human genome, together with that of an increasing number of other living systems including pathogens, poses problems in structural biology preceding the challenge of high throughput generation of 3D structures of gene products, namely proteins. The biological NMR community, in particular, needs to overcome

several intrinsic limitations of the technique including the presence of paramagnetic metals in the molecule, which may be a source of severe line broadening [4].
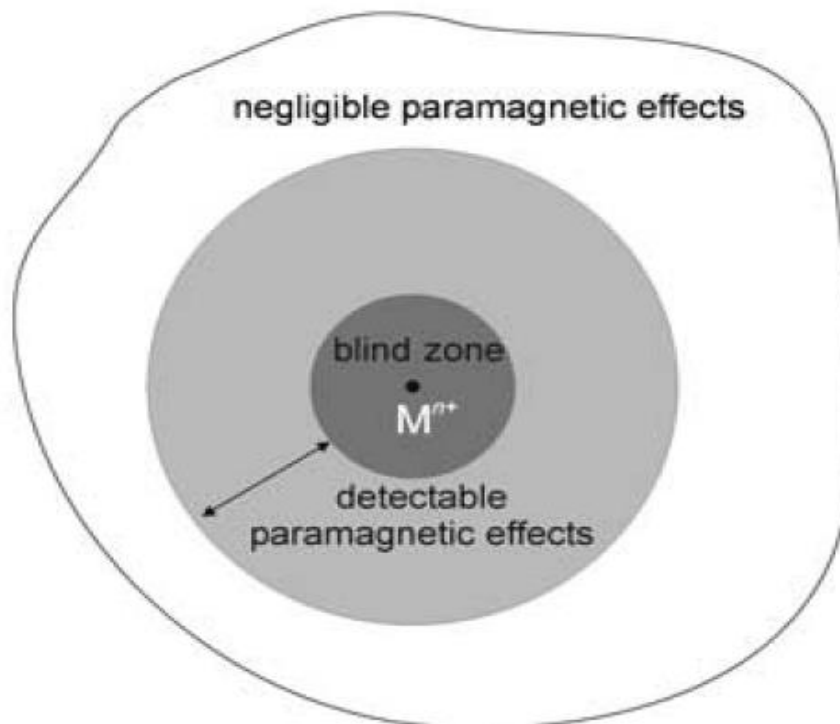
Figure 1.2 The inner sphere centered on the paramagnetic metal ion is a blind-zone, as proton NMR signals are too broad to be detected. Outside this sphere, there is another sphere indicating the region where NMR signals are visible and still affected by paramagnetism, so that information can be extracted on their position with respect to the metal ion [4].

While it has long been recognized that both the hyperfine shifts and paramagnetic relaxation can provide unique and valuable information on the electronic, magnetic, and molecular structural properties of the active site of paramagnetic metalloproteins, access to this information has been thwarted by the absence of a systematic and reliable strategy for assigning the resonances to specific nuclei in the molecule. Thus, the initial excitement about and interest in NMR spectroscopy of paramagnetic proteins in the late 60s to middle 70s of the last centuries faded somewhat on the full realization of the

apparent barriers to unambiguous signal assignment. The early strategies for assigning hyperfine-shifted resonances in a paramagnetic protein relied on a number of methods, of which most had only a very limited applicability.

As the estimated fraction of metalloproteins is about one third of the total proteins, and a significant number of these are paramagnetic, the issue is not an irrelevant one. The increasing number of NMR groups that have begun tackling paramagnetic systems in the last few decades. It has been increasingly recognized that, besides contributing to line broadening, the electron nucleus interactions contain useful structural information. The first protein solution structure was published in 1985 and since then NMR spectroscopy has developed through diamagnetic molecule applications. The broadening due to Para magnetism seemed an insurmountable obstacle for structure determination. However, some groups continued to deepen the understanding of the effects of hyperfine coupling in NMR spectroscopy and simultaneously to exploit technological advancements to increase the signal-to-noise ratio of paramagnetic-system spectra. Eventually, a protocol for solving the structure of a paramagnetic metalloprotein was reported in 1994 and since then many examples have appeared in the literature [5]. The paramagnetic property of the metalloprotein also serves as an intrinsic probe for elucidating the structural properties of enzyme-substrate complexes as will be exploited in Chapter 3 of this dissertation.

1.3 NMR Application to Heme-Peroxidases

Every metal ion has its own peculiarities and should be regarded as special cases.

For example, Low-spin iron (iii): its sphere of non-observability for proton NMR spectroscopy is quite narrow and its compounds represent the most popular class of paramagnetic compounds studied by NMR spectroscopy. Many of the relevant effects that the presence of paramagnetic metals has on the behavior of the protein nuclei have to do with the metal magnetic susceptibility. Previous literature has reported that the presently available homonuclear NMR methods allow productive investigation of the active site of ~40 kDa high-spin ferric heme enzymes, albeit with a more limited information content relative to similar studies on the low-spin, cyanide-inhibited derivatives [6]. Identification of peripheral aromatic contacts allows the determination of the zero-field splitting constant by their characteristic temperature dependence if a homology model is available. It is expected that changes in shifts in resting state peroxidases upon systematic perturbation, such as substrate binding (or point mutation), should be accessible to interpretation in terms of the electronic structure of the heme iron [6].

1.4 CPO Catalyzed Reactions

The crystal structure of CPO reveals the unique structural feature of this versatile biocatalyst [2]. CPO contains a single polypeptide chain of 299 amino acids that folds into 8 helixes, named A~H, as shown in Figure 3 [7].
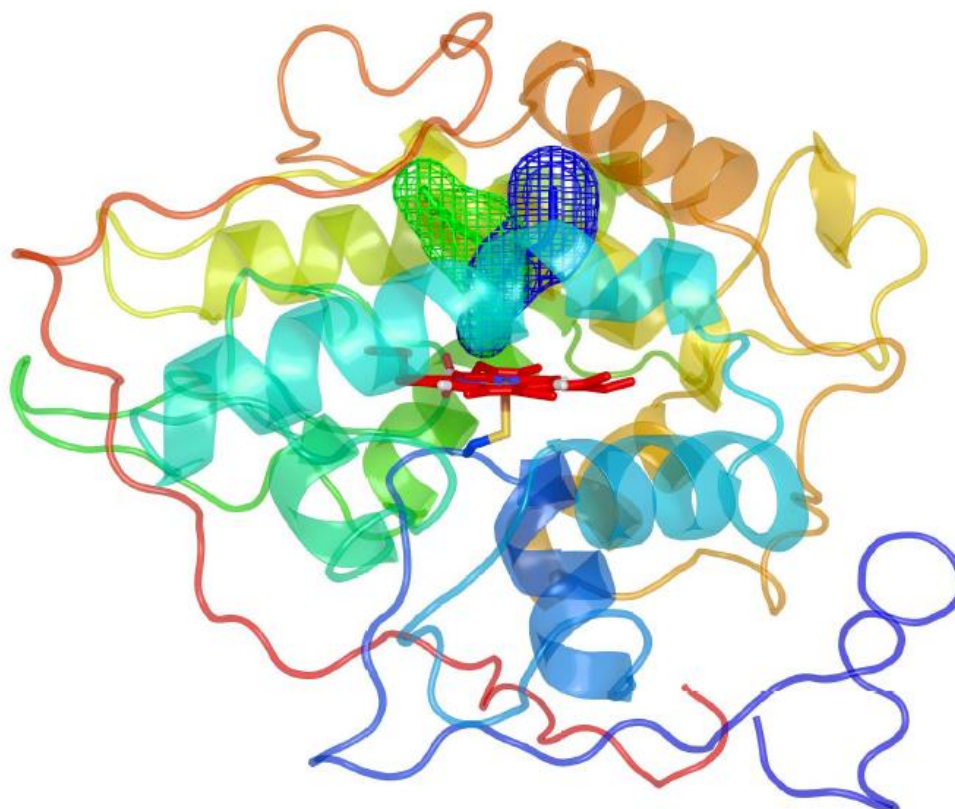
Figure 1.3 The crystal structure of Chloroperoxidase showing the two channels (narrow, green, wide, blue) that connect the heme active site to the surface.

Chloroperoxidase(CPO) is unusually versatile, capable of catalyzing not only the reactions typical of peroxidases but also those of catalases and monooxygenases, as well as halogenation reactions. The structure of CPO shares many common features with that of cytochrome P450 with a merged region containing the proximal ligand and ligand binding site distal to the heme. However, the structure of CPO also displays essential differences from other heme peroxidases and cytochrome P450. Thus, the catalytic activity of CPO is more auspicious especially in making chiral synthons such as epoxides. Chiral epoxides are very important intermediates for the synthesis of optically pure complex molecules, particularly biologically active compounds [8]. Catalytic asymmetric epoxidation of alkenes is one of the most powerful strategies for

the preparation of enantiomerically pure epoxides. A better understanding of the mechanisms of CPO catalyzed enantioselective oxidations would provide guidance to design mutant proteins that display improved catalytic activity and enantioselectivity.

1.5 The Mechanism of CPO Catalyzed Reactions

Chloroperoxidase can catalyze various reactions including halogenation, monooxygenation, dismutation, and peroxidation. An important aspect of chloroperoxidase catalysis is the mode of binding of the substrate to the active site [9]. Compound I is an oxidized ferryl heme with a porphyrin radical intermediate, which was found in the catalytic cycle of many peroxidases and P450s. The reactive species could be generated by reacting the resting or ferric state of CPO with a peroxide molecule. Compound I can go through different pathways in the catalytic cycle [10]. For example, during halogenation reactions, compound I is a strong oxidant and can react with chloride ions to produce HOCl (Fig 1.4).
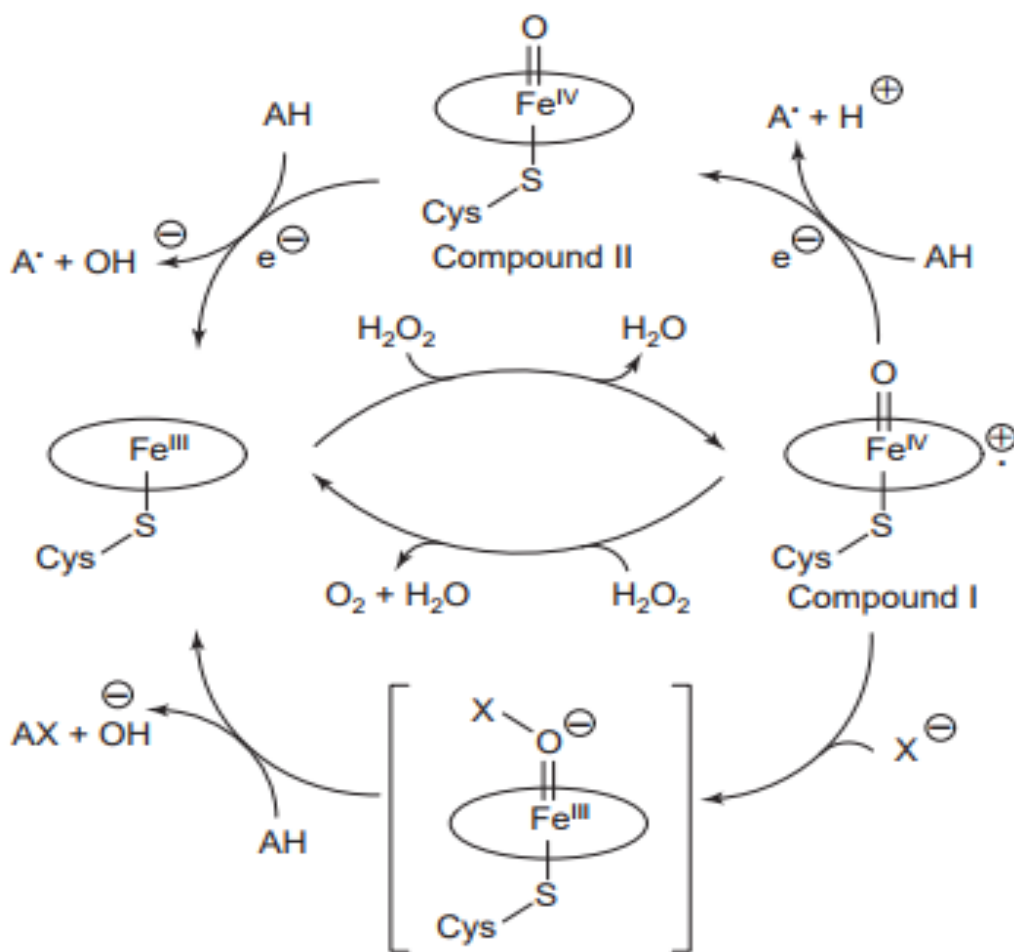
Figure 1.4 The catalytic cycle of chloroperoxidase (CPO). X represents Cl, Br or I involved in the halogenation pathway [11]

During this process, Compound II, an oxo-ferryl heme, will form after one electron reduction of Compound I [12]. After another one-electron reduction Compound II is returned to ferric state.[11]. The lack of stereospecificity in the halogenation reactions catalyzed by CPO is in agreement with the participation of an "enzyme-free" halogenating species, the details remains to be a matter of debate.

1.6 Applications of CPO

1.6.1 Enhancing the Applicability of CPO

Enzyme catalysis has drawn an increasing amount of attention in both academia and industry because of its large potential in the manufacture of value-added fine chemicals, pharmaceuticals, flavors, and fragrances under mild conditions with high yield and selectivity [13]. Chloroperoxidase has long been recognized as a versatile catalyst for its powerful and diverse catalytic activities [14, 15]. However, like most biological catalysts, practical applications of CPO are often hampered by the difficulty in regenerating the active enzyme and the lack of long-term operational stability of the protein, especially in the presence of high concentrations of peroxide and at elevated temperatures [16].

To overcome these drawbacks, tremendous efforts have been made to immobilize enzymes on appropriate supporting materials [17]. However, enzyme bound on a support often display lower activity than that of the free enzyme because of enzyme deactivation during immobilization and/or increased transfer resistance of substrate in the support. Graphene oxide/iron oxide (MGO) composites have been regarded as one of the most promising supporting materials for the immobilization of enzymes. The magnetism of the composites allows easy separation of the enzyme for reuse while the unique surface property of the composites significantly enhances the catalytic performance of the enzyme. The improved enzyme performance can be attributed to such factors as enhanced enzyme purity [18], stability (including the possibility of

enzyme reactivation, especially for multimeric enzymes, such as glucose oxidase), activity, selectivity, decreased inhibition and mass transport limitations [19, 20].

Cascade reactions taking place in one pot offer the second enzyme the opportunity to act on a higher concentration of its substrate. Meanwhile, cascade reactions significantly reduce the length of time required for the full reaction course. However, cascade reactions have at least these two shortcomings. First, since both enzymes are immobilized on the same surface, the loading amount of enzyme becomes restricted. Second, when one enzyme is inactivated, the other will have to be discarded even if it is still fully active [21].

So far various support and composite materials, such as synthetic resins, biopolymers, and inorganic solids (mesoporous silicas or zeolites) have been developed. The properties of the support materials define their interaction with the enzyme and are thus critical to enzyme activity after immobilization. Therefore, nanostructure composite and hybrid materials have gained increasing attention because of their potential to improve the efficiency of enzyme immobilization [22] as exemplified in Chapter 2 of the dissertation.

1.6.2 Environmental Applications

A number of oxidative enzymes from bacteria, fungi and plants have been reported to play an important role in numerous waste treatment applications. Peroxidases and/or phenoloxidases act on specific recalcitrant pollutants by precipitation or transformation of the pollutants to other products and permitting a better final treatment of the

waste[23]. Improvement in the useful life and thereby a reduction in treatment cost has been accomplished through enzyme immobilization.

Horseradish peroxidase, lignin peroxidase and manganese peroxidase mineralize a variety of recalcitrant aromatic compounds. Immobilization of these enzymes on porous ceramic supports or resins did not adversely affect their stability and showed a good potential for degradation of environment persistent aromatics.

According to a recently published work, CPO has been reported to oxidize several phenolic compounds [23] . In addition, oxidation of ethanol to aldehyde and oxidation of chloride ions occurred [24]. Recently, the application of free form of CPO was reported in many kinds of oxidation processes [25]. The enzyme was purified and immobilized on an aminopropyl glass, on talc or on reverse micelles [1, 25]. A combined electrocatalytic approach using immobilized CPO and a glucose electrode has been developed for the measurement of chlorophenol congeners.

There is a growing recognition that enzymes can be used in many remediation processes to target specific pollutants for treatment. Recent biotechnological advances have allowed the production of cheaper and more readily available enzymes through better isolation and purification procedures [26-28]. The potential advantages of the enzymatic treatment as compared with conventional treatments include: application to recalcitrant materials, operation at high and low contaminant concentrations over a wide pH, high temperature and salinity range, needs of biomass acclimatization and the

easy control process among others. The most recent research in this area have focused on the development of enzyme processes for the treatment of wastewater [26].

1.6.3 Pharmaceutical Applications

Chloroperoxidase is able to catalyze a broad spectrum of stereoselective hydroxylation, sulfoxidation and epoxidation reactions. The substrate specificity of chloroperoxidase for chiral epoxidation of mono- and disubstituted alkenes has been well documented as summarized in Figure 1.5. Chloroperoxidase is able to efficiently utilize alkenes with chain lengths of nine or fewer carbon atoms except for monosubstituted terminal olefins which often function as reversible suicide inhibitors of the enzyme. Excellent substrates are created by cis-1 methyl and 2-methyl substitutions on the olefinic double bond. Kinetic, enantioselectivity and epoxide yield data have been obtained on a series of brominated and unbrominated methallyl alkenes and substituted styrenes. The results indicate that methallyl alkenes and styrenes can function as good substrates [29].
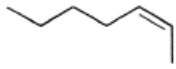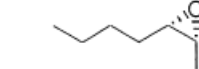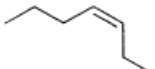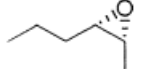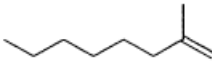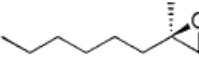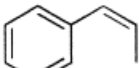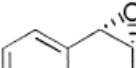
entry	alkene	major epoxide	ee (%)	conversion (%)	yield (%)
1			96	100	78
2			97	17	12
3			74	10	-
4			96	73	67

Figure 1.5 The asymmetric epoxidation reactions catalyzed by chloroperoxidase [7].

Many of the epoxide products derived from chloroperoxidase catalysis can serve as chiral synthons for drug and natural product synthesis. Chloroperoxidase is a readily available and considerably stable enzyme that is well suited for important and valuable synthetic strategies. However, the structural basis for Chloroperoxidase catalyzed chiral reactions has not been well understood. One of the main tasks of my projects is to elucidate the mechanisms of such reactions as will be discussed in Chapter 2 of this dissertation.

1.7 Anticancer Effects of Selected Natural Product Derivatives

Wogonin is a plant flavonoid extracted from *Scutellaria baicalensis* (Figure 1.6) and has been studied by many researchers for its anti-viral, anti-oxidant, anti-cancerous and neuro-protective properties [30]. During the last 20 years, wogonin (WG; 5,7-dihydroxy-8-methoxyflavone) was identified as a potent apoptosis inducer of cancer cells with good efficacy and minor side effects. Furthermore, pharmacokinetic studies

in rats support the possible use of WG in clinic applications. It has been approved for

Phase I clinical trials in China.
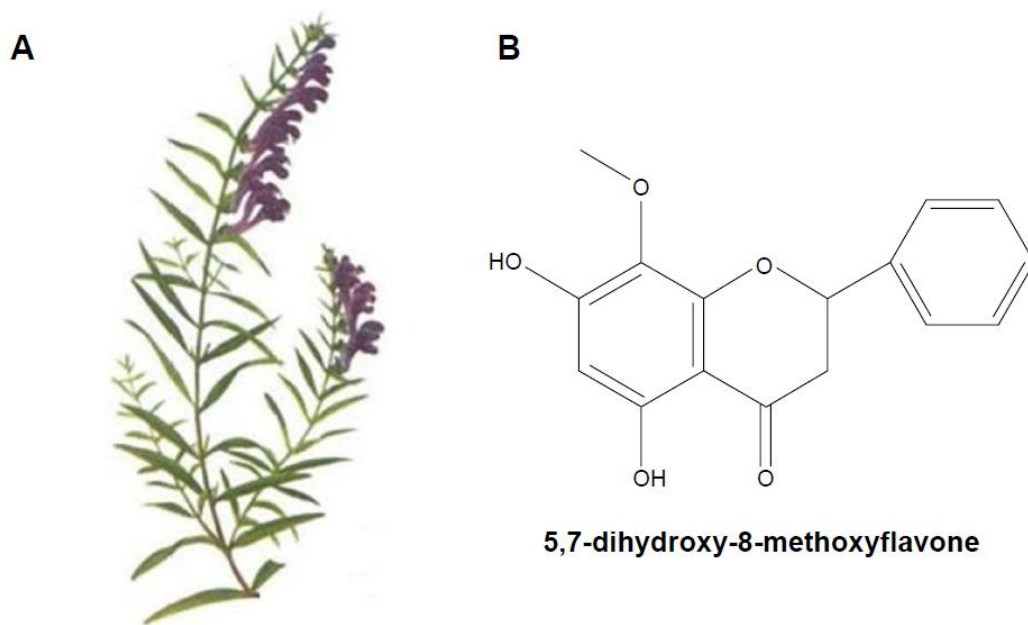
Figure 1.6 Scutellaria baicalensis Georgi (Huang Qin) and WG. (A) The plant of Huang Qin. (B) The chemical structure of WG. Abbreviation: WG, wogonin [31].

Several studies have shown its inhibitory activity on the viability and the growth of

tumor cells. Various investigations have also demonstrated that WG exerts its antitumor

effects via regulation of multiple molecular pathways. The key molecular pathways of

its antitumor effects include reactive oxygen species (ROS), Ca^{2+}, NF-κB, tumor

necrosis factor-related apoptosis-inducing ligand (TRAIL), and tumor necrosis factor-

alpha, which participates in both intrinsic mitochondria-mediated and extrinsic

receptor-mediated pathways. In addition to its activation of Bax/Bak protein and

caspase-8/caspase-9/caspase-3, WG plays an important role in inhibiting

lipopolysaccharide-induced or hydrogen peroxide (H_2O_2)-induced tumor angiogenesis

through PI3K/AKT/NF-κB signaling pathway. In addition, the ability of WG to inhibit tumor angiogenesis by decreasing the expression of hypoxia-inducible factor-1α (HIF-1α) protein was also observed. All those ablity is aiming to summarize its new developments for its future clinical use.[31]. The results of my studies on two derivatives of WG demonstrated the potential of improving the biological activity of this natural product and offers new insights into the mechanisms of the anticancer activity of this class of compounds.

CHAPTER II.

ENHANCING THE CATALYTIC PERFORMANCE OF

CHLOROPEROXIDASE BY CO-IMMOBILIZATION WITH GLUCOSE

OXIDASE ON MAGNETIC GRAPHENE OXIDE

2.1 Background

Although chloroperoxidase (CPO) has long been recognized as a powerful and versatile catalyst, its applications have been thwarted by the difficulty in regenerating the active enzyme and substrate (peroxide) induced protein inactivation. In this paper, we describe the fabrication and characterization of CPO and Glucose Oxidase (GOx) on the surface of Magnetic Graphene Oxide (MGO). The performance of the immobilized CPO was considerably enhanced by coupling with GOx that provided the required H_2O_2 in situ through glucose oxidation. The activity of MGO-GOx-CPO (96.6%) towards the decolorization of orange G was much superior to that of MGO-GOx + MGO-CPO (86.2%), probably as a result of reduced mass transfer resistance between CPO and H_2O_2 generated from GOx molecules. Interestingly, MGO-GOx-CPO reached its peak activity (95.2%) when temperature was maintained between 42 °C and 50 °C compared to the optimal temperature of 35 °C for the free enzyme, possibly due to dispersion of the otherwise stacked MGO below 42 °C. Finally, MGO-GOx-CPO can be conveniently reused for its ease of recovery in the presence of an external magnetic field, with ~38.5% activity remained after 6 cycles of applications.

This work demonstrates the feasibility of co-immobilizing CPO and GOx onto MGO and the potential of MGO-GOx-CPO in environmental applications.

2.2 Experimental Procedure

2.2.1 Materials & Methods

2.2.1.1 Materials

Chloroperoxidase was isolated from the growth medium of *Caldiamides fumago* according to the method of Morris and Hager [9] with minor modifications as described previously [32]. The activity of CPO used in this study was 4800 U/mL based on the standard monochlorodimedon (MCD) assay [33]. The stock CPO was kept in 0.1 mol/L phosphate buffer (pH 5.0) at 4 °C Glucose oxidase was purchased from Sigma-Aldrich (10 kU/29 mg). β-D-glucose was obtained from Tokyo Chemical Industry Co. Ltd. Graphite, $(NH_4)_2Fe(SO_4)_2·6H_2O$, $NH_4Fe(SO_4)_2·12H_2O$, $NH_3·H_2O$, KH_2PO_4, K_2HPO_4 and H_2SO_4 (98%) were acquired from Sinopharm Chemical Reagent Co. Ltd. H_2O_2 (30% in aqueous solution), $NaNO_3$ and $KMnO_4$ were provided by Xi'an Chemical Reagent Factory. All chemicals were of analytical grade and used without further purification.

2.2.1.2 Preparation of MGO

GO was prepared from graphite powder according to published method [34, 35]. Briefly, 1.0 g of graphite powder and 0.5 g of $NaNO_3$ in 75 mL of concentrated H_2SO_4 were stirred in an ice-water bath, 3.0 g of $KMnO_4$ was then added gradually with constant stirring. After the stirring was continued for 2 h at temperatures below 10 °C,

the ice bath was removed, and the mixture was stirred at 35 °C for another 30 min. The reaction mixture was diluted with 45 mL of distilled water and the temperature was increased to and kept at 98 °C for 30 min. The reaction was terminated by adding 140 mL of distilled water, followed by the addition of 6 mL of 30% H_2O_2. The resulting reaction mixture was centrifuged and washed several times with 5% HCl solution, then by deionized water until the pH of the supernatant became neutral. The GO obtained was dried for the preparation of the magnetic Fe_3O_4/GO composites.

The MGO composites were prepared by co-precipitating $(NH_4)_2Fe(SO_4)_2 \cdot 6H_2O$ and $NH_4Fe(SO_4)_2 \cdot 12H_2O$ in the presence of GO. Briefly, 5.8 g of $(NH_4)_2Fe(SO_4)_2 \cdot 6H_2O$ and 10.7 g of $NH_4Fe(SO_4)_2 \cdot 12H_2O$ were dissolved in 100 mL of deionized water under an argon atmosphere and stirred for 30 min. GO (1.0 g) in 100 mL of water was ultrasonicated for 1 h and was then added slowly to the $(NH_4)_2Fe(SO_4)_2 \cdot 6H_2O$ and 10.7 g of $NH_4Fe(SO_4)_2 \cdot 12H_2O$ mixture along with ammonia with constant stirring for 45 min at 85 °C. When the solution was cooled to room temperature, the black precipitates (MGO composites) were washed with deionized water and dried in a vacuum.

2.2.1.3 Immobilization of CPO and GOx

Immobilization of enzyme molecules was achieved by physical ad- sorption of the enzymes onto the surface of MGO sheets. Briefly, 0.25 mg MGO in 1.5 mL phosphate buffer was ultrasonicated for 30 min and then separated by magnetic decantation. Subsequently, the MGO was mixed with 10 μL (0.15 mmol/L) CPO in 1.5 mL phosphate buffer and incubated with constant shaking at 20 °C for 25 min. CPO

absorbed on MGO (MGO-CPO) was magnetically separated from free CPO and rinsed twice with phosphate buffer. The MGO-GOx was obtained using the same procedure with GOx replacing CPO in the preparation of MGO-CPO.

The MGO-GOx-CPO was also obtained with the same procedure by replacing the individual enzyme solution with a mixture of 10 µL (0.15 mmol/L) CPO and 5 µL (29 mg/mL) GOx.

2.2.1.4 Characterization of the carrier and the immobilized enzyme

X-ray Powder diffraction (XRPD) was performed on a D/MAX-2550/PC diffractometer at 40 kV and 30 Ma using Cu Kα radiation (λ = 0.15406 nm). Transmission electron microscopy (TEM) images were obtained with a JEM-2100 microscope at an accelerating voltage of 200 kV. Scanning electron microscopy (SEM) images were recorded on a FEI Quanta 200 microscope at an accelerating voltage of 20 kV. Laser scanning confocal microscopy images were taken on an Olympus FV1200 confocal microscope with the detection wavelengths at 488 nm and 559 nm for fluorescein isothiocyanate (FITC) and rhodamine B isothiocyanate (RhB) respectively, where 8 mg of fluorescein iso- thiocyanate (FITC) or rhodamine B isothiocyanate (RhB) dissolved in DMSO (2 mg/mL) was slowly added in to 1 mL of GOx or CPO solution (in pH 9). The solution was shaken for 8 h at 200 rpm in dark. Then, free FITC or RhB was removed by dialysis and the fluorescent molecule-labeled enzymes were obtained.

2.2.1.5 Enzyme activity

The catalytic activity of the free and immobilized CPO was determined based on their efficiency to decolorize Orange G [36, 37]. The reaction was carried out in 1.5 mL mixtures containing 0.125 mmol/L Orange G, free or immobilized CPO (2.0×10^{-10} mol) in phosphate buffer (pH 3.0) and appropriate concentrations of H_2O_2 (for free CPO and MGO-CPO) or β-D-glucose (for MGO-GOx + MGO-CPO and MGO-GOx-CPO). The decolorization efficiency was measured within 30 min for free CPO or MGO-CPO, and 60 min for MGO-GOx + MGO-CPO or MGO-GOx-CPO. All experiments were repeated at least three times under the same conditions. Control was performed without enzyme while keeping other conditions identical. The percent degradation was measured by following the absorbance change at 478 nm using a Shimadzu UV-1700 UV–vis spectrophotometer and calculated using the following equation:

Decolorization efficiency (%) = $[(A_0 − A_t)/A_0] \times 100\%$

Where A_0 is the initial absorbance and A_t stands for absorbance after "t" min of reaction.

2.2.1.6 Effects of supporting material on the adsorption of dye

Appropriate amount of dye was added to 0.50 mg of the carrier or carrier-immobilized CPO. When the adsorption equilibrium is reached (~20 min), the adsorption rate was calculated by measuring the absorbance at 478 nm. H_2O_2 or β-D-glucose was added to the solution for decolorization of the dye. Then the buffer was

added to the carrier with adsorbed dye after magnetic separation. The desorption of dye was carried out in a thermostatic oscillator (200 r/min) at 30 °C for 3 h and the amount of dye found in the supernatant was analyzed by measuring the absorbance at 478 nm. At the same time, the carrier (without immobilized enzymes) with magnetic separation was achieved after the adsorption reached equilibrium. The same experiment of dye desorption was carried out and the absorbance value of the supernatant was measured.

2.2.1.7 Kinetic properties of the immobilized CPO

Kinetic assay for CPO-catalyzed degradation of Orange G was car- ried out over the concentration range of 0.05~0.125 mmol/L at optimal conditions (pH 3.0, 20 °C, 30 min, 0.25 mmol/L of H_2O_2 (for free and MGO-CPO); pH 3.0, 20 °C, 60 min, 23 mmol/L of β-D-glucose (for MGO-GOx-CPO) established from our optimization experiments. The kinetic parameters including Michaelis constant (K_m), maximum rate of reaction (V_{max}), turnover number (k_{cat}), and catalytic efficiency (k_{cat}/K_m) were calculated from the Lineweaver-Burk plots.

2.2.1.8 Degradation of acid blue 45 and crystal violet with MGO-GOx-CPO

As a model reaction, the decolorization efficiency of Orange G was used to measure the catalytic activity of MGO-GOx-CPO. To test if the MGO-GOx-CPO can also degrade other dyes, acid blue 45 and crystal violet were used as substrates to evaluate the catalytic efficiency of CPO co-immobilized with GOx. The assay was carried out in 1.5 mL phosphate buffer (0.1 mol/L, pH 3.0) containing 2.0×10^{-10} mol CPO and 0.17 mM acid blue 45 or 0.045 mM crystal violet. The reaction was monitored for 30

min at the characteristic absorbance of acid blue 45 or crystal violet at 595 and 584 nm, respectively.

2.2.1.9 Degradation of Orange G in wastewater sample MGO-GOx-CPO

The potential application of MGO-GOx-CPO to remove dye from actual environmental samples was evaluated by the degradation of Orange G in industrial wastewater. The wastewater samples were collected from Hei river, Fengyu (naturally running river water), Qinzhen (running urban water) and man-made lake (still water), respectively. The degradation of orange G is carried out following the same procedure with identical conditions as described in the previous sections, except that buffer was replaced by wastewater sample at pH 3.0 adjusted with 1.0 mol/L HCl.

2.2.1.10 Thermal stability of CPO in different states

Free CPO, MGO-CPO, MGO-GOx + MGO-CPO, MGO-GOx-CPO in 0.1 mol/L phosphate buffer (pH 5.0) was pre-incubated for 60 min at various temperatures (20, 30, 40, 50, 60 and 70 °C) in a closed thermostatic water bath. The thermal stability of the enzyme was tested and expressed as residual activity (the ratio of activity before and after incubation at different temperatures) or was determined as a function of reaction time (0-24 h) at 50 °C.

2.2.1.11 Reusability of the MGO-enzymes

The reusability of MGO-CPO, MGO-GOx + MGO-CPO, and MGO- GOx-CPO was determined and expressed as residual activity with the activity of the first run defined

as 100%. The immobilized CPO was recovered after each reaction cycle by magnetic decantation and washed with phosphate buffer (pH 5.0).

2.3 Results& Discussion

2.3.1 Characterization of supporting materials and immobilized enzymes

X-ray powder diffraction (XRPD) is one of the most powerful methods for the study of crystalline and partially crystalline solid-state materials and has been widely used in the study of graphene related materials [38, 39]. Figure 2.1 shows the XRPD data of the graphite in comparison with GO (a) and MGO (b). The most striking feature is the typical graphene (002) signature at 26.6°. The sharp and intense peak of the diffraction pattern indicates high quality of the crystals [40].
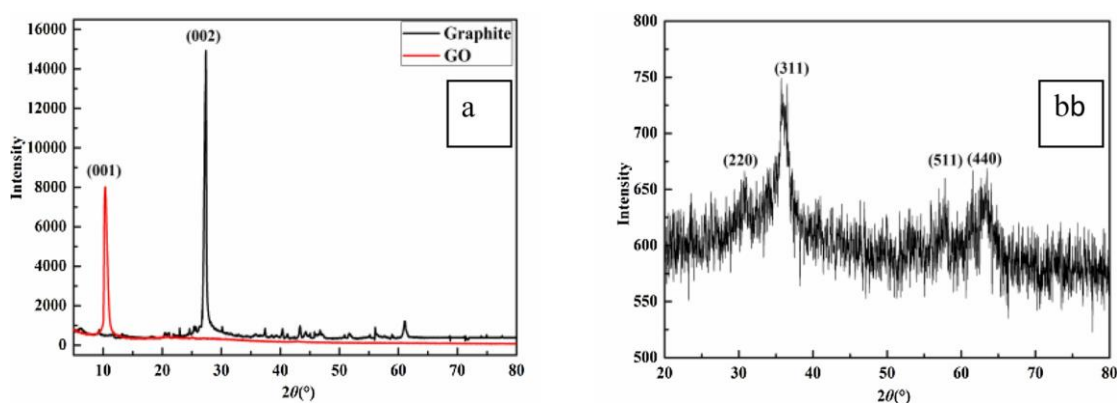
Figure 2.1 XRPD patterns of (a) graphite compared with GO and (b) MGO.

Usually, as graphene is oxidized to graphene oxide, the signature peak of graphene disappears and a new peak at a much smaller angle (around 10.4°) appears with an index of (001) (Fig. 1a). These peaks were more intense in the case of Fig. 1b due to

higher concentration of Fe_3O_4 nanoparticles in the sample. The XRPD peaks were indexed to (220), (311), (511) and (440) planes of a cubic unit cell of magnetite, appearing at 30.3°, 35.7°, 57.0° and 62.7°, respectively (JCPDS 65–3107). Figure 2.1 also revealed that except for the peaks assigned to Fe_3O_4, no diffraction peaks were assignable to GO indicating that the stacking of GO sheets in the composites was disordered [41].

The morphologies of GO, MGO and MGO-enzymes were characterized by transmission electron microscopy (TEM) (Figure 2.2a–c) and scanning electron microscopy (SEM) (Figure 2.2d–f). Both TEM and SEM suggested that GO had crumpled sheet-like structures (Figure 2.2a and 2.2d) and Fe_3O_4 nanoparticles were sparsely deposited and unevenly distributed on the surfaces of GO (Figure 2.2b and 2.2e). Figure 2.2c and 2.2f were the TEM and SEM images, respectively, of MGO-enzymes. Although the GO sheet was clearly visible compared with MGO composites, the number of particles on the carrier was increased, suggesting that the immobilized enzyme was adsorbed on the carrier and did not significantly influence the morphology of the composites.
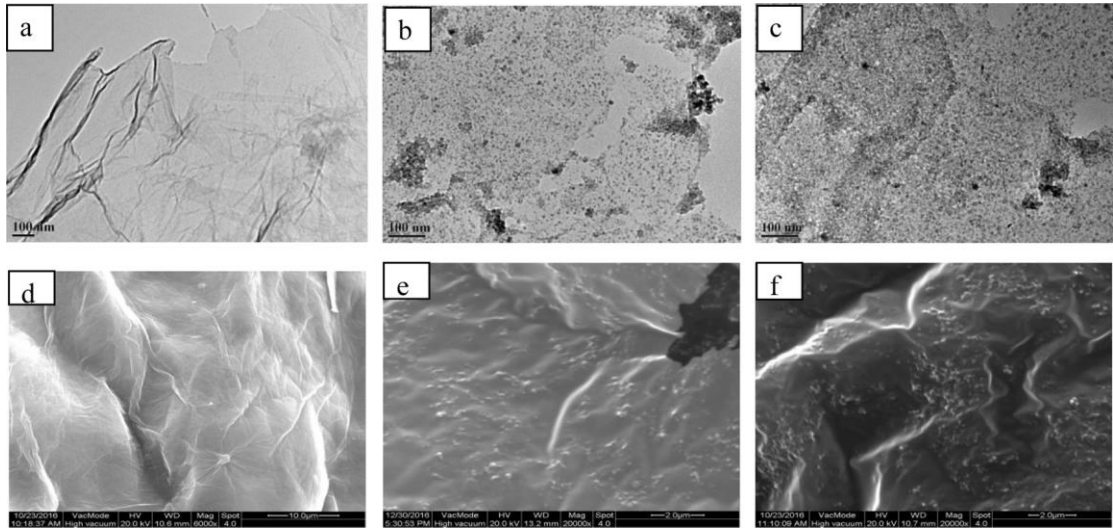
Figure 2.2 TEM images of GO (a), MGO (b), MGO-enzymes (c) and SEM images of GO (d), MGO (e), MGO-enzymes (f).

To further confirm the immobilization of protein on MGO, GOx and CPO were labeled with fluorescent probes fluorescein isothiocyanate (FITC) and rhodamine B isothiocyanate (RhB), respectively. Confocal laser scanning microscopy (CLSM, Figure 2.3) did show the simultaneous presence of both FITC–CPO (green) and RhB–GOx (red) on the surface of MGO.
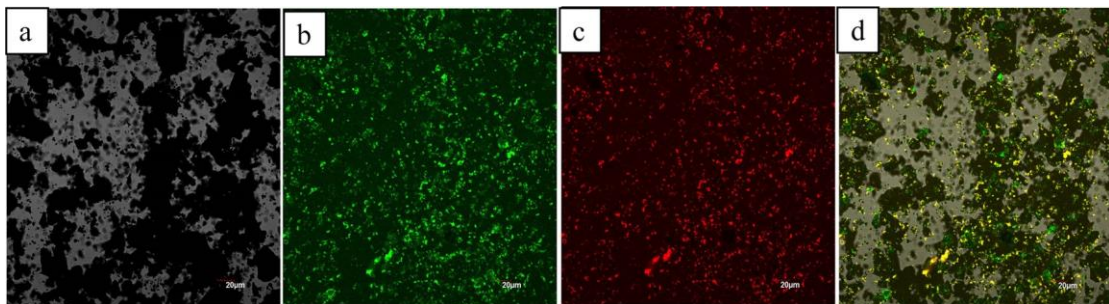
Figure 2.3 Laser scanning confocal microscope images of MGO (a), MGO-CPO (FITC) (b), MGO-GOx (RhB) (c) and MGO-CPO (FITC) -GOx (RhB) (d).

The detection of protein (CPO/GOx) is carried out by HPLC equipped with a UV/Vis detector set at 280 nm. The concentration of CPO and GOx in MGO-GOx-CPO is 1.4×10^{-7} mol/L and 9.3×10^{-8} mol/L, respectively, based on the of enzyme concentration

before and after immobilization. The molar ratio of CPO:GOx in MGO-GOx-CPO is 3:2.

2.3.2 Effects of reaction parameters on the efficiency of orange G decolorization

The effects of reaction parameters including H_2O_2 and β-D-glucose concentration were investigated on the decolorization of orange G by MGO-GOx + MGO-CPO or MGO-GOx-CPO.

For MGO-CPO, the decolorization rate increased significantly at low H_2O_2 concentrations and reached a plateau when H_2O_2 concentration was increased to 0.25 mmol/L as shown in Figure 2.4a. When H_2O_2 concentration was further increased (up to 1.0 mmol/L), the degradation rate decreased, possibly due to inactivation caused by internal oxidative destruction of the enzyme's heme active site [37]. Therefore, an initial H_2O_2 concentration of 0.25 mmol/L was chosen for the rest of this study.
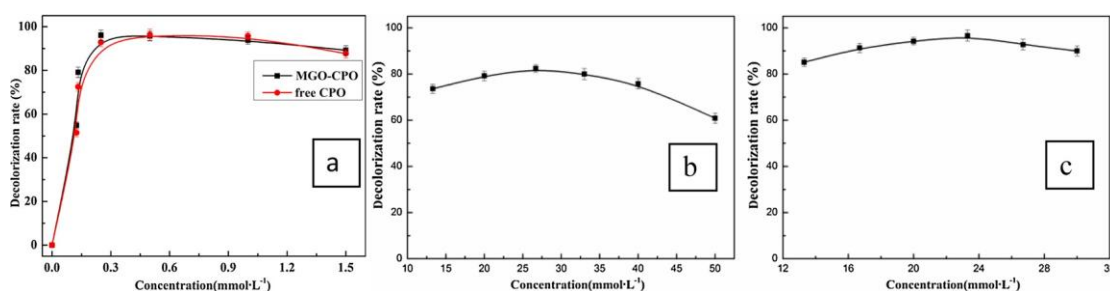
Figure 2.4 Effects of reaction parameters on the efficiency of Orange G decolorization: (a) H_2O_2 concentration for MGO-CPO and free CPO; (b) β-D-glucose concentration for MGO-GOx + MGO-CPO; (c) β-D-glucose concentration for MGO-GOx-CPO.

However, variations in glucose concentration between 0.1 and 1.0 mol/L had little effect on the rate of formation with no more than 0.30 μmol/min H2O2 in a 0.1 mol/L glucose solution for a reaction time of 1600 min [42]. Therefore, the deactivation of

CPO in this work can be avoided due to hydrogen peroxide generation in situ.

For MGO-GOx + MGO-CPO and MGO-GOx-CPO, the experiment was performed with varying concentrations of glucose (0~40 mmol/L) in 0.1 M PBS. As shown in Figure 2.4b and 2.4c, similar bell-shaped curves were observed with a maximum value of ~27 mmol/L and 23 mmol/L for MGO-GOx + MGO-CPO and MGO-GOx-CPO, respectively. When β-D-glucose concentration was low, not enough H_2O_2 can be released for CPO catalysis. However, high concentrations of glucose are not favorable for CPO either due to the irreversible in- activation of CPO caused by β-D-glucose [43]. It has been reported that β-D-glucose can result in precipitation of CPO due to its potential interaction with amino groups and binding to the carbohydrates on the surface of the protein. This interaction can also result in the fall-off of CPO from the carrier (CPO immobilized on the carrier only by physical coupling via weak force) and the decrease of catalytic activity of MGO-GOx-CPO [43]. However, the interaction of glucose with CPO can be ignored in our experiment because the concentration of glucose was controlled at a lever below noticeable adverse effect can take place. Therefore, 27 and 23 mmol/L of glucose were used for the MGO-GOx + MGO-CPO and MGO-GOx-CPO systems in further studies.

2.3.3 Effects of supporting material on the adsorption of dye

In order to distinguish whether the decolorization is achieved by oxidation or simple physical adsorption of the dyes on the carrier, the effect of adsorption and desorption of the dye was investigated (Table 2.1). Orange G was not degraded by the carrier itself.

Even if the dye was adsorbed on the carrier, the adsorbed dye was actually degraded by

where A1 or A2 is the absorbance at 478 nm before and after adsorption, respectively.

A3 is the absorbance at 478 nm after desorption CPO in the carrier. Therefore, although

the decolorization was due to the combined effects of catalytic oxidation and adsorption,

catalytic oxidation of the enzyme played the dominating role in the observed

decolorization activity of MGO-enzymes.

Table 2.1 Adsorption and desorption rate of dye on the surface of MGO.

Catalyst	A_1	A_2	Adsorption rate/%	A_3	Desorption rate/%
MGO	1.176	0.957	18.6	0.047	4.0
MGO-CPO	1.121	1.034	12.4	0.020	1.7
MGO-GOx + MGO-CPO	1.205	1.072	11.0	0.023	1.9
MGO-GOx-CPO	1.194	1.038	13.1	0.024	2.0

2.3.4 Kinetic properties of the immobilized CPO

As expected, the kinetic parameters (Km and Vmax) of free CPO were both changed

after immobilization on different supporting materials (Table 2). Of particular interest,

the Km of immobilized CPO on MGO and MGO-GOx decreased systematically

compared to that of the free CPO. The significant decrease in Km of the immobilized

CPO indicated dramatic increase in the protein's affinity toward substrate (orange-G),

suggesting either favorable conformational changes in CPO or the advantageous

surface property of the carrier (large surface area and functional groups) that enhanced

the formation of enzyme-substrate complex upon immobilization. Both Vmax and kcat for the immobilized CPO on either MGO or MGO- GOx were lower than those of the free CPO. The decrease in maximum rate and turnover number are anticipated due to diffusional limitations imposed by the carrier that would result in reduced speed of the co- substrate, H_2O_2, to access the active site of CPO immobilized on MGO. Thus, CPO immobilized on MGO-GOx showed the lowest Vmax and kcat because H_2O_2 needs to be generated in situ in MGO-GOx-CPO. Interestingly, the catalytic efficiency (k_{cat}/K_m) of CPO immobilized on either MGO or MGO-GOx was approximately 2.1- and 2.5- times higher, respectively, compared to that of the free CPO. The superior catalytic efficiency of CPO immobilized on MGO-GOx implicates catalytically efficient encounters of the substrate with CPO in this system is significantly improved, possibly due to the in-situ generation of H_2O_2 that eliminates oxidative damage to CPO as a result of local extreme concentrations of H_2O_2 in solution. Our results suggested that use of an enzyme cascade is practical in harnessing the catalytic power of enzymes, such as cytochromes P450 that require the participation of auxiliary enzymes (reductases) [44-46].

Table 2.2 Kinetic properties of free and immobilized CPO[a].

Enzyme	$V_{max} \pm$ S.D.[b] $(mM \cdot s^{-1})$	$K_m \pm$ S.D.[b] (mM)	k_{cat} (s^{-1})	k_{cat}/K_m $(s^{-1} \cdot mM^{-1})$
Free CPO	0.1073 ± 0.00921	0.0741 ± 0.00517	794.8	1.1×10^4
MGO-CPO	0.0947 ± 0.00883	0.0303 ± 0.00437	701.5	2.3×10^4
MGO-GOx-CPO	0.0743 ± 0.00973	0.0196 ± 0.00589	550.4	2.8×10^4

[a] Concentration of CPO used: 1.4×10^{-7} mol·L^{-1}.
[b] Standard deviation.

2.3.5 Degradation of orange G, acid blue 45 and crystal violet by MGO-GOx-CPO

It is exciting to note that CPO immobilized on MGO displayed significantly enhanced catalytic activity toward the degradation of all three dyes selected in this study. As shown in Fig. 5, up to 96.1% Orange G, 97.2% Acid blue 45 and 98.5% Crystal violet are degraded by MGO-GOx-CPO within 60 min under relatively mild conditions. It is also worth mentioning that MGO-GOx-CPO effectively decolorized environmental wastewater contaminated by synthetic dyes as described below.
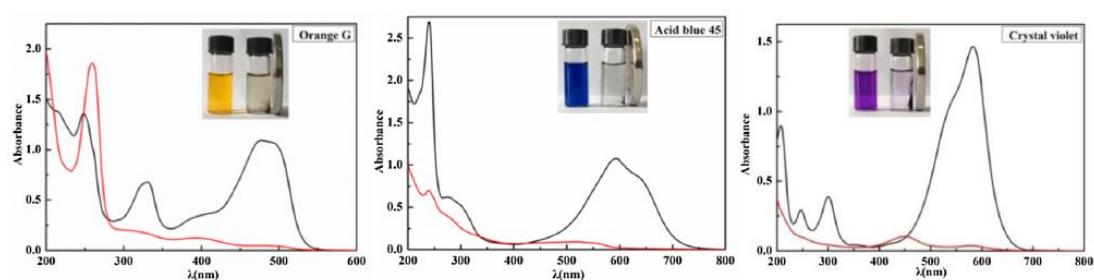
Figure 2.5 MGO-GOx-CPO catalyzed decolorization/degradation of orange G, acid blue 45 and crystal violet as monitored by UV/Vis spectrophotometry. The insets in the figures show the color of samples before and after CPO degradation.

Figure 2.6 Decolorization of orange G with MGO-GOx-CPO in pure buffer and in actual wastewater with same amount of orange G added (From left to right, orange G in pure buffer without treatment, and orange G in water samples from Hei river, Fengyu, Qinzhen and a man-made lake after treatment).

The decolorization of Orange G (0.125 mmol/L) in wastewater by MGO-GOx-CPO was shown in Figure 2.6. The decolorization efficiency of Orange G reached 93.4% in Hei river, 92.2% in Fengyu, 90.3% in Qinzhen, and 87.8% in a man-made lake, respectively. The decrease of decolorization efficiency in real wastewater samples was possibly due to the presence of multiple metal ions and microorganism in the samples that would interfere with the performance of CPO.

2.3.6 Thermal stability of CPO

Most catalytic reactions in industry are carried out under conditions unsuitable for naturally occurring enzymes. For example, running reactions at elevated temperature is a common practice to accelerate reaction rate, increase solubility, reduce solution viscosity, and avoid microbial pollution. This precludes the industrial application of many enzymes due to their limited thermal stability. Immobilization on suitable supports offers a novel revenue to improve the thermal stability of the enzymes, making their large-scale industrial application possible.

2.3.6.1 Thermal stability of CPO from 20 °C to 70 °C

Temperature is a critical factor that affects the decolorization of orange G by both free and immobilized CPO. Figure 2.7a show the thermal stability of free and immobilized CPO expressed as residual activity after incubation at different temperatures (from 20 °C to 70 °C). In general, the stability of MGO-CPO differs notably from that of free CPO. When reaction temperature is increased to 70 °C, free CPO kept only about 10% of its initial activity, while MGO-CPO retained approximately 30% of its initial activity within one hour.
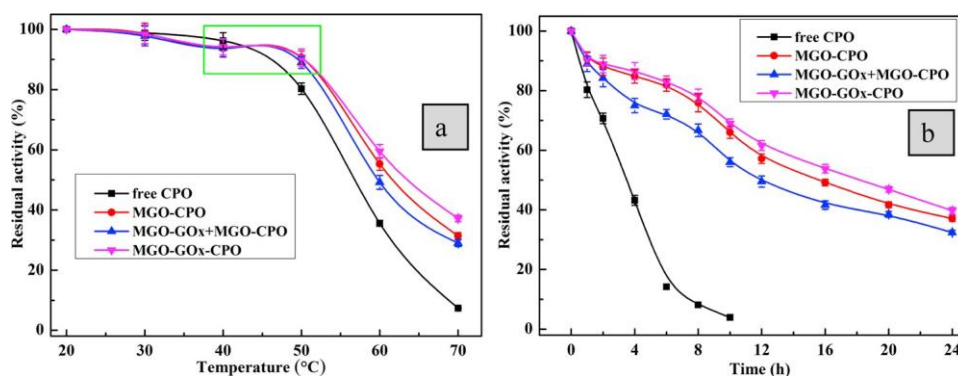
Figure 2.7 Thermal stability of free and immobilized CPO (a) at different temperatures and (b) at 50 °C as a function of time.

The thermal stability of CPO was different for the three immobilization systems designed. On one hand, MGO-GOx-CPO was superior to the combination of MGO-GOx and MGO-CPO, probably due to mass transfer resistance between GOx and CPO experienced in the latter case. As shown in Figure 2.8a, when GOx and CPO were individually immobilized on the surface of MGO, the oxidation of β-D-glucose was catalyzed by GOx in the presence of O_2 to produce H_2O_2 in situ, which was used as the oxidant by the nearby CPO for the degradation of dyes. The catalysis will be improved

if the H_2O_2 produced can reach CPO and the dye substrate quickly. This explains the fact that the amount of oxidant was not always proportional to the observed activity of CPO. The advantage of in situ production of H_2O_2 in MGO-GOx-CPO is a critical factor in determining the operational stability and catalytic efficiency of CPO. In addition, there is no mass transfer resistance between CPO and GOx compared to the combination of MGO-GOx and MGO-CPO, allowing the H_2O_2 produced in situ to be directly used for the effective transformation of substrates (Figure 2.8b).
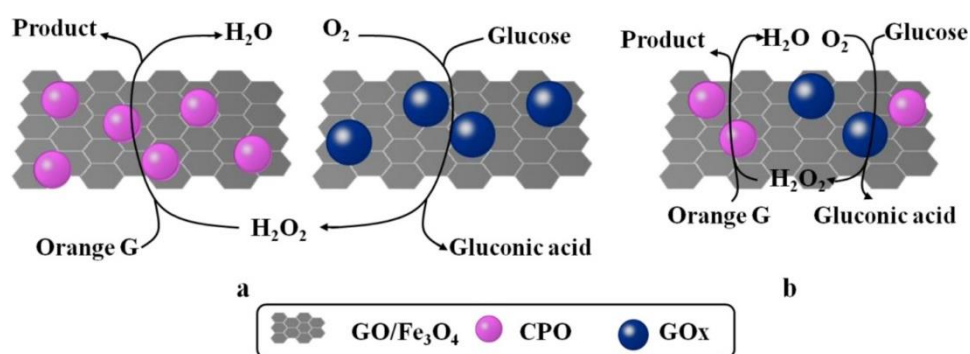
Figure 2.8 (a) Mass transfer resistance between CPO and GOx for MGO-GOx + MGO-CPO; (b) no mass transfer resistance between CPO and GOx for MGO-GOx-CPO.

2.3.6.2 Thermal stability of CPO at 50 °C

The thermal stability of free and immobilized CPO at 50 °C is shown in Figure 2.7b. As can be seen, the stability of CPO was significantly improved after immobilization. The immobilized CPO retained more than 60% of its initial activity after 10 h incubation at 50 °C, while free CPO completely lost its activity under identical conditions. Immobilized CPO on MGO-GOx resulted in the highest stability. This is due, in part, to the improved enzyme rigidity associated with immobilization [47] and in part to the

in situ production of H2O2 that avoids the oxidative in- activation of CPO caused by local extreme concentrations of H2O2.

It should be noted that the thermal stability of CPO immobilized on MGO composites was not only much better than free CPO but also superior to CPO immobilized on other supports pioneered by other groups [47-50]. In practice, formation of multi point interactions between enzymes and MGO composites may stabilize the weak intramolecular forces [47].

Moreover, the GO layers will naturally stack due to the presence of Fe3O4 in MGO. This makes it difficult for some enzyme molecules to play an effective catalytic role. It is worth mentioning that the activity of MGO-GOx-CPO displayed a somewhat strange relationship with the reaction temperature as shown in Figure 2.7a. Different from a consistent decrease in activity with increasing temperature as observed with free CPO, the activity of MGO-GOx-CPO initially decreased as temperature was increased. However, when temperature reached a critical point around 42 °C, the activity of MGO-GOx-CPO started to increase and remained high until temperature reached 50 °C. This unusual phenomenon could be attributed to the re-dispersion of the stacked MGO layer due to thermal diffusion (Figure 2.9) as revealed by SEM images (Figure 2.10). The dispersion of the stacked MGO layers override the adverse effect of increasing temperature, accounting for the good thermal stability of CPO immobilized on MGO between 42 and 50 °C. However, as temperature went above 50 °C, the adverse effect of increasing temperature superseded the beneficial effects from dispersion of the

stacked MGO layers, therefore the activity of MGO-GOx-CPO decreased as temperature was further increased.
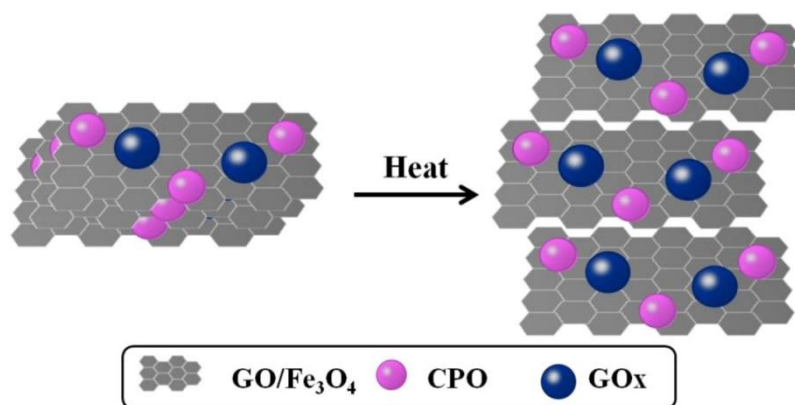
Figure 2.9 The GO layers are dispersed due to thermal diffusion.
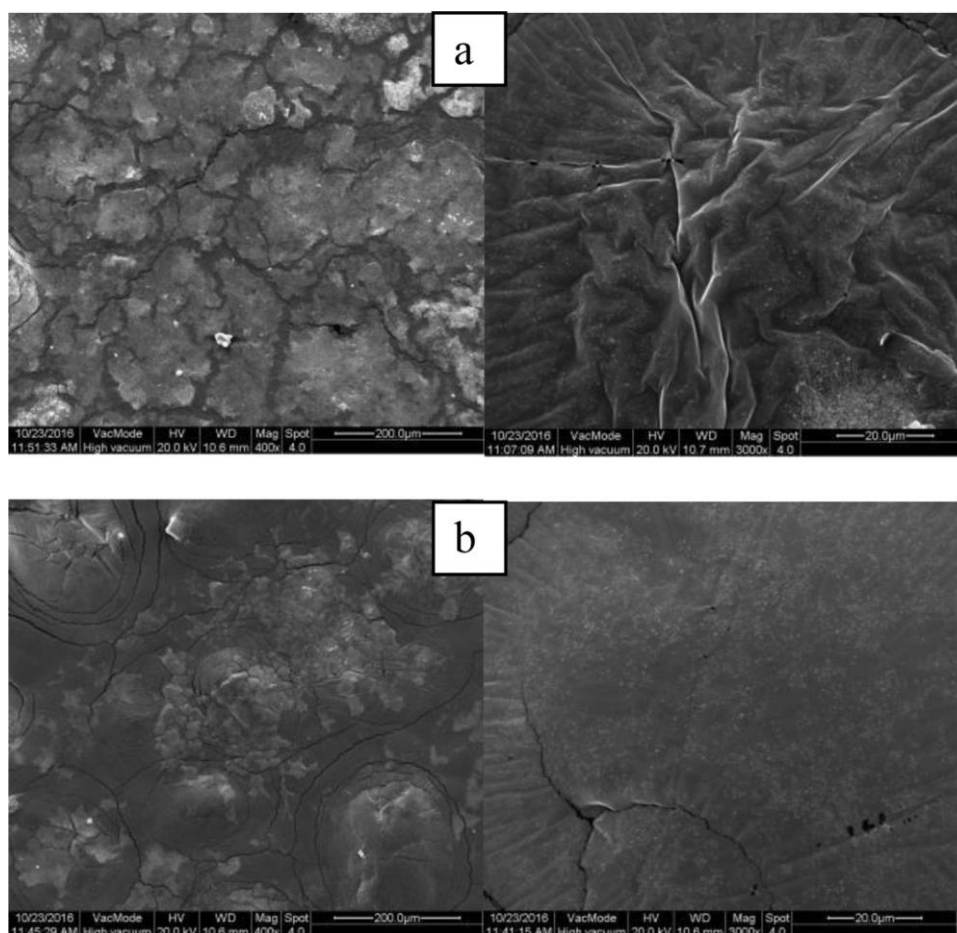
Figure 2.10 SEM images of the GO dispersed layers at 20 °C (a) and 50 °C (b).

2.3.7 Reusability of MGO-GOx + MGO-CPO and MGO-GOx-CPO

The reusability of immobilized CPO on different systems is shown in Figure 2.11. CPO co-immobilized with GOx (MGO-GOx-CPO) shows a relatively good reusability with more than 38.5% residual activity retained after 6 cycles of use for the oxidation of the dyes. Consistent with enzymes immobilized on most supporting materials [51, 52], the activity of MGO-GOx-CPO decreased after each recycle, possibly due to enzyme fall off from the carrier. Nonetheless, the magnetic nature of GO composite particles allows easy separation of the immobilized CPO from the reaction mixture, making the reuse of CPO feasible.
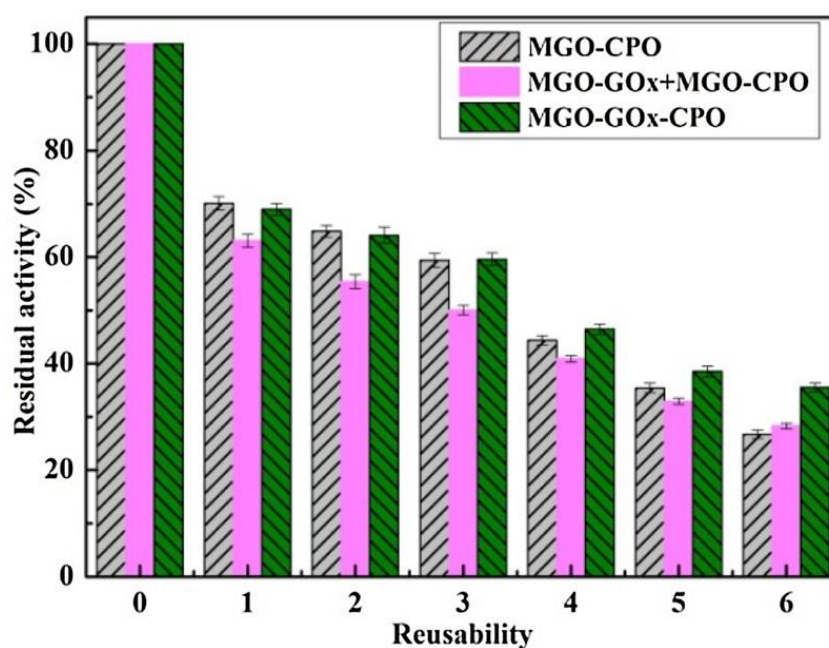
Figure 2.11 MGO-CPO displays significantly improved reusability in catalysis.

2.4 Conclusion

A new type of composites (GO-Fe$_3$O$_4$) with the combined ad- vantages of large surface area of GO and magnetic property of Fe$_3$O$_4$ was synthesized to serve as supports for the immobilization of CPO and GOx-CPO. The immobilized CPO exhibits enhanced operational dur- ability, thermal stability, catalytic efficiency, and reusability. in particular, MGO-GOx-CPO, showed far greater thermal stability than the free enzyme. MGO-GOx-CPO not only reduce the mass transfer resistance between the two enzymes, but also allow the production of H$_2$O$_2$ in situ. Taken together, our results presented herein demonstrated that GO functionalized by Fe$_3$O$_4$ is a great support for the co-immobilization of CPO with GOx. This material might also find applications in the assembly of robust biological catalysts composed of other enzyme systems such as cytochromes P450 for the synthesis of fine chemicals and degradation/removal of synthetic dyes and other pollutants from industrial wastewater.

CHAPTER III.

MECHANISMES OF CHLOROPEROXIDASE-CATALYZED

ENANTIOSELECTIVE EPOXIDATIONS--A NUCLEAR

PARAMAGNETIC RELAXATION STUDY

3.1 Background

The characterization of CPO-substrate complex will be carried out using UV-Vis spectrophotometry and nuclear magnetic resonance (NMR) spectroscopy. We will focus on understanding the mechanism of CPO-catalyzed enantioselective epoxidation and structure-activity relationship of CPO. As we know, this mechanism also represents synthesis featuring enantioselective epoxidation moderated by chloroperoxidase. Because of chloroperoxidase's ready availability, ease of use, and potential for high selectivity, its use in the synthesis of intermediates difficult to obtain by other methods is a continuing investigation in my research [53]. So, to investigate the mechanism of CPO-catalyzed reactions remains mysterious and its application will be ringing rapid and effective development in industry. The project will investigate the structural factors that contribute to CPO's stereoselectivity in catalyzing epoxidation reactions.

Chloroperoxidase from the marine fungus *Caldariomyces fumago* has been the subject of extensive studies due to its versatile catalytic activities and potential biotechnological applications such as synthetic chemistry, pharmaceutical industry, and environmental management. Chloroperoxidase catalyzes a broad spectrum of chemical reactions including the traditional oxidation activity typical of classical peroxidases,

dismutation reaction of catalase, epoxidation of olefin by cytochrome P450 monooxygenases, and halogenation/dehalogenation reactions unique to haloperoxidases. Most significantly, CPO-catalyzed oxidation and epoxidation reactions proceed with high regio- and enantio-selectivity. Great efforts have been made during the past several decades aimed at understanding the mechanism of CPO's regio- and/or enantio-selectivity [114]. It has been generally agreed that most enzyme catalyzed chemical transformations proceed via the formation of enzyme-substrate complexes. Therefore, understanding the structural features of the CPO-substrate complexes will undoubtedly cast fresh light on the structure-function relationships of heme peroxidase in general and the structural basis for the broad catalytic activity, strict substrate specificity, and high regio-/enatio-selectivity exhibited by CPO in particular. The definitive structure of CPO-substrate complexes will also provide crucial information regarding the topology of the heme active site of CPO, the critical residues involved in catalysis, the location as well as orientation of substrate within/near active site, and eventually, the mechanisms of CPO-catalyzed regio-/enantio-selective reactions. The information extracted from such studies can serve as a lighthouse in the design of more efficient CPO mutants that target specific substrates and produce custom products that are difficult to obtain with traditional organic synthesis under mild conditions. Unfortunately, the structural information about CPO-substrate complexes remains surprisingly scarce despite the great efforts made during the past few decades with the application of the most powerful techniques available such NMR spectroscopy and X-ray crystallography.

It is generally believed that X-ray crystallography is the most authoritative techniques for establishing the three-dimensional structure of proteins and protein-substrate complexes. The crystal structure of CPO resolved by Poulos and coworkers has demonstrated the presence of a substrate-binding site with a channel above the heme that enables access of organic substrates to the oxoferryl oxygen of CPO compound I [46]. It is well known that substrate binding would result in noticeable structural rearrangements of the protein. Contrary to this general agreement, the structures of CPO-ligand complexes are indistinguishable from that of the ligand-free protein. Furthermore, the crystal structure of CPO complexed with its natural substrate, 1,3-cyclopentanedione (CPDO), (PDB code: 2CIX) revealed another astonishing scenario in that the active methylene group of CPDO is not pointing towards the heme iron. This structure is actually in good agreement with the results reported from an NMR relaxation study of CPO-CPDO complex in solution. To my knowledge, 2CIX is the only crystal structure of CPO complexed with a substrate. The limited structural data on CPO-substrate complexes is mainly the result of the difficulty of diffusing organic substrates into CPO crystals as explained[115].

Nuclear magnetic resonance (NMR) spectroscopy is an alternative technique to X-ray crystallography for investigating the structural information of enzymes and their complexes with substrates in solution. Especially, in heme proteins, the enhanced nuclear relaxation induced by the paramagnetism of the heme can be successfully used to deduce the structure and stability of enzyme-substrate complex. Many reports in

literature have demonstrated that NMR relaxation studies can be used in extracting the structural features of CPO complexed with different classes of substrates, for example, phenols [116], sulfides [117], and the natural chlorination substrate, CPDO [118].

Along with the advances in computational chemistry, molecular mechanics studies have become a popular complement to NMR and X-ray studies in understanding heme proteins and their interactions with substrates at the atomic level [114]. For solution studies, distances between substrate and the heme iron of protein can be determined by NMR measurements. The distance obtained can be used as restraints in simulation studies using a simulated annealing protocol. The simulation method has been successfully applied to the investigation of substrate binding to several hemoproteins [119]. The success of these studies has encouraged us to undertake this project of investigating the mechanisms of CPO-catalyzed enantioselective epoxidation of a few selected olefins (Figure 3.1) using both NMR and computational techniques.

The CPO-catalyzed epoxidation of the olefins chosen for this study was first reported in by Hager and his coworkers in 1996 [120]. It is noted that the epoxidation of these structurally closely related olefins yields the corresponding epoxides with strikingly different enantioselectivity. The reactivity of the olefins also varies depending on the nature and the position of substituents along the double bond. However, to our best knowledge, the structural basis for CPO-catalyzed enantioselective epoxidation of substituted olefins remains undefined. Therefore, a detailed structural characterization of CPO-olefin complexes would offer fresh insight into the mechanisms of CPO-

catalyzed epoxidations and solve the long-lasting mystery of the dramatically different product distribution from epoxidation of these structurally closely related olefins.

The aims of the present work are to reveal the orientation of the selected substituted olefin binding at the active site of CPO, to identify the residues involved in the formation of CPO-olefin complex, and to elucidate the mechanism of CPO-catalyzed enantioselective epoxidation of olefins. The interaction of the substituted olefins with CPO was probed using longitudinal NMR relaxation and two computational methods, molecular docking and simulated annealing. The dissociation constant of CPO-olefin complex and the distances between the protons of olefin and the heme iron of CPO are obtained. The effect of pH and halide ion on the binding of olefin with CPO is also inspected. Simulated annealing and molecular docking of the substituted olefins in the active center of CPO are provided. Our results showed that a complex with a KD of approximately 21 mM is formed between CPO and the selected olefins with 3-H of the olefin pointing towards the heme iron. The simulation structural feature satisfactorily explains the unusual product observed from CPO-catalyzed epoxidation of the selected olefins. It is concluded that formation of CPO-olefin complex is responsible for the escorted delivery of oxygen from CPO compound I to the preferred side of the double bound in the substituted olefins, resulting in the observed enantioselectivity in product distribution.

3.2 Materials and Methods

3.2.1   To estasblish the three-dimensional structure of the complexes formed between CPO and some selected substrates

Structural similarity of some known substrates compared to their dramatically different stereochemistry of the corresponding products serviced as our guideline in the selection of the substrates used for this study. Specifically, we will use ethyl 3-methylbut-3-enoate (L-1), 2-methylallyl propionate (L-2), and ethyl 3-methylbut-3-enoate (L-3) (Figure 3.1) as substrates to investigate the mechanism of CPO catalyzed epoxidations. NMR and UV-Vis spectrophotometry will be used to detect the formation and characterization of CPO-substrate complexes.

3-methylbut-3-enoate   2-methylallyl propionate   3-methylbut-3-en-1-yl
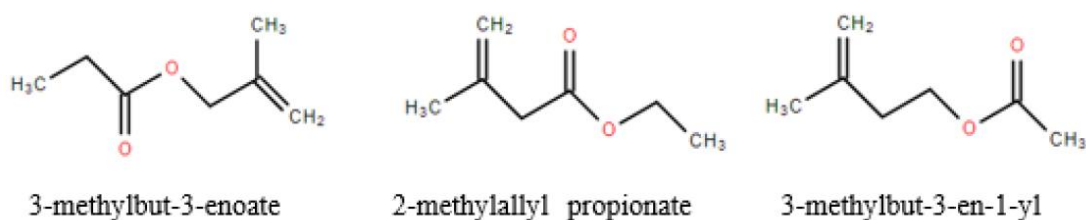
Figure 3.1 The substrates selected for this project

3.2.2 *Caldariomyces fumago's* Expression and Purification

A piece of the colonized acrylamide plates was cut and inoculated in a 250-mL flask at 25 °C (the optimal temperature for CPO expression) and 250 rpm for 5 days (Figure 3.2). Different assays, described in the later section, was used to monitor the status of CPO production. The 250-mL cultures was transferred to the 2-L flask and incubated at 25 °C and 250 rpm for 5 more days. Afterward, acetone precipitation was used to separate protein from impurities [53]. The filtrate was concentrated to 30 mL through

43

an Amicon high pressure cells using a membrane of 30 kDa cutoffs. After concentrating

the medium containing CPO, the sample was dialyzed against 4 L buffer A (25 mM

phosphate buffer, pH 5.9) overnight with at least one-time change of buffer. The

dialyzed CPO was filtered through a 0.45 μm filter and subjected to two types of

chromatography, ion-exchange and size exclusion [54]. For ion-exchange, the column

was packed with diethylaminoethanol (DEAE) sepharose and equilibrate with buffer A.

The protein was loaded onto the column and washed with buffer A. Elution was done

by gradually increasing NaCl concentration (0-0.5 M) of the buffer. When the protein

elutes, a red color was seen. Eluted fractions with Reinheitzahl (Rz, A398/A278) values

above 1.0 were combined and concentrated to approximately 1 mL through a Millipore

centrifugal filter unit (30,000 Da cutoff)). The concentrated sample will be purified

through a size exclusion column packed with Sephadex G75 resin and washed with

buffer A. Similarly, the eluted fractions with the highest Rz-value was combined and

concentrated for use in substrate binding experiments.
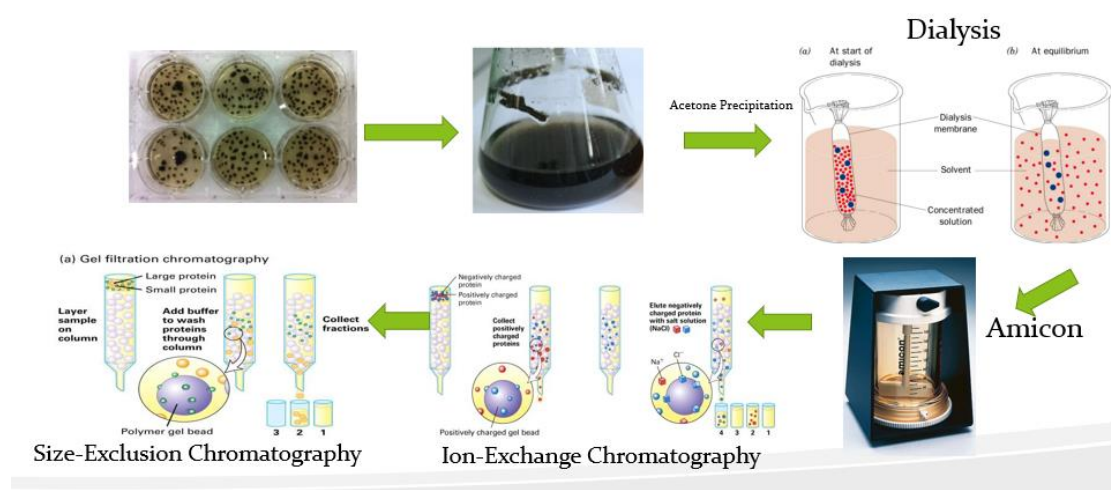
Figure 3.2 Chloroperoxidase's expression and purification

3.2.3 MCD Assay

The MCD assay is commonly used for determining the chlorination activity of chloroperoxidase [55]. The assay monitors the chlorination of monochlorodimedone (MCD) to dichlorodimedone (Figure 3.3). The reaction system composed of CPO in 100 mM potassium-phosphate buffer containing 20 mM KCl and 0.17 mM MCD (pH range 2.5- 5.0). The reaction was initiated by the addition of 2.2 mM H_2O_2 and the rate of chlorination was monitored at 278 nm where MCD absorbs.
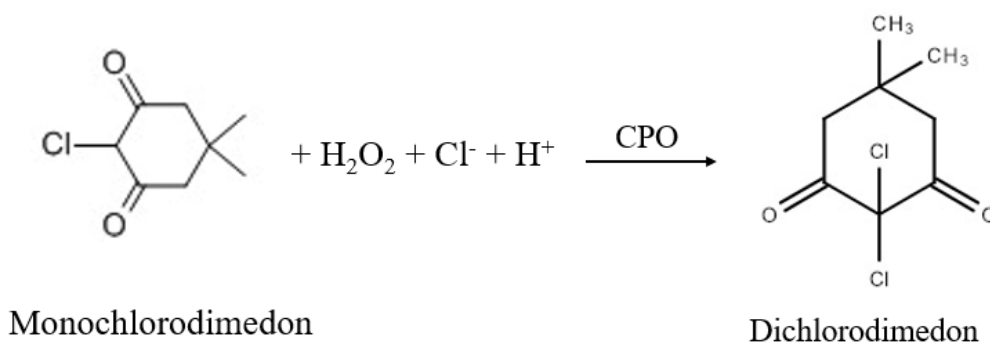
Figure 3.3 Enzyme Activity Assay (MCD Assay)

3.2.4 Synthesis and Characterization of the Selected Compounds

As outlined in **Scheme 1**, esterification of 2-methyl-2-propen-1-ol with propionic anhydride afforded compound L-1. Using the same condition, compound L-3 was synthesized by esterification of 2 methyl-2-propen-1-ol with acetyl anhydride as shown in **Scheme 3**. To synthesis compound L-2, 3-methyl-3-buten-1-ol was oxidized with Jones reagent and esterified with ethanol as depicted in **Scheme 2**. The yield of this route is higher than that of the Wittig reaction and esterification from the material 3-oxobutanoic acid. Detailed synthesis procedure is described below.
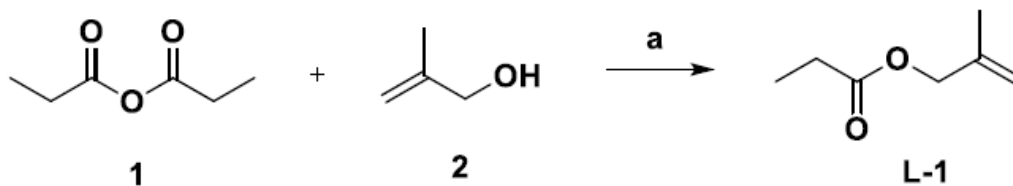
Scheme 1, *conditions and reagents used for the synthesis of L-1*: a) pyridine, dichloromethane, 40ºC, 8~9h, yield: 90%
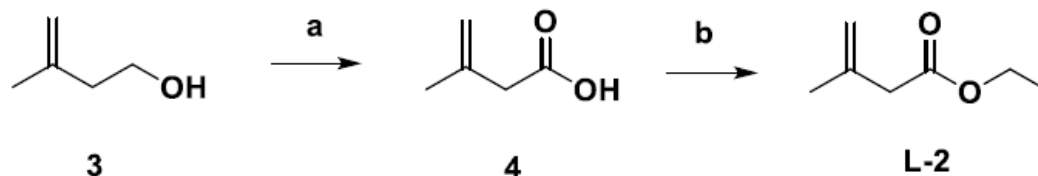
Scheme 2, *conditions and reagents used for the synthesis of L-2*: a) Jones reagent, acetone, 0 ºC, 1h, yield: 86%; b) ethanol, methanesulfonic acid, 70 ºC, 2h, yield: 31%
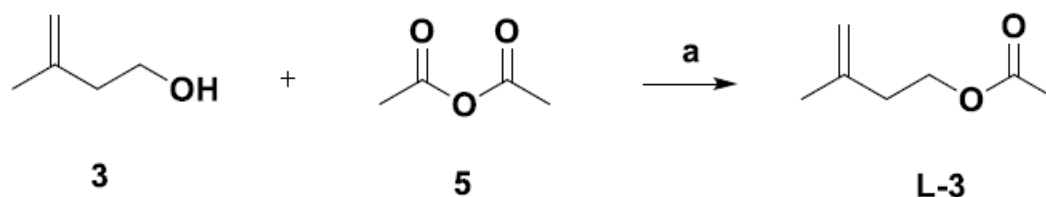
Scheme 3, *conditions and reagents used for the synthesis of L-3*: a) pyridine, dichloromethane, 40 ºC, 8~9h, yield: 81%

To the solution of 2-methyl-2-propen-1-ol (50.0g, 0.693 mol), propionic anhydride (108g, 0.832 mol), dichloromethane (1L) at 0 ℃, the pyridine (109g, 1.38 mol) dissolved in 100 ml dichloromethane was added dropwise. The mixture was reacted for 8~9 h at 40 ℃. After the reaction, monitored by TLC (petroleum ether/AcOEt = 3:1), was completed, the mixture was extracted by 4 mol/L HCl solution (400 mL ×10), washed by saturated sodium bicarbonate solution (400 mL ×7), water (400 mL ×2), saturated brines (400 mL ×2) and dried by anhydrous sodium sulfate. After filtration, evaporation and distillation, the final production was obtained as a clear, colorless oil

80.0g (90%). Proton NMR (Figure 3.4) analysis confirmed the identity of the product.
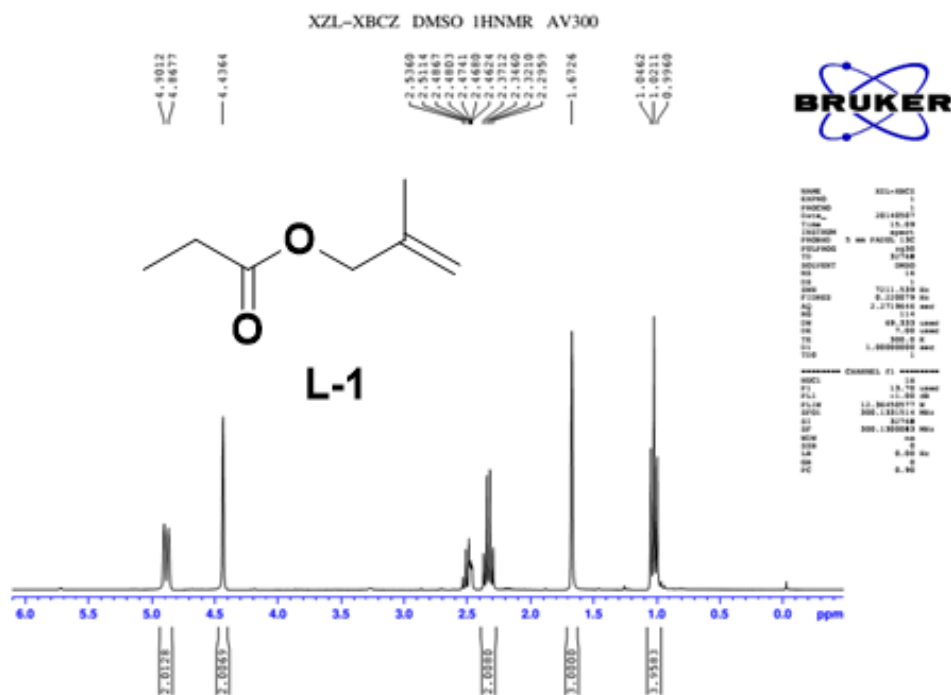
Figure 3.4 Proton NMR spectra of 2-methyl-2-propen-1-ol. H NMR (300 MHz, DMSO-d_6) δ 4.90~4.86 (2H, d, J=12.0Hz, -C=CH$_2$), 4.43 (2H, s, -O-CH$_2$-), 2.37~2.26 (2H, q, J$_1$=7.5Hz, CH$_3$-CH$_2$-CO-), 1.67 (3H, s, CH$_3$-C=CH$_2$), 1.02 (3H, t, J=7.5 Hz, CH$_3$-CH$_2$-CO-) ppm.

Compound L-2 was obtained following the following procedure. To the solution of 3-methyl-3-buten-1-ol (10 mL, 0.099 mol) and acetone 500 mL at 0 ℃, the Jones reagent (52 mL, 0.138 mol) was added dropwise. The reaction was stirred for 1h at 0 ℃. After the reaction, monitored by TLC, was complete, the 2N NaOH solution was added and stirred for 30min. then, the mixture was adjusted by 4 mol/L HCl solution to pH of 3~4, extracted by diethyl ether (300 mL ×7), washed by saturated brines (300 mL ×2) and dried by anhydrous sodium sulfate. After filtration, evaporation, and distillation, the intermediate of 3-methyl-3-butenoic acid was provided as a clear, light yellow oil 10.3g (86 %). The mixture of 3-methyl-3-butenoic acid (5g, 0.05 mole) and methane

sulfonic acid (1 mL) in ethanol (30 mL) was stirred for 2 h at 70 ℃. After the reaction, monitored by TLC, was complete, the mixture was extracted by n-pentane (50 mL ×5), washed by water (50 mL ×5), saturated brines (50 mL ×5) and dried by anhydrous sodium sulfate. After filtration, evaporation and distillation, the product was obtained as a clear, light yellow oil with a total of 2.01g (31 %) as confirmed by proton NMR analysis (Figure 3.5).
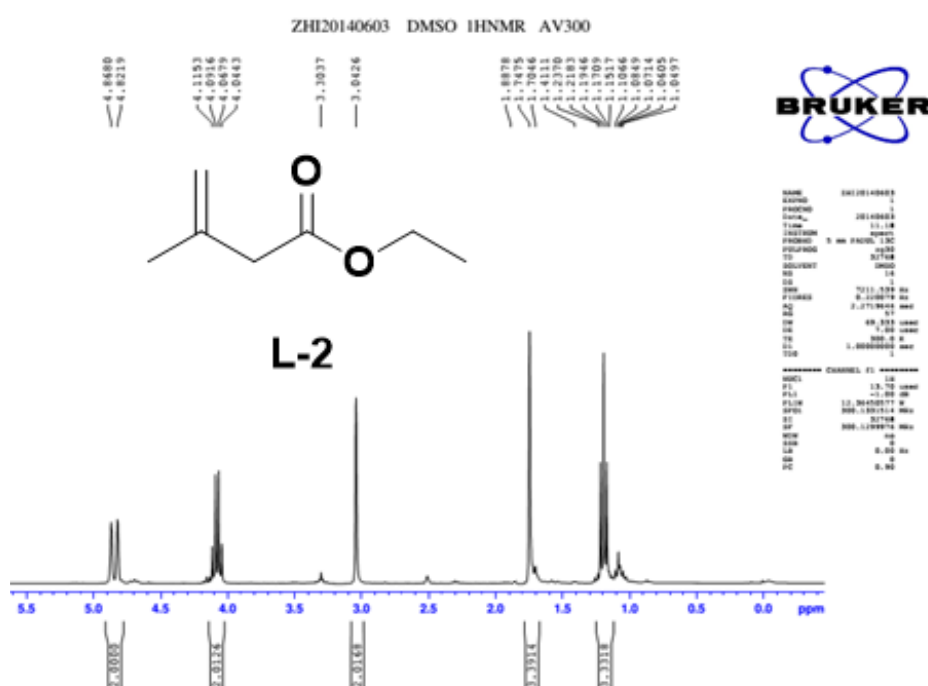
Figure 3.5 Proton NMR spectra of 2-methylallyl propionate. H NMR (300 MHz, DMSO-d$_6$) δ 4.86~4.82 (2H, d, J=10.0 Hz, -C=CH$_2$), 4.11~4.04 (2H, q, J$_1$=7.11 Hz, CH$_3$-CH$_2$-O-), 3.04 (2H, s, -CO-CH$_2$-), 1.74 (3H, s, CH$_3$-C=CH$_2$), 1.19 (3H, t, J=7.11 Hz, CH$_3$-CH$_2$-O-) ppm.

The following procedure was employed to synthesize compound L-3. To the solution of 2-methyl-2-propen-1-ol (25.0g, 0.290 mol), acetic anhydride (37.6g, 0.348 mol), dichloromethane (300 mL) at 0 ℃, the pyridine (45.8g, 0.580 mol) dissolved in 50 mL dichloromethane was added dropwise. The mixture was reacted for 8~9 h at 40 ℃.

After the reaction, monitored by TLC (petroleum ether/AcOEt = 3:1), was complete, the mixture was extracted by 4 mol/L HCl solution (200 mL ×10), washed by saturated sodium bicarbonate solution (200 mL ×7), water (200 mL ×2), saturated brines (200 mL ×2) and dried by anhydrous sodium sulfate. After filtration, evaporation and distillation, the final product was obtained as a clear, colorless oil with a total yield of 31.3g (81%). The structure of the product was confirmed with proton NMR analysis as shown in Fig. 3.6.
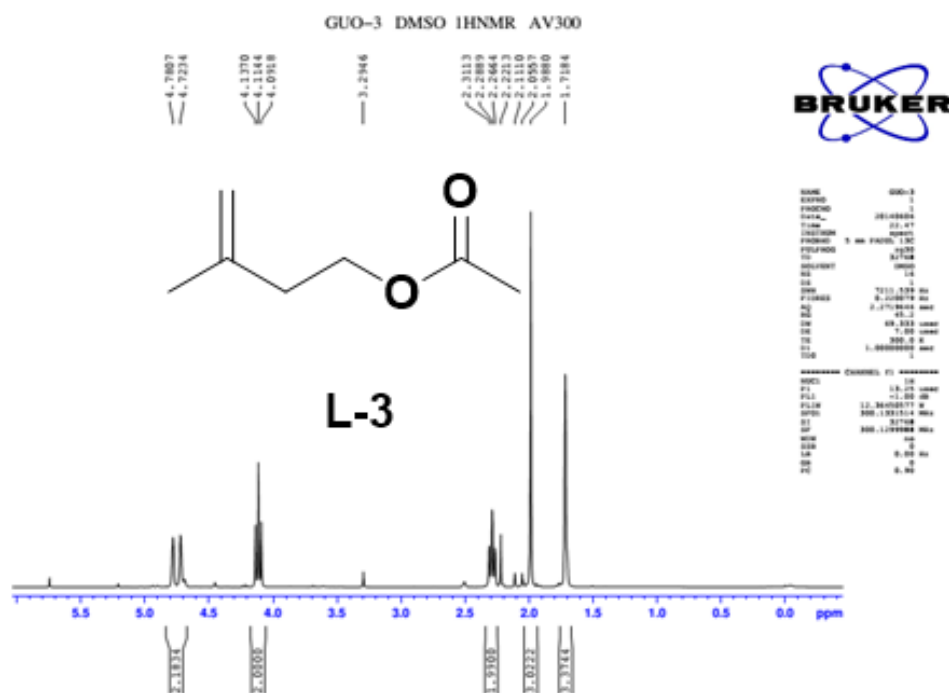
Figure 3.6 Proton NMR spectra of 3-methylbut-3-en-1-yl acetate. H NMR (300 MHz, DMSO-d$_6$) δ 4.78~4.72 (2H, d, J=17.1Hz, -C=CH$_2$), 4.11 (2H, t, J=6.7 Hz, -O-CH$_2$-CH$_2$-), 2.31 (2H, t, J=6.7 Hz, -O-CH$_2$-CH$_2$-), 1.98 (3H, s, CH$_3$-CO-), 1.71 (3H, s, CH$_3$-C=CH$_2$) ppm.

3.2.6 NMR relaxation of the CPO-substrate Complexes

Proton NMR relaxation measurements were conducted on a Bruker Avance 600 MHz NMR spectrometer at 298.0 K. The NMR data were processed using Topspin,

version 2.1.The longitudinal relaxation time (T_1) was determined using the standard inversion-recovery method with 180°-τ-90° pulse sequence [56]. Eleven spectra were recorded for each sample, with the inter-pulse delay τ ranging from 0.05 to 10.0 s. For each spectrum, 16 scans were acquired. The T_1 values were calculated by fitting Equation 3.1, where τ is the interval between 180° and 90° pulses, M_z is the Z-component of nuclear magnetization (represented by the intensity of the peak) when the interval is τ, M_0 is the is the Z-component of the nuclear magnetization when the interval is infinite, and ρ is a parameter that equals to 2.0 at an exactly 180° pulse.

$$M_z = M_0(1 - \rho e^{-\frac{\tau}{T_1}})$$

(3.1)

The samples used for NMR experiments contained 2-10 mM substrates and 0.1 mM CPO in 100 mM phosphate buffer with 99.9% D_2O. The final volume of all NMR samples was 500 μL.

3.2.7 Dissociation constants of CPO- L-2 complex

The longitudinal relaxation rate (T_{1obs}^{-1}) is the weighted average of the relaxation rates of the free substrate (T_{1f}^{-1}) and the bound substrate (T_b^{-1}) [57]. Thus, the relaxation-time values (T_{1obs}^{-1}, T_{1f}^{-1}, and T_b^{-1}) are related as shown in Equation 3.2 when only one molecule of substrate binds to a molecule of enzyme, where T_{1obs} is the relaxation time of the substrates obtained from the relaxation experiment, T_{1f} is the relaxation time of substrates obtained from the relaxation experiment in the absence of CPO, T_{1b} is the relaxation time of the CPO bound substrates, K_D is the dissociation

constant of CPO substrates complex, E_0 is the initial CPO concentration, and S_0 is the

initial substrates concentration.

$$E_0[\frac{1}{T_{1obs}} - \frac{1}{T_{1f}}]^{-1} = K_D[\frac{1}{T_{1b}} - \frac{1}{T_{1f}}]^{-1} + S_0[\frac{1}{T_{1b}} - \frac{1}{T_{1f}}]^{-1}$$

(3.2)

3.3 Results & Discussion

3.3.1 Proton NMR spectrum of substrate L-2 in the presence of chloroperoxidase (CPO)

The H-NMR spectra of 5.0 mM substrate L-2 in the absence and presence of varying amount (0.01, 0.05, 0.08, 0.1, and 0.15 mM) of CPO is shown in Figure 3.8. The five main peaks can be easily assigned, based on the splitting pattern and shift positions, to the protons of the substrate L-2 in the absence of CPO (Figure 3.7) 1.19 ppm (1-H), 4.11 ppm (2-H), 3.04 ppm (3-H), 1.75 ppm (5-H). The 4-H was not observed due to overlap with the large peak of H_2O.
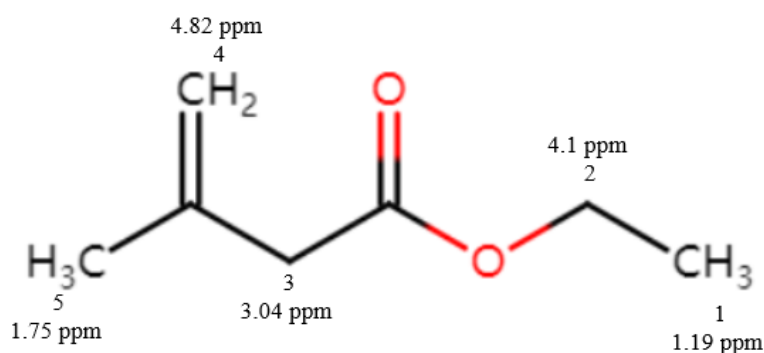
Figure 3.7 The structure of substrate L-2, proton number assignment is shown. 1.19 ppm (1-H), 4.11 ppm (2-H), 3.04 ppm (3-H), 1.75 ppm (5-H).

As the concentration of CPO increased from 0.01 to 0.15 mM, the linewidth of the 1- proton increased from 21.73 to 27.89 Hz (Figure 3.8). The linewidth of 3-H also increased dramatically from 10.75 to 17.05 Hz as the concentration of CPO was increased. In contrast, the other peaks were less broadened than those of the 1- and 3-H. For instance, the linewidth of 2-H increased gradually from 27.43 to 30.35 Hz in the range of the CPO concentration tested. The shorter distances suggests that protons 1-H or 3-H are closer to the heme iron than other protons of the substrate.
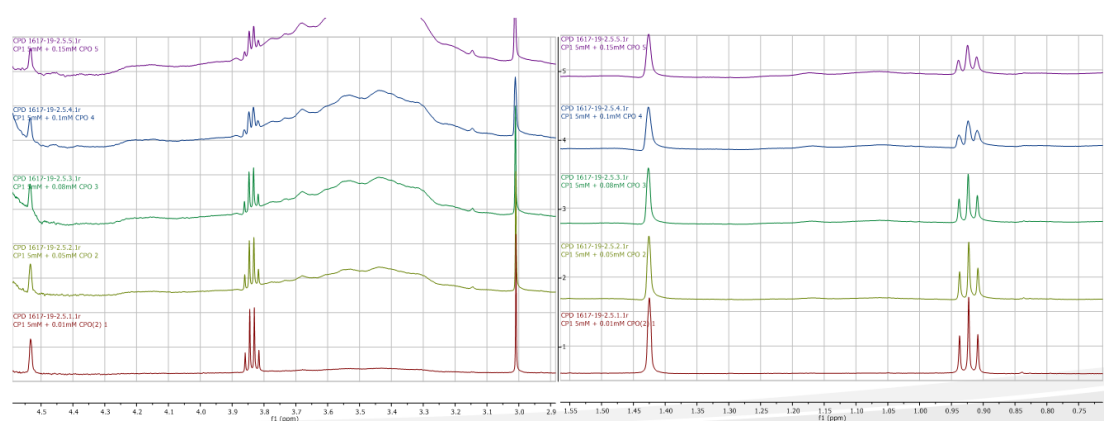
Figure 3.8 The effect of the concentration of CPO on the proton NMR spectra of substrate L-2. The spectra were obtained in 100 mM deuterated phosphate buffer (pH 5.9) containing 5.0 mM L-2 and varying concentrations of CPO.

3.3.2 Dissociation constant of CPO- L-2 complex

To evaluate the binding affinity between CPO and L-2, the longitudinal relaxation time (T_1) of L-2 protons was measured in the presence of 0.1 mM CPO and different concentrations of L-2 (2.0-10.0 mM) at pH 5.9. Figure 3.9 shows the exponential fit of signal intensities (Mz) as a function of the delay time (τ) as defined in Equation 3.1, using the resonance at 1.19 ppm (1-H) as an example. Similar fits are obtained for other

protons of L-2. Therefore, T_{1obs} of 1-H (Figure 3.9A-E) can be obtained from Equation 2.1 (2.38s, 2.58s, 2.75s, 2.89 s, and 3.05s, respectively). The increase in T_{1obs} is attributed to the increase of the fraction of free L-2 as its concentration is increased as show in a plot of $E_0[1/T_{1obs} - 1/T_{1f}]^{-1}$ versus S_0 for 1-H. The fitted straight line demonstrates the reliability of the data ($R^2=0.9741$). The K_D value can be calculated as the intercept of the fitted line divided by its slope using Equation 3.2. The K_D calculated from Figure 3.9F was approximately 16 mM.(2-H is 6 mM, 3-H is 22 mM, 5-H is 32 mM)
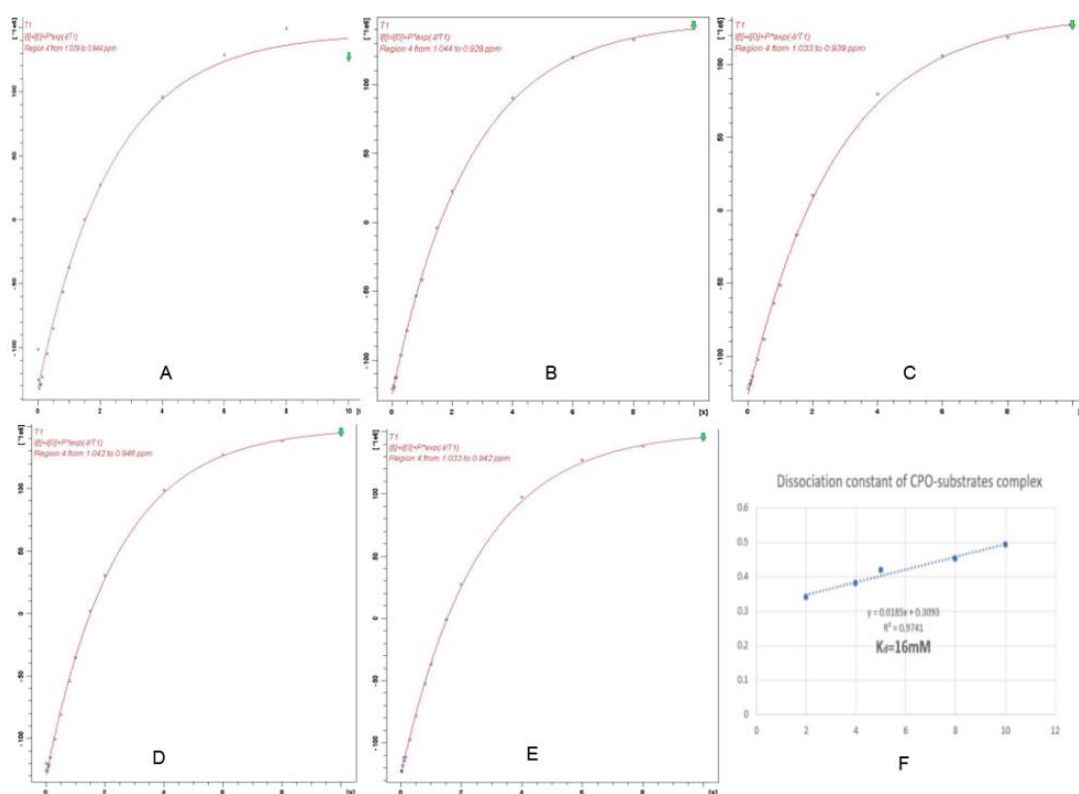
Figure 3.9 NMR relaxation experiments for 1-H of substrate L-2 in the presence of CPO. (A-E) The results were obtained in 100 mM deuterated phosphate buffer (pH 5.9) containing 0.1 mM CPO and (A) 2.0 mM·L^{-2}, (B) 4.0 mM·L^{-2}, (C) 5.0 mM·L^{-2}, (D) 8.0 mM·L^{-2}, and (E) 10.0 mM·L^{-2}. (F) The plot of $E_0[1/T_{1obs} - 1/T_{1f}]^{-1}$ as a function of the concentration of L-2 (S_0).

3.3.3 Distances between CPO Heme Iron and the Protons of L-2

To reveal the orientation of L-2 in the active site of CPO, paramagnetically induced NMR relaxation of L-2 in the presence of CPO was used to calculate the distance between the heme iron and the protons of L-2. Table 3.1 lists the NMR relaxation time, T_{1b}, and the calculated distances between the protons of L-2 and the heme iron of CPO. These distances are consistent with those obtained for alky phenyl sulfides (8.0-10.9 Å), phenols (5.6-9.3 Å), CPDO (7.1 Å), and L-2 binding with CPO. Examination of Table 3.1 revealed that the distance between the heme iron of CPO and proton 3 of L-2 is the shortest. This position happens to be the location at which the epoxidation takes place, indicating that the epoxidation of L-2 proceeds by a direct insertion of oxygen from the oxyferryl intermediates of CPO to the double bond of the olefin. Furthermore, the use of these distance constraints in advanced computational methods such as simulated annealing can provide the precise orientation and position of L-2 in the active site of CPO, which will be presented in Distance-Restrained Model of CPO Complexed with L-2.

Table 3.1. The dissociation constant (K_D) of CPO-L-2 complex and the distances (r) between the protons of L-2 and CPO heme iron[a]

position	δ (ppm)	T_{1b} (s)	r (Å)	K_D (mM)
2-H	4.07	2.2×10^{-3}	9.0	6
3-H	3.04	1.9×10^{-4}	6.6	22
5-H	1.74	2.6×10^{-3}	9.8	32
1-H	1.19	2.7×10^{-2}	11	16

[a] The relaxation experiments were performed in 50 mM deuterated phosphate

buffer (pH 5.9) 0.1 mM CPO by changing the concentration of L-2 from 2 to 10 mM.
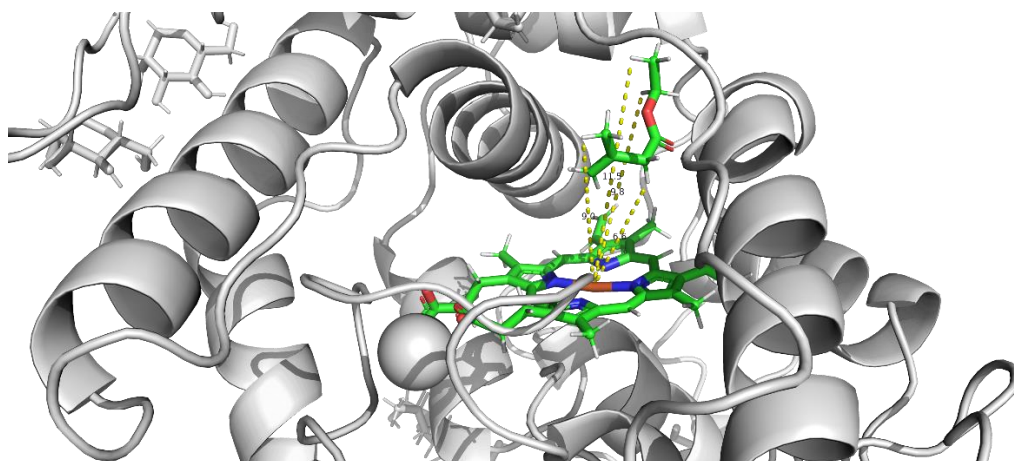
Figure 3.10 Distance-restrained model of L-2 in the active site of CPO, to differentiate the protein residues from the substrate, the L-2 molecules are colored green, the oxygens are colored red.

On the basis of our docking results (Figure 3.10), the distance of 1-H was 11 Å, the

2-H was 9 Å and the 5-H was 9.8 Å from the hem iron center. The lowest energy results

are also matched to the NMR relaxation measurements, with 3-H (6.6 Å) being the

closest to the heme iron.
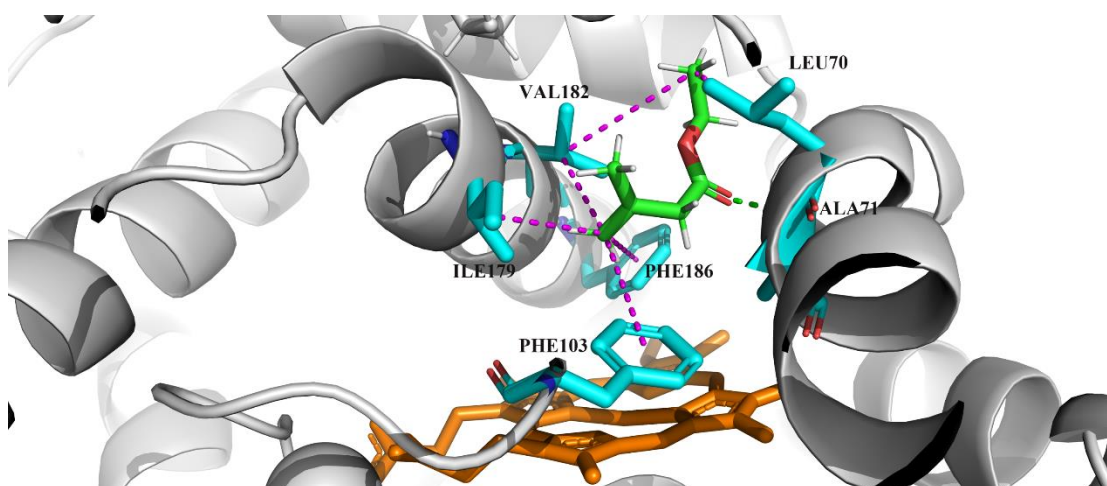
Figure 3.11 Distance-restrained model of L-2 in the active site of CPO. To differentiate the protein residues from the substrate, the L-2 molecules are colored green, the heme is colored brown, and the carbons of the residues are colored blue.

It is observed that residues close of L-2 are PHE103, PHE186, VAL182, ILE179,

LEU70, ALA71. Week forces between L-2 and these residues in CPO help to stabilize the complex formed between CPO and L-2, orienting L-2 in a position ensuring the formation of the observed enantioselectivity in production distribution.

3.4 Conclusion

The work presented here provides insights into the mechanism of the CPO-catalzyed enantioselective oxidation of L-2. Association of L-2 with CPO was confirmed from both linewidth and longitudinal relaxation time measurements of the proton NMR signals of L-2. Based on the dissociation constant (K_D) of CPO L-2 complex at pH 5.9, the K_D values obtained from the relaxation property of different protons in L-2 are quite consistent, further proving the validity of the relaxation method in probing the structural properties of hemoprotein-substrate complexes.

CHAPTER IV.

RATIONAL MODIFICATION OF DANOFLOXACIN INTRODUCES NOVEL ANTICANCER ACTIVITY

4.1 Background

4.1.1 Development of lung cancer treatment

Lung cancer is one of the most common cancers and the leading cause of cancer-related deaths worldwide. Due to the lack of clinical symptoms and effective screening programs, most lung cancer is diagnosed in the advanced stage. However, the treatment and prognosis of lung cancer depend on accurate staging of the disease [58, 59]. Non-small cell lung cancer (NSCLC), which includes adenocarcinoma (glandular formation), squamous cell carcinoma, and large cell carcinoma tissue subtypes, accounts for approximately 85% of all new lung cancer cases [60]. Lung cancer accounts for more than 1.8 million new cancer diagnoses worldwide each year (13% of all cancer diagnoses) and 1.6 million cancer-related deaths (19.4% of the total) [61]. In the United States, there were an estimated 224,210 new lung cancer cases and 159,260 deaths in 2014. In Europe, there were an estimated 410,000 new lung cancer cases and 353,000 deaths in 2012 [62]. While lung cancer rates are falling in developed countries, they are rising in less developed parts of the world (Africa, South America, eastern Europe and China). In fact, 58% of the 1.8 million new cases worldwide in 2012 occurred in underdeveloped regions. One possible explanation for the findings is that smoking rules in these countries are less strict. However, lung cancer rates are highest in North

America, Europe, Australia, New Zealand and China [63]. Despite recent advances in

therapeutic regimen, the curative effect is not so inspiring because of the poor outcome

[64]. Consequently, it is indispensable to develop more effective therapies against lung

cancer.
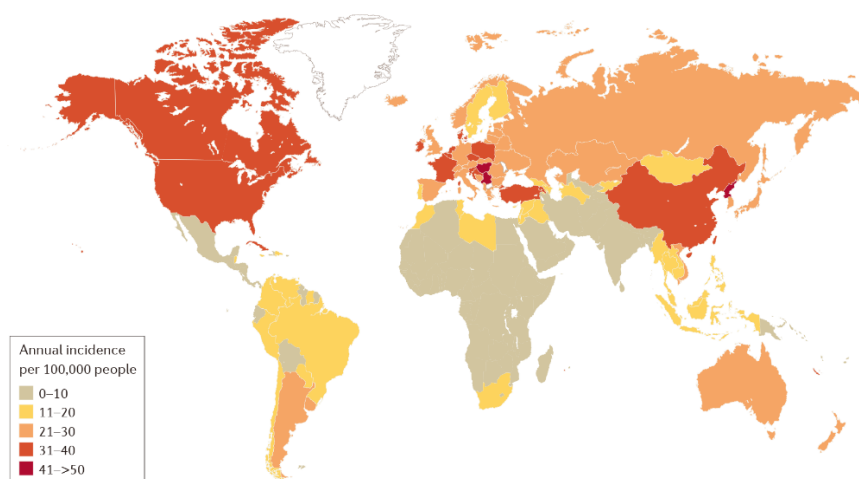
Fiugre 4.1 Annual incidence of lung cancer per 100,000 people [60].

4.1.2 Bim-mediated apoptosis in cancer cells

There are two major apoptosis pathways, the extrinsic and intrinsic (mitochondria-

associated) pathways, in cytoplasm. Intrinsic apoptosis could be regulated via

mitochondrial pathway characterized by the release of cytochrome c (Cyt c) and

activation of caspase [65]. The Bcl-2 family proteins, anti-apoptotic proteins (such as

Bcl-2 and Bcl-xL), pro-apoptotic proteins (such as Bax and Bak), and Bcl-2 homology

3-only (BH3-only) proteins (such as Bim, Bad and Puma), play a crucial role in intrinsic

apoptotic process. The apoptotic stimuli activate specific BH3-only proteins to engage

anti-apoptotic proteins and release downstream pro-apoptotic proteins, leading to

increased mitochondrial outer membrane permeability and eventually cell death

induced by triggering caspase cascade [66]. Subsequently, cytochrome c is released

from mitochondria into cytoplasm which can trigger the caspase cascade, leading to

cell death. Bim acts as direct activators of Bax and Bak by interacting with them. Bim

is also involved in p53-dependent and p53-independent apoptosis [67]. Recent studies

have implicated that Bim may serve as a potential target for anti-cancer

chemotherapeutics since it plays an important role in apoptosis [68, 69].
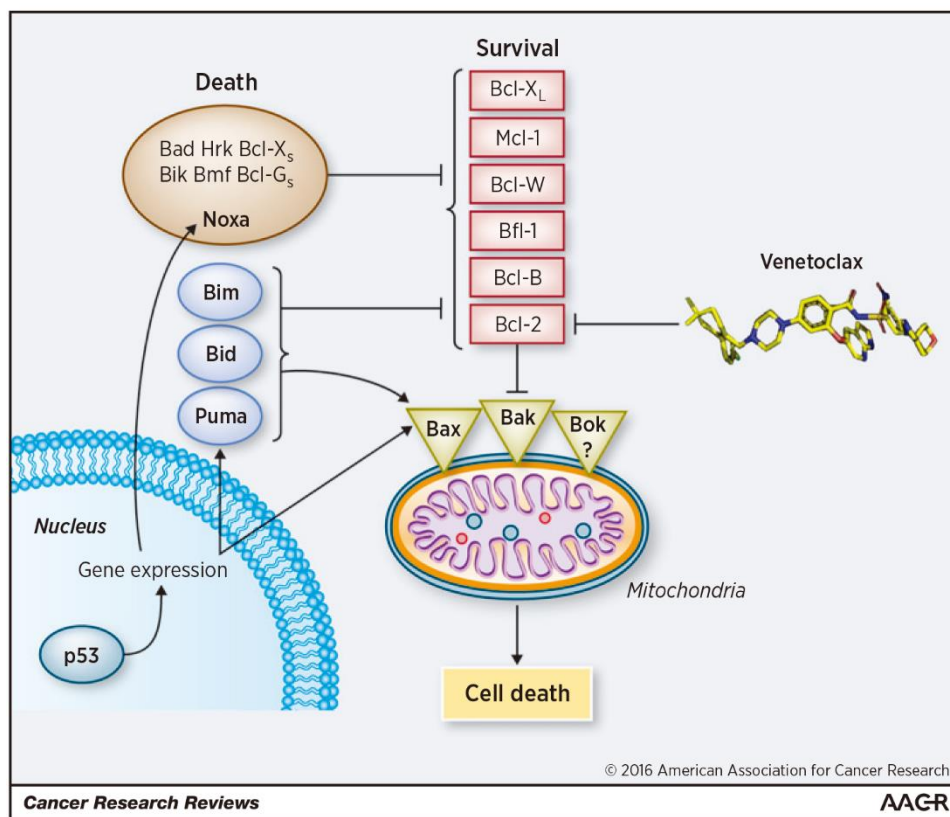
Fiugre 4.2 Interactions among Bcl-2 family proteins [70].

4.1.3 Transcriptional outputs of FoxO activity

The FOXO subfamily of transcription factors is evolutionarily conserved, including

FOXO1, FOXO3a, FOXO4, and FOXO6 [71]. FOXO proteins can regulate multiple

target genes involved in tumor suppression, such as Bim, FasL, p27kip1, cyclin D and

GADD45 [72-75]. FOXO3a, the most important transcription factor in FOXO family, was phosphorylated by Akt at Thr32, Ser253 and Ser315, leading to FOXO3a translocate from nucleus to cytoplasm and is consequently degraded by proteasome [76]. The proteasome inhibitor MG132 increases the stability of FOXO3a and induces apoptosis in thyroid cancer cell [77]. In addition, studies have reported that FOXO3a is a substrate for autophagy [78]. This suggests that FOXO3a degradation depends not only on the proteasome pathway, but also on autophagy activation.
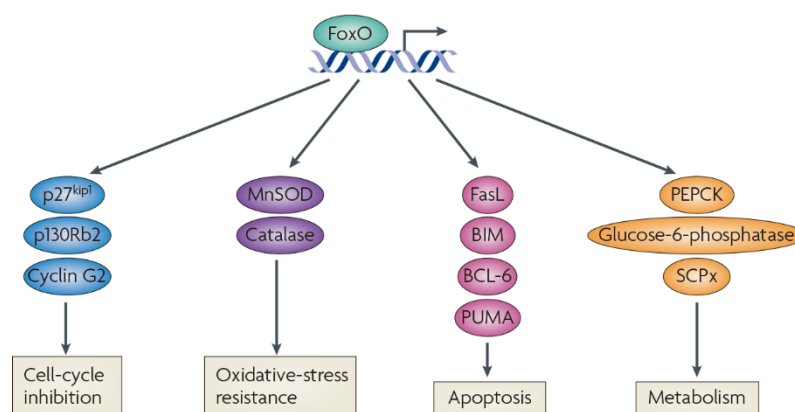
Fiugre 4.3 Increased FoxO activity participates in several cellular processes [79].

4.1.4 A modified danofloxacin LZ101 with potential anticancer activity

LZ-101 is a derivative of danofloxacin that has been developed specifically for veterinary use [80]. Danofloxacin has been widely used for the treatment for respiratory disease and urinary tract infections in animals, such as chicken and buffalo [81, 82]. However, studies have shown that danofloxacin induces apoptosis by inducing oxidative stress in renal tubular cells, epithelial cell line (LLC-PK1). This study showed that danofloxacin exhibited apoptosis-inducing effects. While the effect of danofloxacin

derivative LZ-101 on apoptosis is still unclear. This study demonstrated that LZ-101 induced apoptosis in A549 human non-small cell lung cancer cells and inhibited tumor growth with low systemic toxicity in BALB/c mice bearing A549 tumor through mitochondria-associated pathway by stabilizing FOXO3a via blocking autophagy flux. Our results showed that LZ-101 exhibits remarkable anti-tumor activity and is promising to serve as an effective candidate for the treatment of human non-small cell lung cancer.

4.2 Materials and Methods

4.2.1 Rationale of the modification

DNA topoisomerase I (Top I) is an important enzyme for tumor growth. Traditional Top I inhibitors, such as the natural alkaloid camptothecin (CPT), can bind and stabilize a binary DNA-Top I complex containing a single-strand nick, thus inhibiting DNA replication and eventually causing cell death. Despite the initial success of CPT in preclinical studies, the low water-solubility of CPT severely limits its use. Therefore, tremendous efforts have been made to develop more water-soluble analogues of CPT, such as topotecan (TPT) and irinotecan, which are derivatives of 10-hydroxycamptothecin (HCPT) and have been approved for clinical treatment of cancer patients. However, the therapeutic potential of CPT and its derivatives is severely hampered by their rapid deactivation by lactone ring hydrolysis at physiological pH. In addition to CPT and its derivatives, metabolically stable non-CPT derivatives, such as indolocarbazoles and indenoisoquinolines, have been developed, some of which are

under clinical evaluation. Given the success of these non-CPT derivatives, we believe

that non- CPT Top I inhibitors have better chemical stability because they lack a lactone

ring in their skeleton. We attempted to synthesize compounds lacking CPT lactone ring,

and converted the rigid framework of CPT into the single bond binding of quinolones

and benzimidazole groups. Therefore, we modified danofloxacin to synthesize its

derivative LZ101, and to study the anti-tumor effect of LZ101.

4.2.2 Structural Characterization of the Modified Danofloxacin--LZ101

We kept the main group of danofloxacin, including the basic structure of 4-oxo-

quinoline, the 2,5-Diaza-bicyclo[2.2.1]heptane, the fluorine atom, and the ternary

carbon ring on the nitrogen atom. The carboxyl group at the C-3 position was modified

into cyanosubstituted benzimidazole to improve the activity.
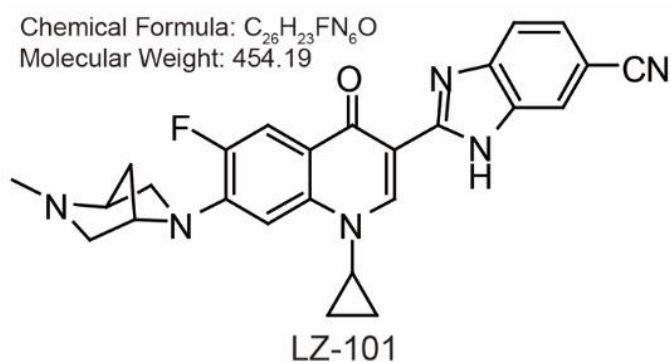
Figure 4.4 The molecular structure of LZ-101.

4.2.3 *In-vitro* Study

4.2.3.1 Cell culture

Human non-small cell lung cancer cell line H460 and H1299 cells were cultured in

RPMI-1640 medium (Gibco, Waltham, USA) and A549 cells were cultured in F-12

62

medium (Gibco, Waltham, USA) supplemented with 10% fetal bovine serum (Gibco, Waltham, USA), 100 U/ml penicillin and 100 U/ml streptomycin, cells were cultured in a humidified CO_2 (5%) incubator (Thermo Forma, Waltham, USA) at 37 °C.

4.2.3.2 MTT assay

Experiments were done in triplicate in a parallel manner for each concentration of LZ-101 used and the results are presented as mean ± SEM. Control cells were given culture media containing 0.1% DMSO. After incubation for 24 or 48 h, 20 μL of 5 mg/mL MTT was added to cells, and cells were incubated at 37 °C for another 4 h. The absorbance (A) was measured at 570 nm using an ELx800 automated microplate reader (BioTek Instruments, Inc.). The inhibitory ratio (%) was calculated using the following equation: inhibitory ratio (%) = (1- average absorbance of treated group / average absorbance of control group) × 100%. IC_{50} was taken as the concentration that caused 50% inhibition of cell viability and was calculated by the Logit method.

4.2.3.3 Annexin V/PI staining

A549 cells were harvested, washed, and resuspended in PBS after LZ-101 treatment, then stained with the Annexin V/PI Cell Apoptosis Detection Kit (KeyGen Biotech, Nanjing, China) according to the manufacturer's instructions. Data acquisition and analysis were performed with a Becton Dickinson FACS Calibur flow cytometer using Cell-Quest software (BD Biosciences, Franklin Lakes, USA). The cells in early stages of apoptosis were Annexin V positive and PI negative, whereas the cells in the late stages of apoptosis were both Annexin V and PI positive.

4.2.3.4 Mitochondrial transmembrane potential ($\Delta\Psi_m$) assessment

The electrical potential difference across inner membrane ($\Delta\Psi m$) was monitored using the $\Delta\Psi m$-specific fluorescent probe JC-1 (Beyotime Institute of Biotechnology, Shanghai, China) [83]. The $\Delta\Psi m$-specific fluorescent probe JC-1 exists as a monomer with an emission at 530 nm (green fluorescence) at low membrane potential but forms J-aggregates with an emission at 590 nm (red fluorescence) at higher potentials. A549 cells were treated with LZ-101 for 24 h. Cells were harvested and incubated with JC-1 for 30 min at 37 °C in the dark, then resuspended in washing buffer and relative fluorescence intensities were monitored using flow cytometry (FACSCalibur, Becton Dickinson, USA) with settings of FL1 (green) at 530 nm and FL2 (red) 585 nm.

4.2.3.5 Preparation of whole cell lysates and cytosolic and nuclear extracts

A549 cells were treated with LZ-101 at indicated concentrations for 24 h. The whole cell lysates was prepared as described [84]. Nuclear and cytosolic protein extracts were prepared using a Nuclear/Cytosol Fractionation Kit (BioVision, Mountain View, CA) according to the manufacturer's protocol. The cytosolic and nuclear fractions were reserved for immunoblot analysis. Final detection was performed with Western blots.

4.2.3.6 Mitochondrial fractionation

Mitochondrial fractionation kit (KeyGen Biotech, China) was used to get mitochondrial according to the following protocol. The cells were treated with different concentrations of LZ-101 for 24 h and 3.5×10^7 cells were incubated with 1 mL ice-

cold mitochondrial lyses buffer, then suspended and ground the cells with tight pestle on ice. The homogenate was subjected to centrifugation at 800 g for 5 min at 4 °C to remove nuclei and unbroken cells, and then added 0.5 mL supernatant to the 0.5 mL Medium Buffer in the new 1.5 mL tube gently. After centrifugation at 15,000 g for 10 min at 4 °C, the supernatant was carefully removed and collected as the cytosolic fraction and the remaining mitochondrial pellet was resuspended in the mitochondrial extraction buffer.

4.2.3.7 Western blot analysis

The whole cell lysates, cytosolic extracts, nuclear extracts and mitochondrial extracts were prepared as described above. Western blot analysis was carried out as described previously [85]. Protein samples were separated by 10% SDS-PAGE and transferred onto nitrocellulose membranes. The membranes were incubated with 1% BSA at 37℃ for 1 h and then indicated antibodies overnight at 4℃, followed by IRDye800 conjugated secondary antibody for 1 h at 37℃. Immunoreactive protein was detected with an Odyssey Scanning System (LI-COR Inc., Lincoln, Nebraska).

4.2.3.8 Immunofluorescence microscopy

For confocal imaging of fixed cells, A549 cells were used. After the appropriate treatment, cells were fixed with 4% paraformaldehyde in PBS, permeabilized with 0.5% Triton X-100, and blocked with 3% BSA for 1 h. Samples was incubated with primary antibodies (diluted 1:100) overnight at 4℃. After washed, Alexa Fluor 488 donkey anti-rabbit IgG, Alexa Fluor 594 donkey anti-rabbit IgG were used as secondary antibodies

(Invitrogen, CA, USA). Samples were observed and captured with a confocal laser scanning microscope (Olympus Corp., Tokyo, Japan).

4.2.3.9 Cell transfection

GFP-LC3, mCherry-GFP-LC3 plasmid (Addgene, MA, USA), the siRNA targeting human FOXO3a, human ATG5, human ATG7 or control siRNA and the shRNA targeting human Bax or control shRNA with scrambled sequence were transfected using Lipofectamine 2000™ reagent (Invitrogen, CA, USA) according to the manufacturer's instructions.

4.2.3.10 Luciferase assay

A549 cells were seeded in 6-well plate, cultured for 24 h, and then transfected with 1 μg pGMFOXO-Lu (Genomeditech, Shanghai, China) and 0.05 μg pRL-TK Renilla (Beyotime, Nantong, China) with 10 μL Lipofectamine 2000 and incubated for 24 h at 37℃ with LZ-101. Cells were lysed with Promega passive lysis buffer and assayed by using Promega dual luciferase (Firefly luciferase/Renilla luciferase) kit. Luciferase intensity was detected with a Luminoskan Ascent (Thermo Fisher Scientific Inc. Finland).

4.2.4 *In-vivo* Study

4.2.4.1 Antitumor effects in nude mice

Male BALB/c nude mice, 35–40 days old and with weight ranging from 18-22 g, were supplied by Shanghai Laboratory Animal Limited Company. The mice were

maintained in a pathogen-free environment (23 ± 2 ℃ and 55 ± 5% humidity) on a 12 h light-12 h dark cycle with food and water supplied ad libitum throughout the experimental period. Mice were subcutaneously inoculated with 1×10^6 A549 cells/ nude mice. After 12-14 days, tumor sizes were determined using micrometer calipers, then nude mice with similar tumor volume (eliminate mice with tumors that are too large or too small) were randomly divided into four groups (6 /group): one saline tumor control group; (i.v.) 5-fluorouracil 30 mg/ml/2 days group; (i.v.) LZ-101 10 mg/kg/2 days group; (i.v.) LZ-101 20 mg/ml/2 days group. At the end of 3 weeks, the mice were sacrificed, and the tumor xenografts were removed and measured. Tumor volume (TV) was calculated using the following formula: TV (mm^3) = $d^2 \times D/2$, where d and D are the shortest and the longest diameters, respectively. This study was approved in SPF Animal Laboratory of China Pharmaceutical University.

4.2.4.2 TUNEL assay

Apoptosis induction in the tissue specimen was analyzed by TUNEL assay. It was performed as per instructions given in situ cell death kit. The slides were photographed with a confocal laser scanning microscope (Fluoview FV1000, Olympus, Tokyo, Japan).

4.2.4.3 Immunohistochemistry

The expression of FOXO3a, Bim, Bcl-2, Bax of the tissues of control and LZ-101 (20 mg/kg) treated groups was assessed by SP immunohistochemical method using a rabbit-anti-human monoclonal antibody and an Ultra-Sensitive SP kit (kit 9710 MAIXIN, Fuzhou, Fujian). Tissue sections (4 mm thick) were placed onto treated slides

(Vectabond, Vector Laboratories, Burlingame, CA). Sections were heat fixed, deparaffinized and rehydrated through graded alcohols (100%, 95%, 85%, 75%) to distilled water. Tissue sections were boiled in citrate buffer at high temperature for antigen retrieval, and treated with 3% hydrogen peroxide to block endogenous peroxidase activity. The slides were incubated with a protein-blocking agent (kit 9710 MAIXIN, Fuzhou, Fujian) prior to the application of the primary antibody, and then incubated with the primary antibody at 4℃ overnight. The tissues were then incubated with the secondary biotinylated anti-species antibody and labeled using a modification of the avidin-biotin complex immunoperoxidase staining procedure according to the UltraSensitive SP kit manual. Counterstaining was done with Harris hematoxylin. All reagents were supplied by MaixinBio Co. (Fuzhou, China).

4.3 Results & Discussion

4.3.1 LZ-101 inhibited cell viability in human non-small-cell lung cancer cells

To evaluate the inhibitory effect of LZ-101 on human non-small-cell lung cancer cells including A549, H1299 and H460 cells, we investigated its effect on cell viability at different concentrations with varying lengths (12, 24 or 48 h) of treatment. The IC_{50} (the concentration of drug inhibiting 50% of cells) values for A549 cells were 13.95 ± 2.24, 8.61 ± 0.75 and 4.28 ± 0.42 μM, respectively, after 12, 24 and 48 h treatment. Whereas, the IC_{50} values for H1299 were 44.47 ± 6.54, 18.47 ± 0.86 and 6.75 ± 0.58 μM, respectively, after 12, 24 and 48 h treatment. In H460 cells, the IC_{50} values were 22.49 ± 4.52, 13.15 ± 1.02 and 6.80 ± 0.72 μM, respectively, after 12, 24 and 48 h

treatment (Figure 4.5). As shown in Figure 4.6, treatment with 5, 10 and 15 μM LZ-101 for 24 h significantly inhibited the surviving of A549, H1299 and H460 cells with A549 cells being the most sensitive to LZ101. Therefore, A549 cell line was chosen for further experiments with 5, 10 and 15 μM of LZ-101 treatment for 24 h.
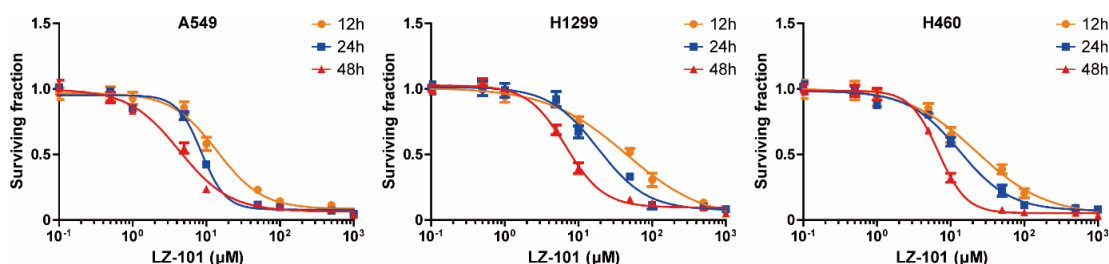
Figure 4.5 MTT assay was used to detect cell viability after treatment of different concentrations of LZ-101 for 12 h, 24 h and 48 h in A549, H1299 and H460.
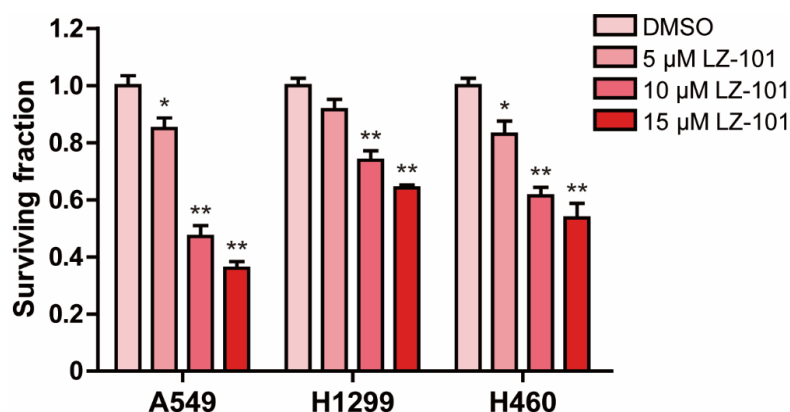
Figure 4.6 Cell viability was detected after treatment of 5, 10 and 15 μM LZ-101 for 24 h in A549, H1299 and H460 cells.

To explore the mechanism of LZ-101 inhibiting A549, H1299 and H460 cells survival, cells were also treated with a pan-caspase inhibitor, Q-VD-OPh, during LZ-101 treatment. Survival inhibition of LZ-101 was significantly inhibited in A549, H1299 and H460 cells, when caspase activity was inhibited by Q-VD-OPh (Figure 4.7).

This suggests that LZ-101 inhibited the survival of human non-small cell lung cancer cells by triggering apoptosis.
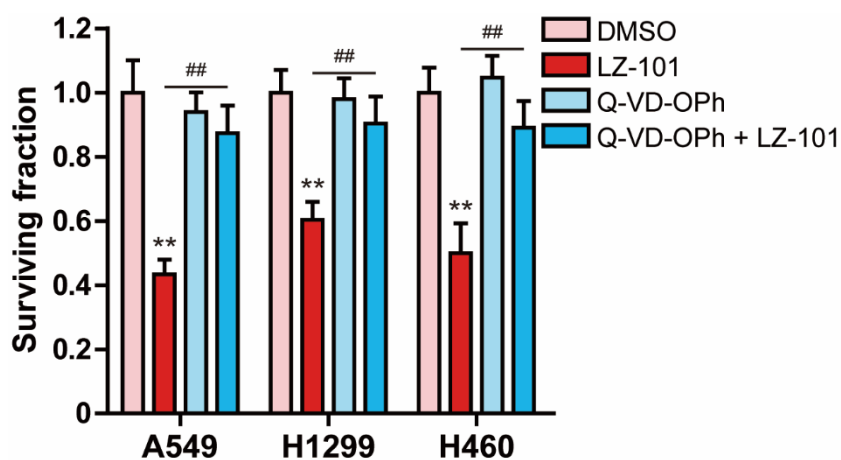
Figure 4.7 Cell viability was detected after treatment of 20 μM Q-VD-OPh or 15 μM LZ-101 for 24 h in A549, H1299 and H460 cells.

4.3.2 LZ-101 induced mitochondrial apoptosis in A549 cells

To detect the apoptosis induced by LZ-101 in A549 cells, DAPI staining assay and Annexin V/PI staining were used with rotenone as positive control. In DAPI staining assay, control cells emitted blue fluorescence with consistent nucleus intensity and showed typical homogeneous distribution of chromatin in nucleus. After LZ-101 treatment, cells presented morphological features of bright apoptotic bodies and nuclear condensation (Figure 4.8 arrows). These features appeared more frequently with increasing concentrations of LZ-101.
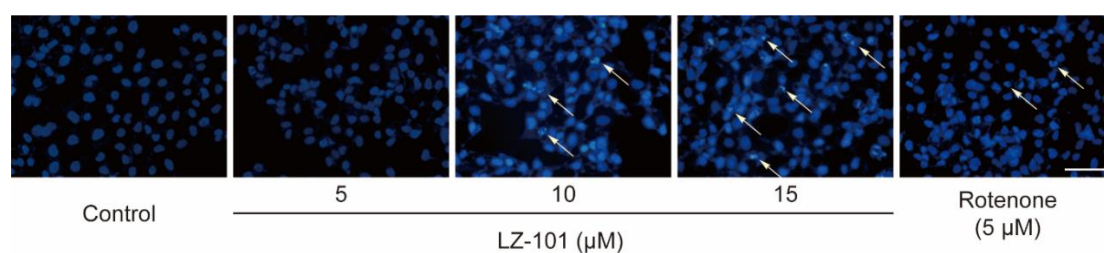
Figure 4.8 DAPI staining was used to detect the apoptosis. Scale bars, 50 μm.

To further confirm the apoptosis induced by LZ-101, Annexin V/PI staining assay was used. As shown in Figure 4.9, increased apoptotic was detected after LZ-101 or rotenone treatment for 24 h. The percentage of apoptotic cells increased from 6.07% ± 1.62% to 14.92% ± 4.32%, 22.07% ± 4.32%, and 43.62% ± 7.83%, respectively. Furthermore, the apoptosis related proteins such as Bcl-2, Bax, caspase-9 and PARP were investigated by Western blots. After treatment with LZ-101 for 24 h, the apoptotic protein Bax expression increased while the anti-apoptotic protein Bcl-2 expression decreased in a concentration-dependent manner (Figure 4.10). The ratio of Bax/Bcl-2 is crucial for the activation of the mitochondrial apoptotic pathway. The ratio of Bax/Bcl-2 was increased by different concentrations of LZ-101 treatment. Besides, Caspase-9 and PARP cleavage were activated significantly after LZ-101 treatment (Figure 4.10). These data indicated that LZ-101 induced apoptosis in A549 cells.
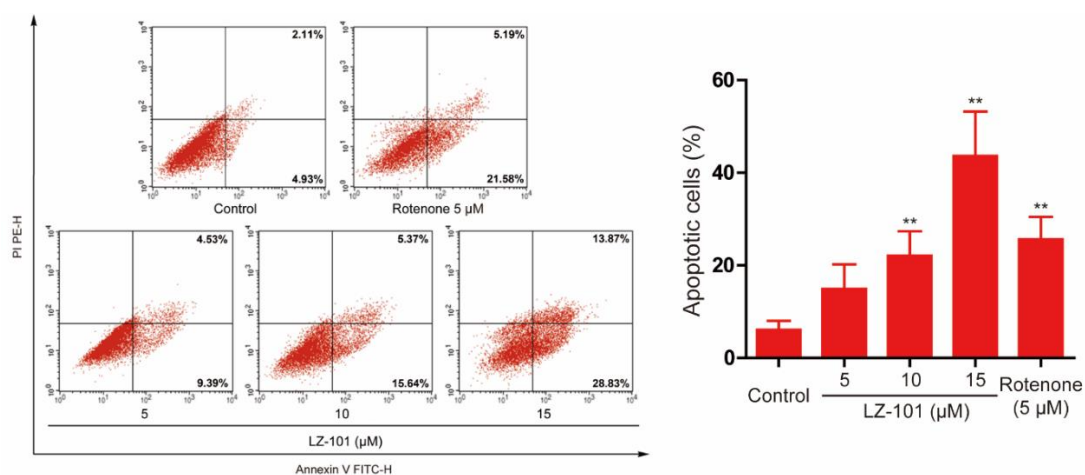
Figure 4.9 Induction of apoptosis were measured by Annexin-V/PI double-staining assay.
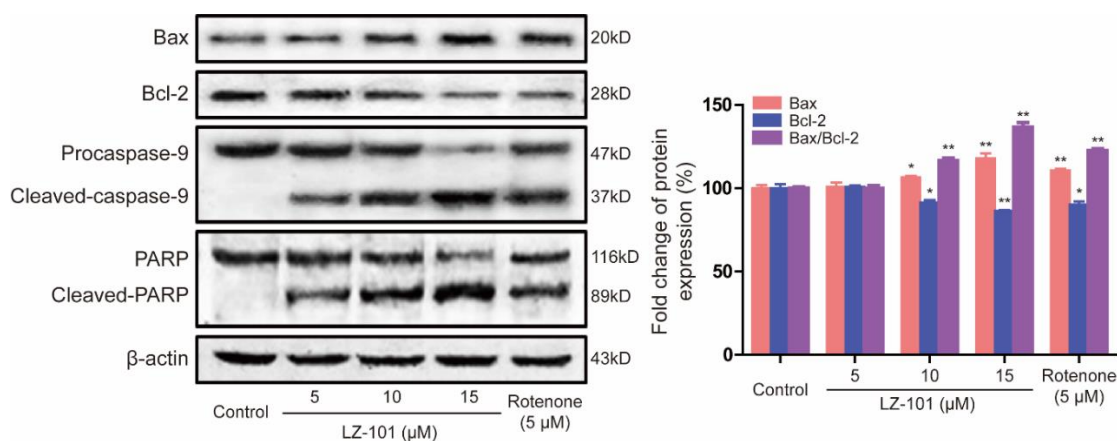
Figure 4.10 The levels of Bax, Bcl-2, caspase-9 and PARP were assessed by Western blot. Ratio of Bax/Bcl-2 expression using densitometric analysis.

In order to elucidate the mechanism of LZ-101-induced apoptosis in A549 cells, we investigated the effect of LZ-101 on mitochondrial function. Changes in mitochondrial functions are essential for mitochondrial apoptotic pathway. In early apoptosis stage, the change of mitochondrial membrane potential ($\Delta\Psi_m$) is a marker for mitochondrial dysfunction. Accordingly, we used a fluorogenic probe JC-1 staining cells to detect the change of $\Delta\Psi_m$ after LZ-101 treatment. Flow cytometric analysis revealed that A549 cells became more susceptible to mitochondrial membrane depolarization after LZ-101 treatment (Figure 4.11). We observed almost 50% decrease in $\Delta\Psi_m$ with 15 μM LZ-101, compared with the control group. Multidomain proapoptotic proteins like Bax and Bak play pivotal roles in the release of apoptogenic proteins, such as cytochrome c and AIF, from the mitochondria into the cytosol in response to apoptotic stimuli [84]. To study the involvement of Bax in LZ-101-induced apoptosis, we used Bax shRNA to diminish the expression of Bax. As shown in Figure 4.12, cytochrome c and AIF were released from mitochondria upon LZ-101 treatment whereas their release was almost completely blocked in Bax knockdown cells and β-actin levels of all the fractions were similar.

72

Taken together, our findings suggested that LZ-101 induced apoptosis was mediated by mitochondrial dysfunction in A549 cells.
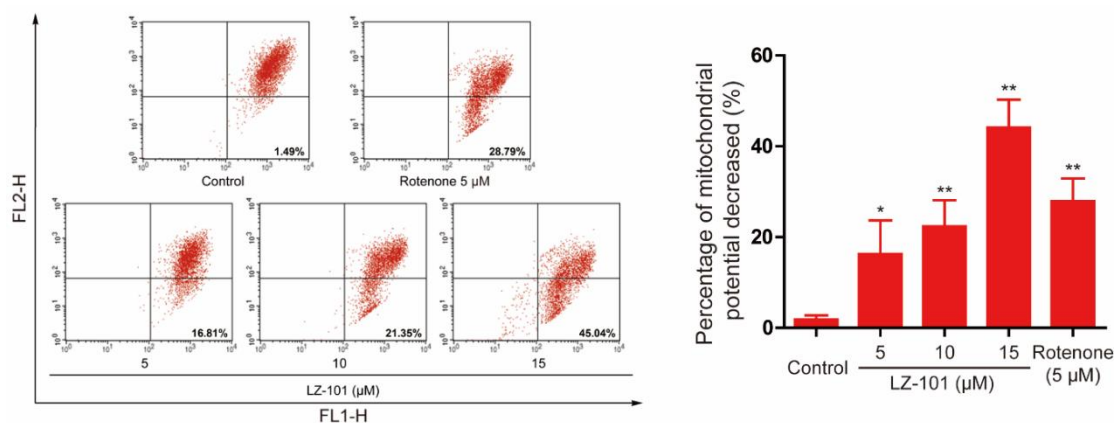
Figure 4.11 The change of $\Delta\Psi_m$ as detected by flow cytometry using JC-1 staining.
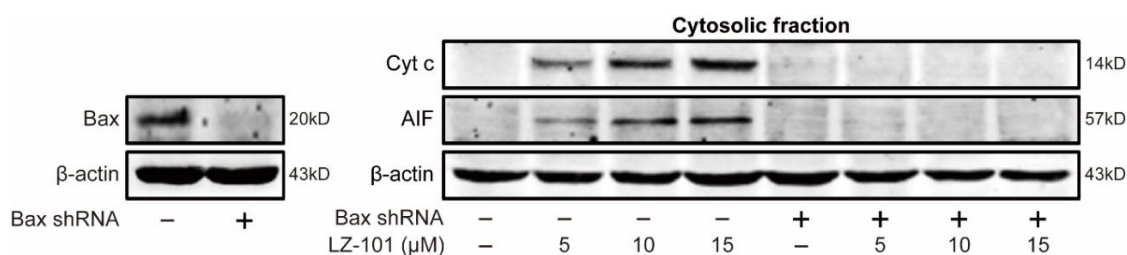
Figure 4.12 The release of Cyt c and AIF from mitochondria into cytoplasm was measured by Western blot assay after knockdown of Bax.

4.3.3 The up-regulation of FOXO3a expression was involved in LZ-101 induced apoptosis of mitochondrial

When cells receive intrinsic apoptosis signals, the pro-apoptotic BH3-only proteins, such as Bim, Bad, Noxa and Puma, will be activated. These proteins not only inhibit the activity of anti-apoptotic protein (Bcl-2, Bcl-xL and Mcl-1), but also activate the pro-apoptotic protein (Bax and Bak), which form an oligomer and subsequently punch pores in the outer mitochondrial membrane, eventually, leading to permeabilization of mitochondrial outer membrane [67]. As mentioned before, although pro-apoptotic BH3-only protein Bim plays a crucial role in apoptosis, it could be regulated by

FOXO3a at transcriptional level. Therefore, we investigated the effect of LZ-101 on this signalling pathway. Western blots analysis showed that Bim increased in A549 cells after LZ-101 treatment for 24 h (Figure 4.13). This result confirms that FOXO3a regulated the transcription of Bim. Moreover, we found that LZ-101 up-regulated FOXO3a protein expression in A549 cells (Figure 4.13). The change of mRNA level of Bim, tested by Real-time PCR, was consistent with that of the protein levels (Figure 4.14). Furthermore, Luciferase reporter gene assay suggested that LZ-101 increased transcriptional activity of FOXO3a in a concentration-dependent manner (Figure 4.15). LZ-101 also promoted FOXO3a to translocate into the nucleus (Figure 4.16). Therefore, LZ-101 up-regulates the expression of FOXO3a and promotes the transcription of Bim.
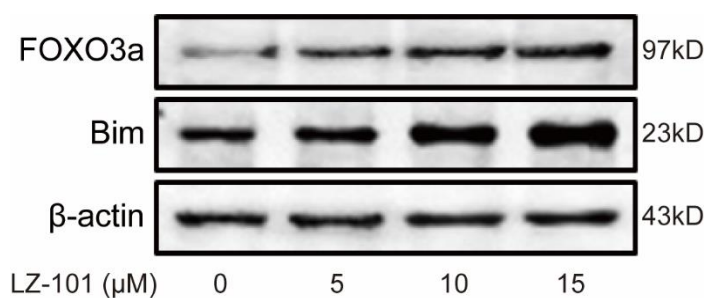
Figure 4.13 The levels of FOXO3a and Bim were assessed by Western blot after 5, 10 and 15 μM LZ-101 treatment for 24 h.
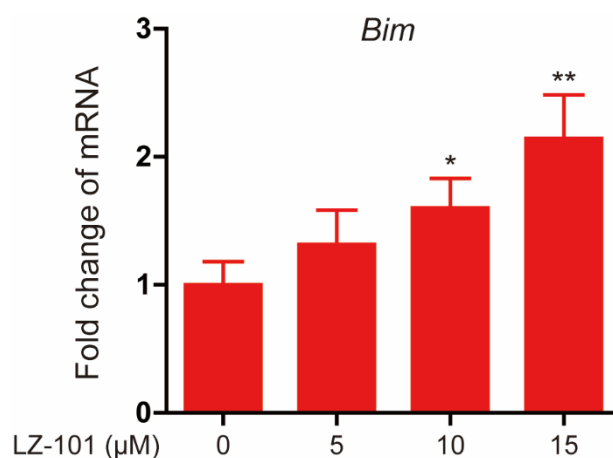
Figure 4.14 Bim mRNA was measured by real-time PCR following treatment with 5, 10 and 15 μM LZ-101 for 24 h in A549 cells.
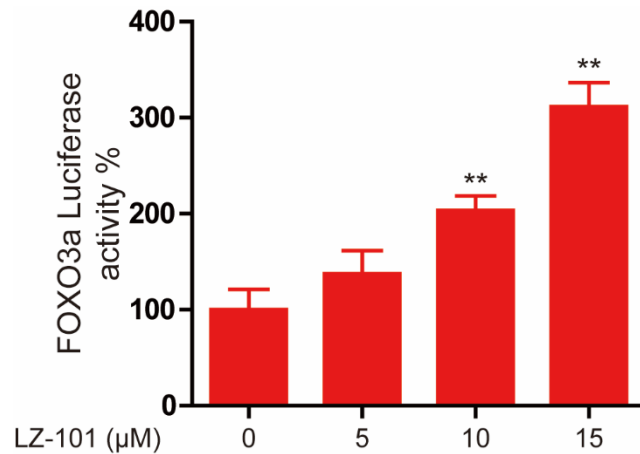
Figure 4.15 The transcriptional activities of FOXO3a in A549 cells co-transfected with pGMFOXO-Lu and pRL-TK Renilla with LZ-101.
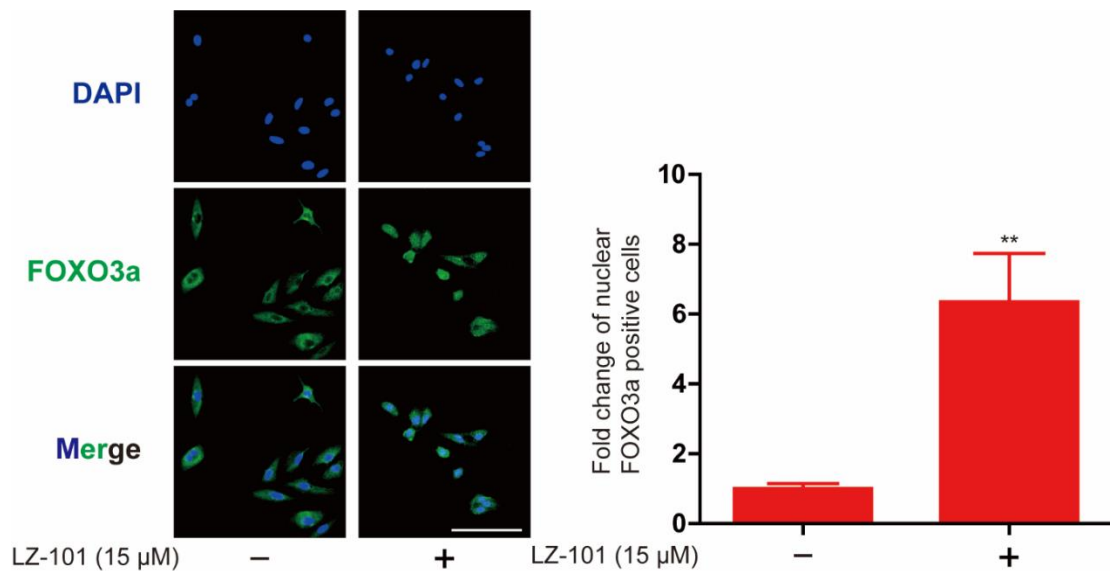
Figure 4.16 Immunofluorescence staining of FOXO3a in A549 cells was carried out to test the effect of LZ-101 on FOXO3a protein nuclear translocation.

To further explore the mechanism of LZ-101-induced apoptosis and determine the roles of FOXO3a activation in this process, we detected the influence of LZ-101 on Bax and Bcl-2 expression after FOXO3a siRNA transfection. Western blot results showed that the protein level of Bax and Bcl-2 were notably regulated by LZ-101. However, these effects of LZ-101 were obviously reversed by the knockdown of FOXO3a (Figure 4.17). Remarkably, the ratio of Bax/Bcl-2 increased by LZ-101 was also reversed. Moreover, Flow cytometry analysis demonstrated that the percentage of

apoptotic cells in LZ-101 group transfected with FOXO3a siRNA reduced from 50.47%

± 8.59% to 19.44% ± 3.63%, compared with LZ-101 group without transfection with

FOXO3a siRNA (Figure 4.18). The decrease of mitochondrial potential was inhibited

in LZ-101 group transfected with FOXO3a siRNA compared with LZ-101 group

(Figure 4.19). In conclusion, the up-regulation of FOXO3a expression was involved in

the induction of mitochondrial apoptosis by LZ-101.
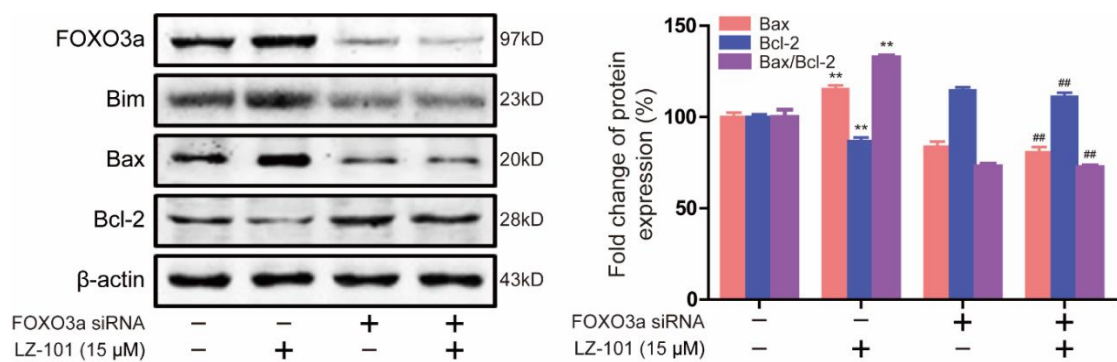
Figure 4.17 FOXO3a, Bim, Bax and Bcl-2 were detected by Western blot.
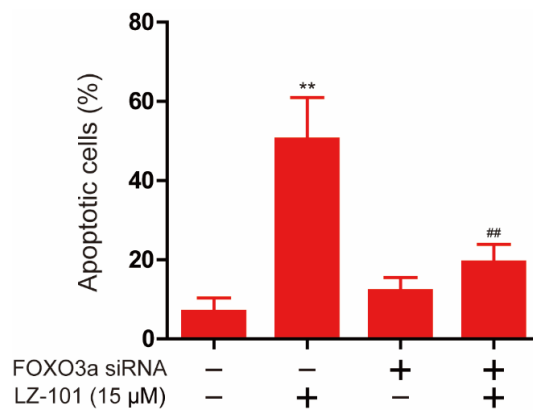
Figure 4.18 Annexin-V/PI staining assay were measured after knockdown of FOXO3a.
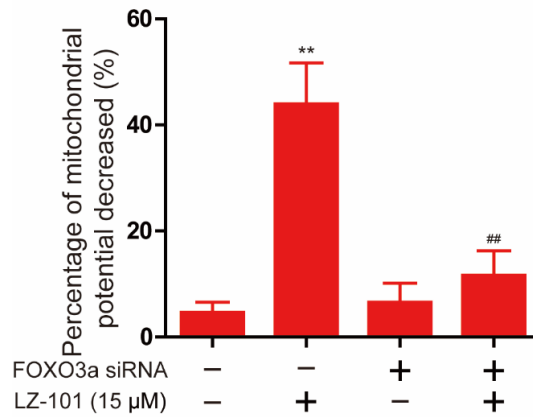
Figure 4.19 The change of $\Delta\Psi_m$ were measured by flow cytometry after knockdown of FOXO3a.

4.3.4 LZ-101 increased the stability of FOXO3a in a proteasome-independent manner

To further investigate the molecular mechanism by which LZ-101 up-regulates FOXO3a expression, de novo protein synthesis inhibitor cycloheximide (CHX) and proteasome inhibitor MG132 were used, respectively. After treatment of CHX, FOXO3a was more stable in A549 cells treated by LZ-101 compared with A549 cells treated by DMSO (Figure 4.20), indicating that LZ-101 interfered with FOXO3a degradation. In support of this observation, when MG132 (20 μM) was added to A549 cells, increased FOXO3a levels were observed, whereas LZ-101 unexpectedly further increased FOXO3a levels in A549 cells treated with MG132 (Figure 4.21). Further detection of apoptosis levels showed that LZ-101 significantly increased apoptosis induced by MG132 (Figure 4.22). These results suggested that LZ-101 interfered with FOXO3a degradation in a proteasome-independent manner.
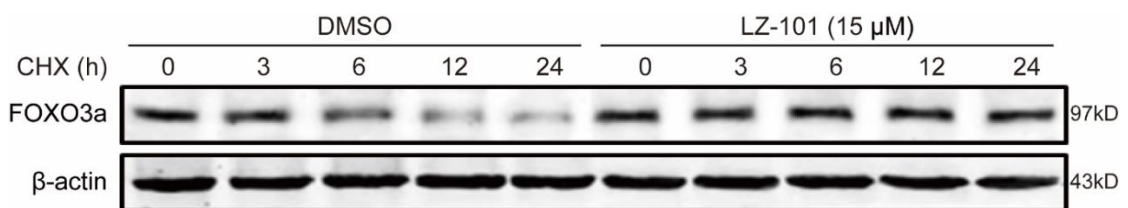
Figure 4.20 Degradation dynamics of FOXO3a following a time course CHX treatment in A549 cells treated with 15 μM LZ-101.
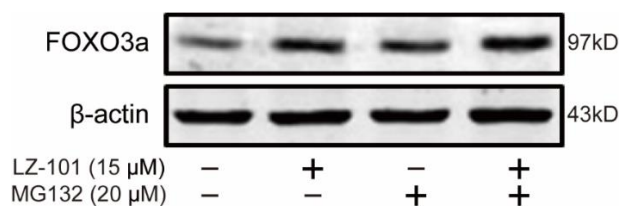
Figure 4.21 FOXO3a proteins were stabilized in the presence of MG132 (20 μM) in A549 cells treated with 15 μM LZ-101.
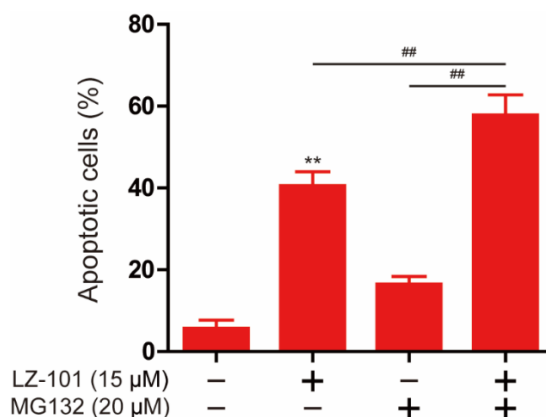
Figure 4.22 Annexin-V/PI staining assay measured by flow cytometry in the presence of MG132 (20 μM) in A549 cells treated with 15 μM LZ-101.

In addition to proteasome degradation of proteins in cells, the autophagic lysosomal pathway may also be involved in protein degradation. To confirm this hypothesis we detected the co-localization of FOXO3a and LAMP1 in A549 cells. As shown in Figure 4.23, LZ-101 indeed inhibited the co-localization of FOXO3a and LAMP1. To further confirm FOXO3a is degraded by the autophagic lysosomal pathway, an autophagolysosome inhibitor, bafilomycin A1, was used. After treatment with bafilomycin A1, FOXO3a degradation was inhibited, combination of bafilomycin A1 with LZ-101 could not further inhibit FOXO3a degradation (Figure 4.24). These results suggested that LZ-101 increased the stability of FOXO3a through the autophagic lysosome pathway rather than the ubiquitin proteasome pathway.
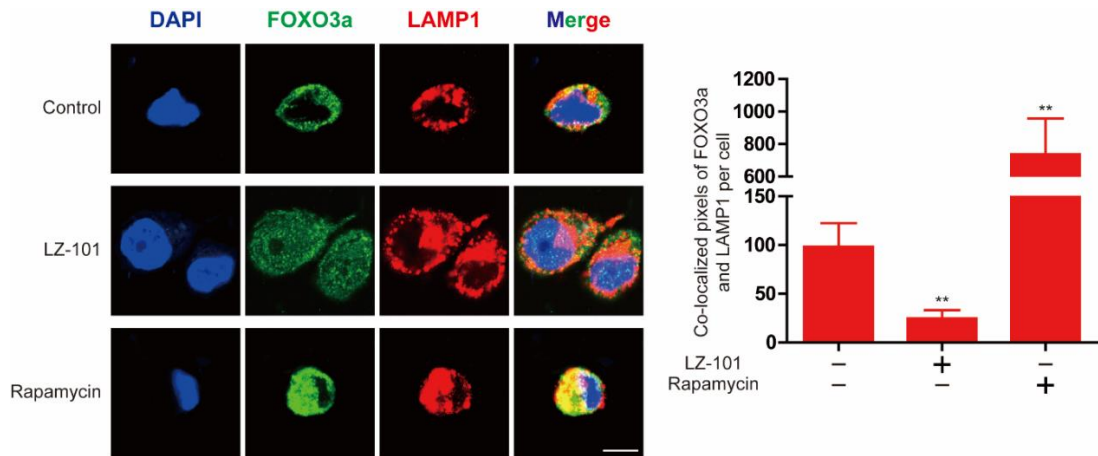
Figure 4.23 Confocal microscopy of A549 cells treated with 15 μM LZ-101 or 100 nM rapamycin, immunostained for FOXO3a (green) and LAMP-1 (red).
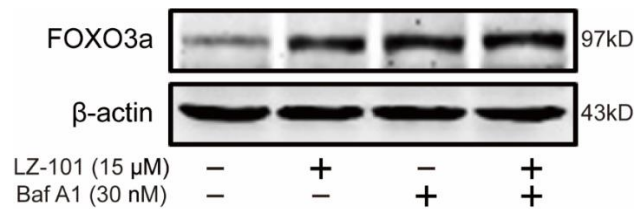
Figure 4.24 FOXO3a was detected after 15 μM LZ-101 and 30 nM bafilomycin A1 treatment.

4.3.5 LZ-101 blocked autophagy flux in A549 cells

In Figures 4.23, 100 nM rapamycin remarkably increased the co-localization of FOXO3a and LAMP1 in A549 cellls. This is consistent with the study that FOXO3a is an autophagy substrate [86]. To further investigate the molecular mechanism by which LZ-101 increased the stability of FOXO3a, we investigated the effect of LZ-101 on autophagy. LC3-I and LC3-II are both produced post-translationally, but LC3-I is cytosolic and LC3-II, the hallmarks of autophagy, is membrane bound and forms the autophagosome [87]. Treatment with 15 μM LZ-101 increased GFP-LC3 puncta accumulation (Figure 4.25). Then, we assessed LC3 in the cell lysates by immunoblot analysis. We found that LC-II protein levels gradually increased following treatment

with LZ-101 in A549 cells (Figure 4.26), indicateing that LZ-101 increased autophagosome formation in A549 cells.
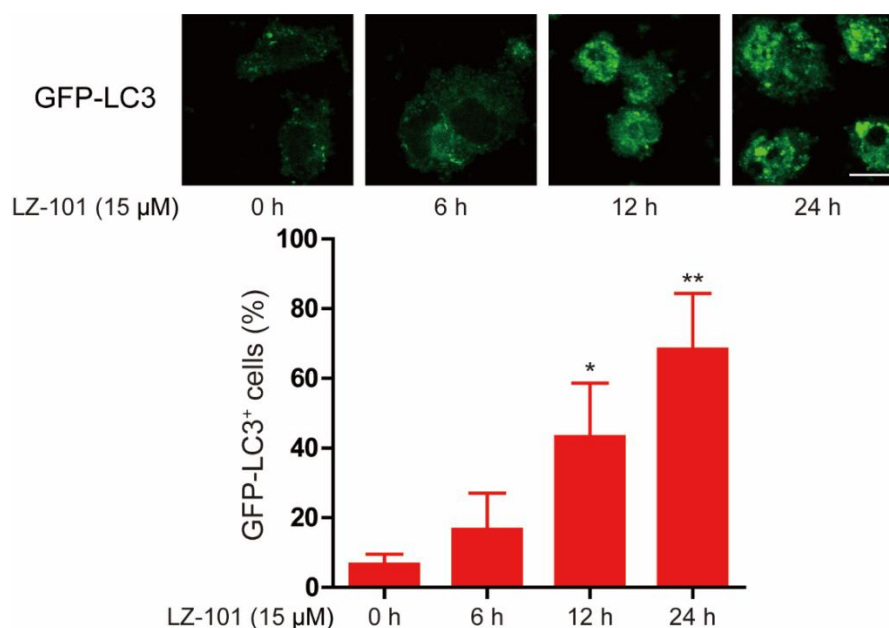
Figure 4.25 Induction of GFP$^+$ dots in A549 cells expressing GFP-LC3 treated with 15 µM LZ-101. Images of individual cells and quantified of GFP-LC3$^+$ cells. Scale bars, 10 µm
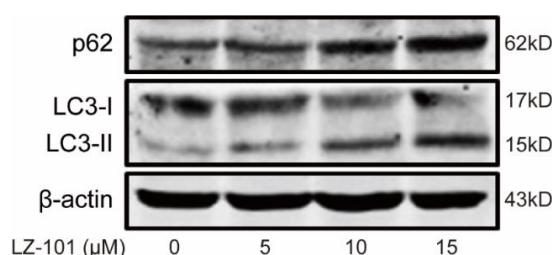
Figure 4.26 p62 and LC3 were detected by Western blot in A549 cells treated with 15 µM LZ-101.

Since enhanced autophagosome accumulation could be caused either by promoted autophagosome formation or by suppressed autophagosome degradation, we determined whether a complete autophagic flux occurred after LZ-101 treatment. As shown in Figure 4.26, the degradation of p62 was significantly suppressed in A549 cells with LZ-101 treatment. To further assess the status of autophagic flux, we used the mCherry-GFP-LC3 construct. As the more stable of mCherry in acidic conditions

compared with GFP, autophagic flux can be determined by the appearance of more GFP$^-$ mCherry$^+$ (red) puncta. After treatment with LZ-101, large-sized GFP$^+$ mCherry$^+$ (yellow) puncta were observed, while the yellow puncta did not change significantly after bafilomycin A1 treatment (Figure 4.27). These results indicated that LZ-101 blocked autophagy flux in A549 cells by inhibiting autophagosome degradation.
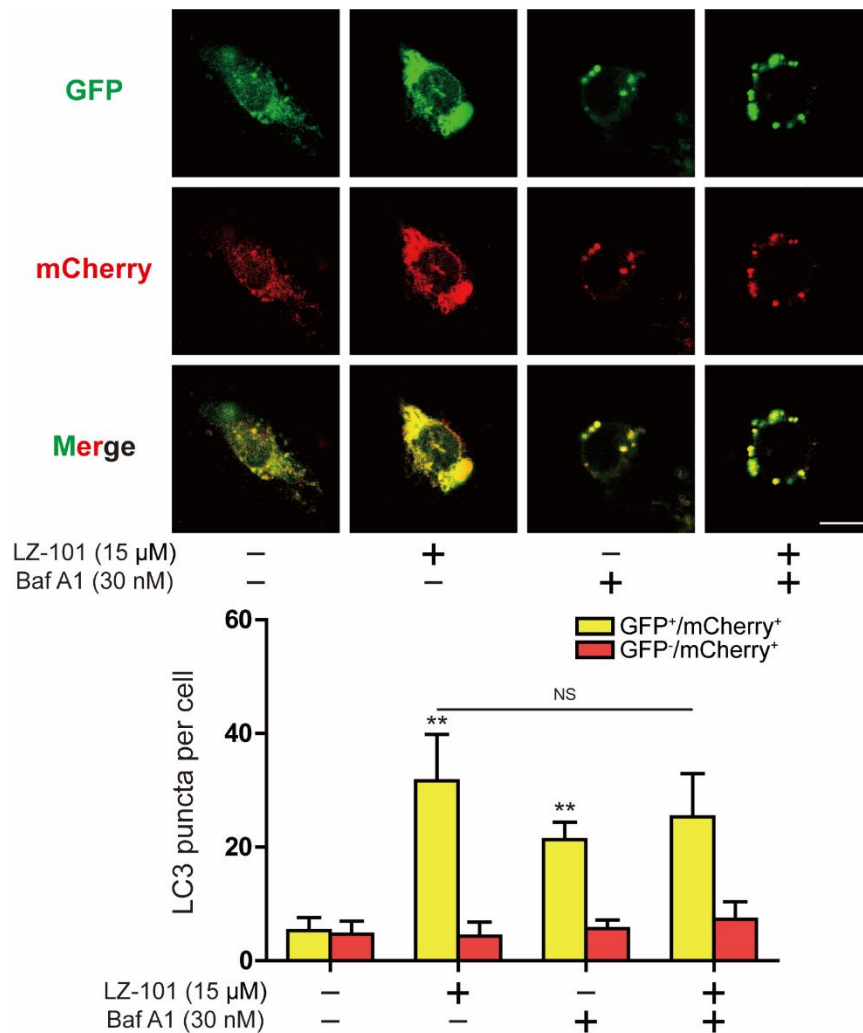
Figure 4.27 A549 cells expressing mCherry-GFP-LC3 were observed under a confocal microscopy after 15 μM LZ-101 and 30 nM bafilomycin A1 treatment.

4.3.6 Inhibition of autophagosome formation abolished the induction of apoptosis by LZ-101

To investigate the role of autophagy in the induction of apoptosis by LZ-101, we

blocked the formation of autophagosomes with 3-MA. After treatment with 3-MA, the effect of LZ-101 to stabilize FOXO3a abolished (Figure 4.28). In addition, the effect of LZ-101 induced apoptosis was similarly abolished after treatment with 3-MA (Figure 4.29). In the process of autophagy, ATG5 and ATG7 are required for the formation of the autophagosome (need references here to support this statement). As shown in Figure 4.30, we silenced the expression of ATG5 or ATG7 through transfecting siRNA. The induction of apoptosis was abolished after diminishing the expression of ATG5 or ATG7 in LZ-101-treated A549 cells. Thus, blocking the formation of autophagosome abolished LZ-101 induced apoptosis of A549 cells.
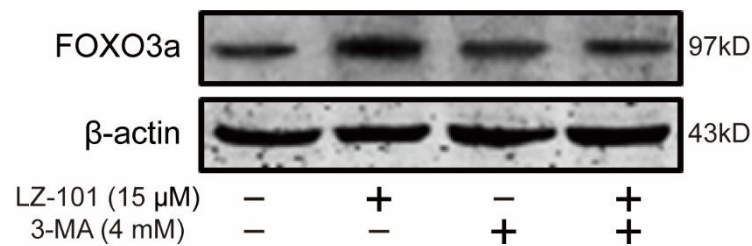
Figure 4.28 FOXO3a was detected by Western blot in the presence of 3-MA (4 mM) in A549 cells treated 15 μM LZ-101.
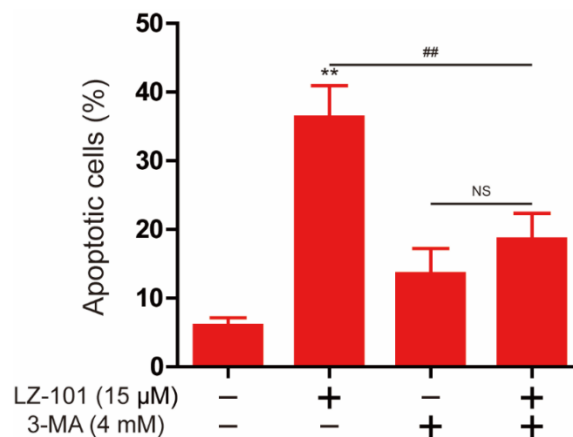
Figure 4.29 Annexin-V/PI staining assay by flow cytometry in the presence of 3-MA (4 mM) in A549 cells treated with 15 μM LZ-101.
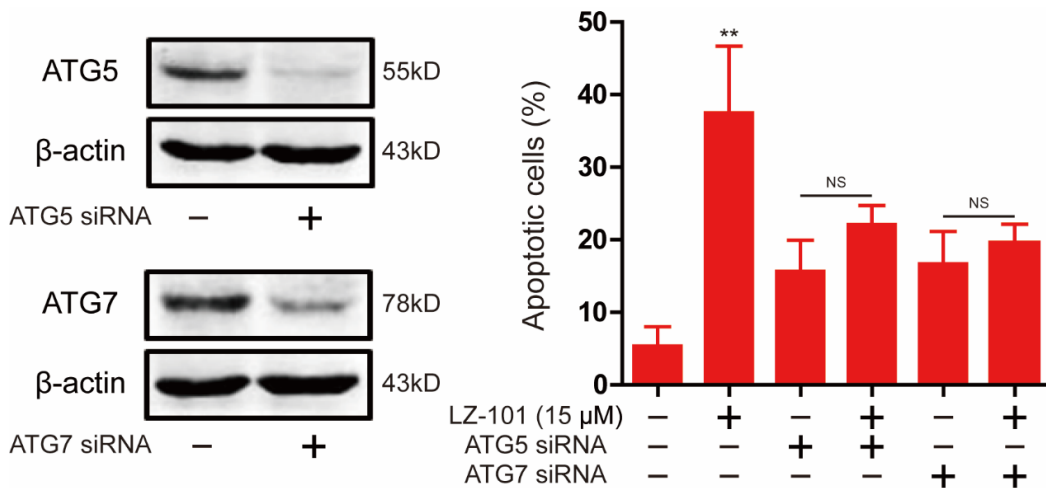
Figure 4.30 Annexin-V/PI staining assay by flow cytometry in A549 cells treated with 15 μM LZ-101 and transfected ATG5 or ATG7 siRNA.

4.3.7 LZ-101 exerted antitumor effect with low toxicity in A549 inoculated xenograft mice

The xenograft mice transplanted with A549 cells were used to evaluate the antitumor effect of LZ-101 in vivo. The tumor volume of mice with LZ-101 treatment was smaller than that of mice in control group but larger than that of mice in 5-fluorouracil-treated group at the same measurement day (Figure 4.31). Moreover, the tumor weight of LZ-101-treated mice was significantly smaller than that of the control group (Figure 4.32). Accordingly, the inhibitory rates of 5-fluorouracil, 10 mg/kg and 20 mg/kg LZ-101 groups were 68.05%, 40.86% and 55.62%, respectively (Table 4.1). The TUNEL assay was performed to detect apoptotic cells in tumor tissues. The results indicated that DNA damage in tumor tissues was induced by LZ-101. In addition, immunohistochemical analysis showed that p-Akt and Bcl-2 expression were decreased while FOXO3a, Bim and Bax expression were increased after LZ-101 treatment (Figure 4.33).
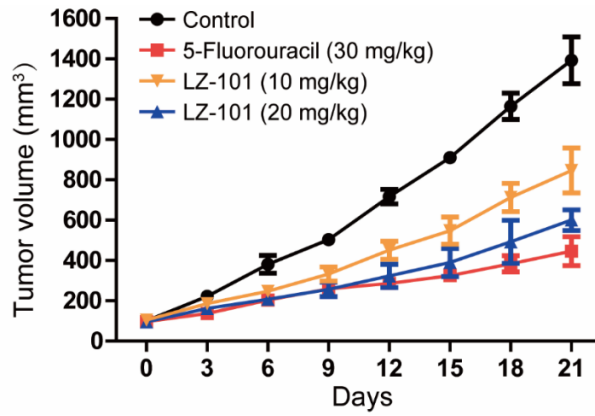
Figure 4.31 Tumor volumes of control, 5-fluorouracil, LZ-101 treatment groups were measured and calculated every 3 days.
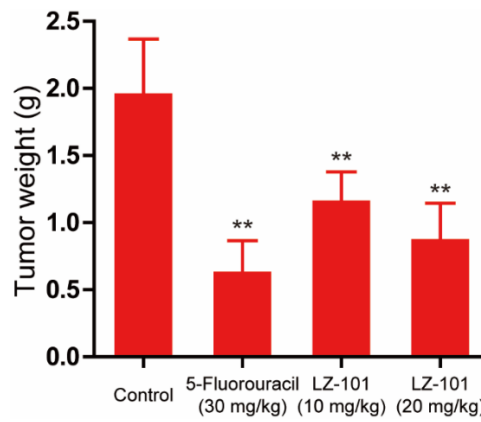
Figure 4.32 Weight of tumor in control, 5-fluorouracil, LZ-101 treatment groups.

Table 4.1 Inhibitory activity of LZ-101 against A549 xenograft tumor.

Groups	Dose (mg/kg)	Inhibitory rate (%)
5-Fluorouracil	30	68.05[**]
LZ-101	10	40.86[**]
	20	55.62[**]

[**]$P < 0.01$ versus control group.
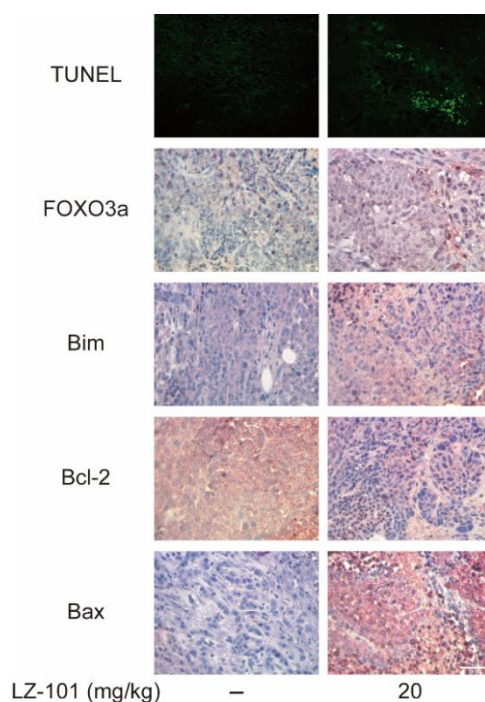
Figure 4.33 DNA damage and FOXO3a, Bim Bcl-2, Bax expression detected by TUNEL assay and immunohistochemistry in tumor xenograft tissues.

Furthermore, we monitored the toxicity of LZ-101 during the entire in vivo experiment. LZ-101 treatment (21 days) did not cause any physical abnormalities. Hematological parameters showed that there were no notable changes in the analysed parameters in the experimental animals, as listed in Table 4.2 with the standard ranges for mice. Besides, there was no significant difference in the average body weight of LZ-101-treated mice compared with that of the control mice (Figure 4.34). H&E staining (Figure 4.35) showed no morphological changes in the organs of mice with LZ-101 treatment. Taken together, our results suggested that LZ-101 inhibited tumor growth via FOXO3a activation in xenograft mice bearing A549 tumor with low toxicity *in vivo*.

Table 4.2 Hematology profile in non-tumor bearing athymic nude mice administered with normal saline. Two mice per group were used. Standard ranges were obtained in house from 100 normal BALB/c mice of 8-12 weeks age.

Hematological parameters	Control	10 mg/kg	20 mg/kg	Standard
White blood cells (×10^3 μl)	4.71/4.42	4.90/4.95	5.87/5.74	4.5-9.1
Red blood cells (× 10^6/μl)	9.76/10.70	10.51/9.84	10.25/9.30	7.51-16.1
Hemoglobin (g/dL)	14.5/13.0	15.2/14.2	14.9/13.9	12.8-16.1
Hematocrit (%)	44.8/41.8	47.9/45.3	46.9/44.7	34-50
Lymphocytes (%)	67.2/78.8	50.4/61.4	55.4/63.1	49-82
Monocytes (%)	2.64/4.24	4.54/5.24	3.14/4.64	2-8
Eosinophils (%)	0.24/0.34	0.04/0.74	0.54/0.64	0-3
Basophils (%)	0.24/0.74	0.34/0.34	0.54/0.24	0-3
Platelet (×10^3 μl)	507/410	560/483	526/744	115-1037
Mean corpuscular volume (fL)	45.9/45.8	45.6/46.0	45.8/48.1	41-60
Mean corpuscular hemoglobin (pg)	14.9/14.3	14.5/14.4	14.5/14.9	13-19
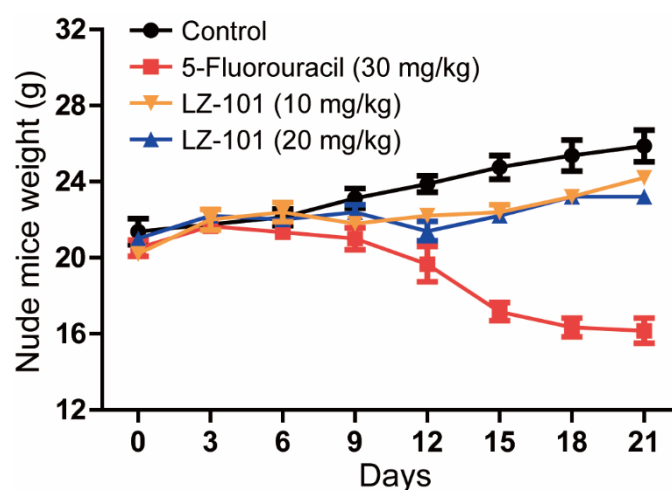
Figure 4.34 Nude mice weight was recorded every three days.
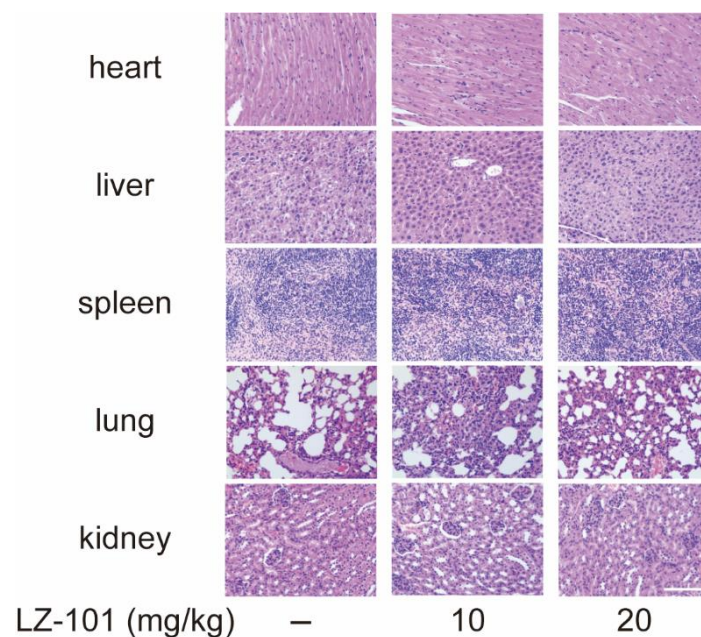
Figure 4.35 H&E stained main organs of mice from treated and control sets to evaluate the toxicity of LZ-101.

4.4 Conclusion

In summary, LZ-101 displayed strong antitumor activity both *in vitro* and *in vivo* based on the mitochondrial apoptosis induced by up-regulation of Bim through stabilizing FOXO3a in autophagic lysosomal dependent manner (Figure 4.36). Moreover, how FOXO3a escapes from autophagosomes to induce transcription remains unknown. Studies have shown that inhibition of autophagy in different means promoted the transcription of FOXO3a. It was suggested that inhibition of autophagy induced FOXO3a activation was not a specific function of LZ-101. Therefore, the relationship between autophagy and FOXO3a activation needs further study and is underway in our laboratories. In conclusion, this study indicated that LZ-101 could be a potential effective agent with low toxicity for human non-small-cell lung carcinoma.
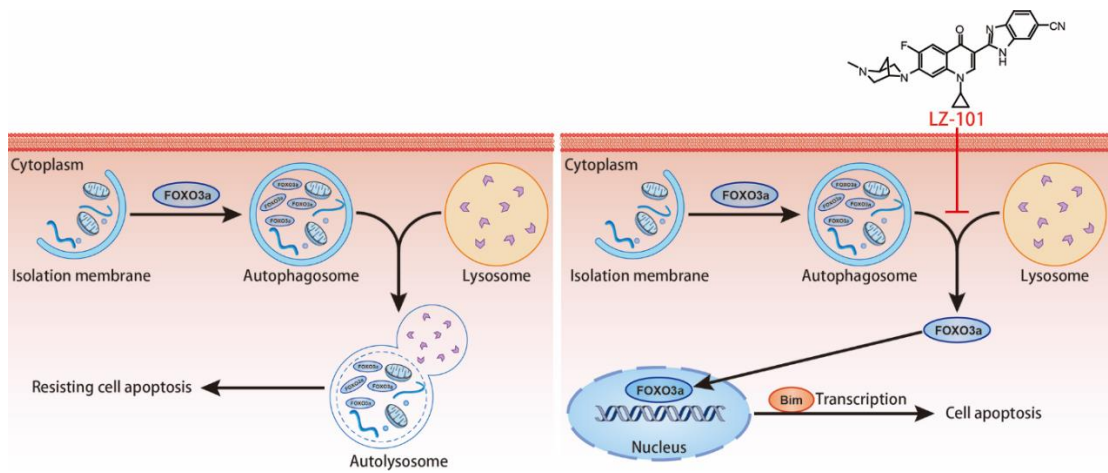
Figure 4.36 The possible mechanism of LZ-101 induced apoptosis in NSCLC.

CHAPTER V.

PERTURBING THE UNIQUE ENERGY METABOLISM IN CANCER CELLS, A REVISIT OF THE WARBURG EFFECTS

5.1 Background

5.1.1 Development of breast cancer treatment

Breast cancer is the most common cancer in women worldwide (second most common cancer overall). In 2017, the number of new cases and deaths from breast cancer reached 252,710 and 40,610, respectively [88]. In China, breast cancer is the most common cancer among female, with the incidence 17.07% and 278,800 new cases, ranking fifth in the causes of tumor death after cancers of lung, gastric, liver and colorectum [89]. Depending on the type and degree of advancement, breast cancer is treated with surgery and then possibly chemotherapy and/or radiation therapy. Among all the breast cancer cases, 15% are triple-negative breast cancers (TNBCs), which lack expression of estrogen receptor (ER), progesterone receptor (PR), and human epidermal growth factor receptor 2 (HER2) and have a very aggressive disease course [90]. 10% to 20% of women who have TNBC subtype breast cancers usually have shorter survival due to high malignancy, high recurrence rate and high transferability [91]. Compared with the well-defined behavior of breast cancer, the molecular mechanism of breast cancer initiation and progression remains poorly understood. The lack of approved targeted therapies and effective chemotherapy with low toxicity for TNBC remains a major hindrance for treatment and prompted us to identify novel targets.
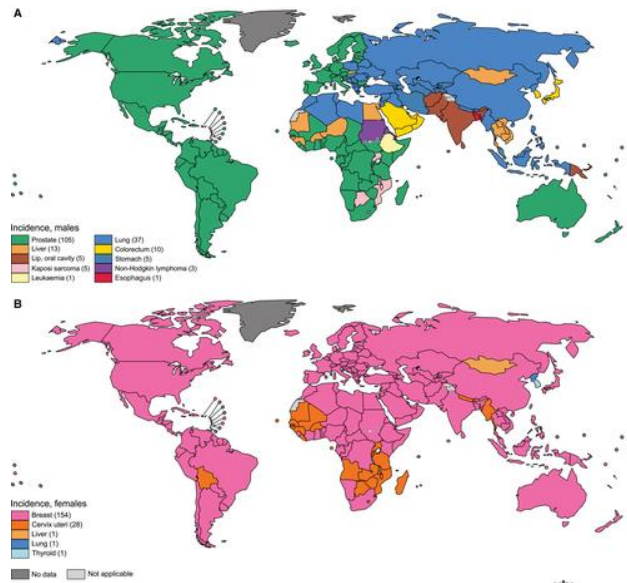
Fiugre 5.1 Global Maps Presenting the Most Common Type of Cancer Incidence in 2018 in Each Country Among (A) Men and (B) Women[92].

5.1.2 Characteristics of glucose metabolism in cancer

Under aerobic conditions, normal cells process glucose, first to pyruvate via glycolysis in the cytosol and thereafter to carbon dioxide in the mitochondria; under anaerobic conditions, glycolysis is favored and relatively little pyruvate is dispatched to the oxygen-consuming mitochondria. However, cancer cells have a unique energy metabolism manner, which was first proposed by Warburg almost a century ago: even in the presence of oxygen, cancer cells can reprogram their glucose metabolism, and thus their energy production, by limiting their energy metabolism largely to glycolysis, leading to a state that has been termed ''aerobic glycolysis'' [93]. The shift in energy production from mitochondrial oxidative phosphorylation (OXPHOS) to aerobic glycolysis is a hallmark of cancer development [94]. Aerobic glycolysis not only supports rapid growth, but also makes the cancer cells less dependent on oxygen availability and generates a suitable micro-environment for cancer progress [95].

90

Studies of the metabolic changes in cancers proide rationale for and insight about cancer therapy. Some rate-limiting enzymes of glycolysis, such as hexokinase (HK) and pyruvate kinase (PK) have, in addition to ensuring glycolytic reactions, other biological functions such as regulation of transcription and induction of apoptosis [96, 97]. Some inhibitors or regulators of glycolytic enzymes have been developed to extract cancer cells' "sweet tooth" [98]. The recent approval of the first tumor metabolism regulating drug, Enasidenib, by FDA served as a new gateway to cancer therapy. Inhibition of glycolysis is attracting increasing attention as a novel therapeutic focus in cancer managements.
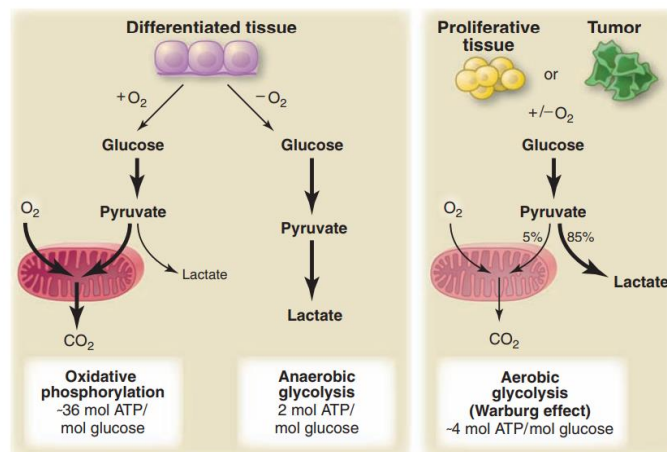
Fiugre 5.2 The unique glucose metabolism in cancer cells [99].

5.1.3 Functions of HK2 in cancer cells

The high glycolytic rate is closely connected with the greatly increased expression of hexokinase II (HK II), and its binding to the mitochondria through the voltage-dependent anionic channel (VDAC) in malignant cells [100]. HK II mediates the first rate-controlling step of glycolysis, phosphorylating glucose to glucose-6-phosphate.

VDAC is a mitochondrial porin located in the outer mitochondrial membrane (OMM) and is responsible for the exchange of metabolites and ions between mitochondria and other cellular compartments [101]. It has been demonstrated that binding of HK II to VDAC inhibits apoptosis as a result of alterations in the permeability of OMM [102]. It was also reported that the increased binding of HK II to VDAC was associated with drug resistance of cancer cells to chemotherapeutic agents [86]. In malignant tumors, the level of HK II expression was 10 fold higher than normal tissues [103]. Stable binding of HK II to mitochondria promotes aerobic glycolysis, but impairs mitochondrial respiration [104]. HKII binds to VDAC through both its N-terminal membrane binding domain and its putative BH4 domain, which is proposed to compete with the binding of VDAC to Bcl-xL (an anti-apoptotic member of the BCL-2 family proteins) [105]. Thus, HKII binding displaces Bcl-xL from VDAC and thereby facilitates its direct interaction with proapoptotic BCL-2 family members, such as Bax and its homolog Bak, and protects against OMM permeabilization. Alternatively, if HK II was detached, it may prevent Bcl-xL from binding to Bax, resulting in the release of cytochrome c and other apoptosis enhancing proteins.

AKT is an oncogene protein kinase that controls various cellular functions and can exert antiapoptotic effects [106]. It was reported that AKT could phosphorylate HKII at threonine 473 directly, resulting in the increased binding of HKII with VDAC and the observed anti-apoptotic effects [107]. In addition to the direct action on HKII, AKT could influence the binding of HKII with VDAC through its downsteam negative

regulating factor GSK-3β. When AKT is inhibited, GSK-3β is dephosphorylated and activated. A large proportion of GSK-3β is found in the cytosol, but pools are also found in the nucleus and mitochondria. Many studies demonstrated that GSK-3β was implicated in inducing mitochondrial dysfunction. DNA damage induced the interaction between GSK-3β and p53 at the mitochondria, whereas inhibition of GSK-3β blocked caspase activation and suppress apoptosis [108]. GSK-3β phosphorylate VDAC on Thr51 region, which is highly conserved in mitochondrial porins and is in close proximity to Glu72, a residue critical to the binding of VDAC with HK II [109].
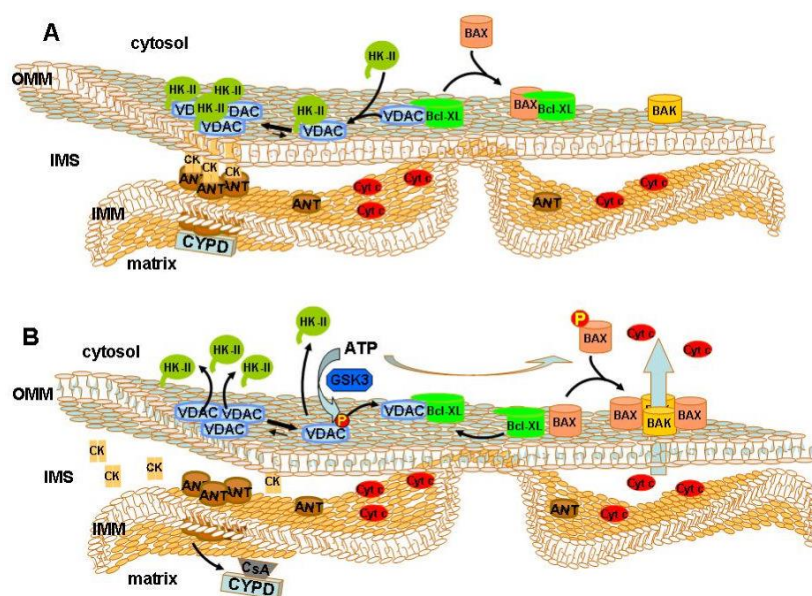
Figure 5.3 Proposed mechanism of HKII-mediated protection against outer mitochondrial membrane (OMM) permeabilization [110].

5.1.4 A new synthesized flavonoid GL-V9 with potential anticancer activity

GL-V9   (5-hydroxy-8-methoxy-7-(4-(pyrrolidin-1-yl)butoxy)-4H-chromen-4-one) is a newly synthesized flavonoid derivatived from natural product wogonin, which has been reported to possess anti-cancer properties in previous studies. GL-V9 inhibits

tumor invasion and metastasis via downregulating the expression and activity of matrix

metalloproteinase-2/9 in MDA-MB-231 and MCF-7 cell lines *in vitro* [111]. It has also

been observed that GL-V9 triggers mitochondria mediated apoptosis and reverses

hypoxia–drug resistance in human hepatocellular carcinoma [112, 113].

Chemical Formula: $C_{24}H_{27}NO_5$
Molecular Weight: 409.47

5-hydroxy-8-methoxy-2-phenyl-7-(4-(pyrrolidin-1-yl)butoxy)-4*H*-chromen-4-one
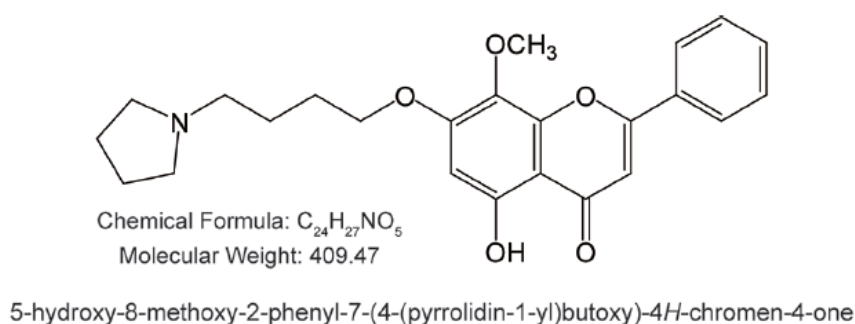
Figure 5.4 Chemical structure of GL-V9

5.2 Materials and Methods

5.2.1 Reagents

GL-V9 (5-hydroxy-8-methoxy-7-(4-(pyrrolidin-1-yl) butoxy)-*4H*-chromen-4-one,

$C_{24}H_{27}NO_5$, MW 409.47, purity>99%) and wogonin (5,7-Dihydroxy-8-methoxy-2-

phenyl-4H-chromen-4-one, $C_{16}H_{12}O_5$, MW 284.27, purity>99%) were dissolved in

dimethyl sulfoxide (Sigma–Aldrich, St. Louis, MO, USA) to 100 mM as a stock

solution, stored at -20 °C, and diluted with medium before each experiment. The final

DMSO concentration did not exceed 0.1% throughout the study. LiCl was purchased

from Sigma-Aldrich and dissolved in distilled water to make a 100 mM stock solution.

Human recombinant IGF-1 was purchased from Merck Millipore (αIGF-1; 10 μg/mL;

Millipore, Ireland). MK-2206 dihydrochloride (MK) was purchased from Santa Cruz

Biotechnology Inc (Santa Cruz, CA) and dissolved in DMSO.

5.2.2 Synthetic route of GL-V9

GL-V9 was synthesized from wogonin (5,7-dihydroxy -8-methoxy-2-phenyl-*4H*-1-

benzopyran-4-one, $C_{16}H_{12}O_5$, MW 284.26). Synthesis of the GL-V9 was initiated from

wogonin, which was react with 1,4-dibromobutane and potassium carbonate by

refluxing in acetone in the presence of K_2CO_3 about 7 hours to give compound 3 (7-(4-

bromobutoxy)-5-hydroxy-8-methoxy-2-phenyl-*4H*-chromen-4-one) . Then the pyrrole

ring was introduced on the bromine of compound 3 by refluxing with tetrahydropyrrole

in acetonitrile about 4~5 hours to obtain GL-V9.
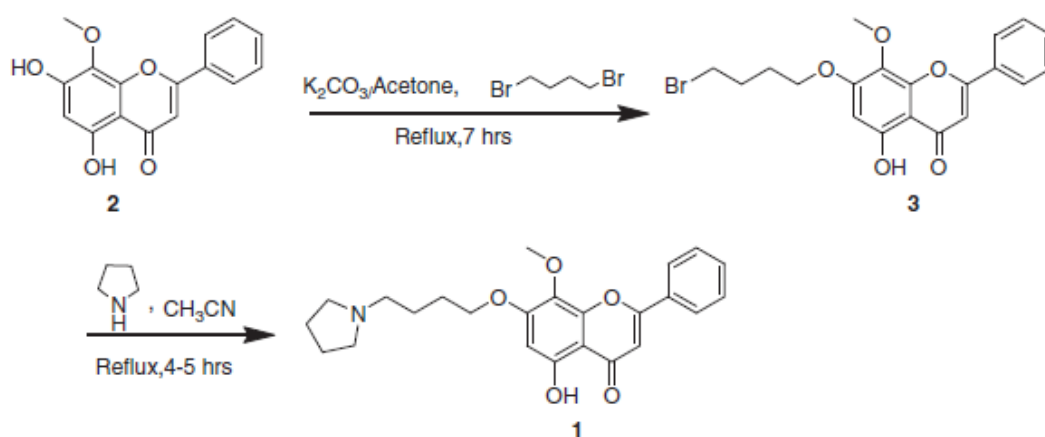
Figure 5.5 The synthetic route of GL-V9. (1) Molecular structure of GL-V9, (2) Molecular structure of wogonin, (3) halogenated hydrocarbons.

5.2.3 In-vitro Study

5.2.3.1 Cell Viability Assays

Cell viability was measured using 3-[4,5-dimethylthiazol-2-yl]-2,5-

diphenyltetrazolium bromide (the MTT assay). Cells (1×10^4) were treated with GL-V9

for 36 h at various concentrations (0~80 μM). Absorbance of the resulting formazan was measured spectrophotometrically at 570 nm using a Universal Microplate Reader EL800 (BIO-TEK instruments, Inc., Vermont, MA).

5.2.3.2 Lactic Acid Production

The generation of lactic acid in cell culture media treated with GL-V9 was assayed using the Lactic Acid Detection kit (KeyGen, Nanjing, China) following the manufacturer's instructions. The assay was monitored spectrophotometrically at 570 nm using the Thermo Scientific Varioskan Flash spectral scanning multimode reader (Thermo, Waltham, MA).

5.2.3.3 ATP Assessment

Cellular ATP concentrations were measured with the ATP Bioluminescent Somatic Cell Assay Kit from Sigma. After cells were incubated with GL-V9 for 36 h, cultured cells were lysed in an ice-cold ATP releasing buffer. Using an ATP standard provided by Sigma, ATP concentrations were then determined with the kit, and normalized to protein concentrations. Aliquots of 100 μL were transferred to white 96-well assay plates. Following the addition of 100 μL luciferin and luciferase, luminescence was monitored on a luminometer Orion II (Berthold DS, Bleichstr, Pforzheim, Germany).

5.2.3.4 Glucose uptake assay

Glucose was assayed using the Amplex Red Glucose Assay Kit (Invitrogen, Eugene, OR). After treatment, media was collected and diluted 1:4,000 with water. The amount

of glucose was detected using a fluorometer (Thermo, Waltham, MA) at Ex./Em. = 530 nm / 590 nm according to the instructions of the assay kit. Glucose uptake was determined by subtracting the amount of glucose in each sample from the total amount of glucose in the media (without cells).

5.2.3.5 Measurements of oxygen consumption

Cells were seeded at a density of 0.2×10^6 cells per well in a 96-well BD Oxygen Biosensor System plate (BD Biosciences, San Jose, CA, USA), and culture media was added until a final volume of 200 µL per well was attained. After drug treatments, the plates were maintained at 37 °C in a humidified incubator with 5% CO_2. Plates were scanned in a temperature-controlled (37 °C) plate reader (Thermo, Waltham, MA) with an excitation wavelength of 485 nm and an emission wavelength of 630 nm at predetermined times for a total of 72 h. The fluorescence traces in each well were normalized according to the signal in the air-saturated buffer. Slopes of fluorescence signal were calculated in the dynamic range of measurements to compare the respiratory rates of samples. Normalized relative fluorescence unit represents oxygen consumption.

5.2.3.6 Mitochondrial Membrane Potential Determination

Following treatment, cells were harvested and resuspended with ice-cold PBS (2000 rpm × 5 min). Quantitative changes of mitochondrial membrane potential (MMP) at the early stage of cell apoptosis were measured by the Mitochondrial membrane potential Detection kit (KeyGen, Nanjing, China) with the lipophilic cation 5,5',6,6'-tetrachloro-

1,1',3,3'-tetraethylbenzimidazolcarbocyanine iodide (JC-1) and detected by FACSCalibur flow cytometry (Becton Dickinson, San Jose, CA) .

5.2.3.7 ROS Measurement

ROS level was assessed using the fluorescent dye 2'7'-dichlorfluorescein-diacetate (DCFH-DA, Beyotime Institute of BioTechnology, Haimen, China) following the methods reported by Wei et al [114].

5.2.3.8 Preparation of mitochondrial extracts

After incubation with GL-V9 for 36 h, the fractionation of the mitochondrial protein was extracted with the Mitochondria/Cytosol Fractionation Kit (BioViso, VA, USA). Briefly, 5×10^7 cells were collected by centrifugation at $600 \times g$ for 5 min at 4 °C and washed with ice-cold PBS. Cells were resuspended with 1 mL of $1 \times$ Cytosol Extraction Buffer Mix containing dithiothreitol and protease inhibitors and incubated on ice for 10 min. Then, cells were homogenized in an ice-cold grinder and the homogenate was transferred to a 1.5 ml microcentrifuge tube and centrifuged at $700 \times g$ for 10 min at 4 °C. The supernatant was transferred to a fresh 1.5 mL microcentrifuge tube and centrifuged at $10\,000 \times g$ for 30 min at 4 °C. The supernatant was collected as cytosolic fraction and the pellet was resuspended in 0.1 ml Mitochondrial Extraction Buffer Mix containing DTT and protease inhibitors and then vortexed for 10 s and saved as mitochondrial fraction.

5.2.3.9 Immunoprecipitation

For co-immunoprecipitation of VDAC complexes, VDAC were immunocaptured from mitochondrial extracts. Lysate of mitochondrial fraction (1 mL) containing 1.5 mg total protein was incubated, respectively, with 1 mg VDAC antibody and 20 mL protein A/G-conjugated beads (Santa Cruz Biotechnology, Santa Cruz, CA, USA) overnight. After four washes with TNES buffer, samples were centrifuged at 3000 × g for 2 min and resuspended in 20 mL SDS-sample buffer (0.5 M Tris–HCl, pH6.8, 20% glycerol, 2% SDS, 5% 2-mercaptoethanol, 4% bromophenol blue). For western blot analysis, 10 ml samples were used. The immunocomplexes were analyzed by western blotting and probed with antibody against anti-GSK3β or HKII antibody.

For co-immunoprecipitation of GSK3β complexes, GSK3β were immunocaptured from mitochondrial extracts. The same experimental procedures were conducted as described for VDAC complexes above. The immunocomplexes were analyzed by western blotting and probed with antibody against VDAC or HKII antibody.

5.2.3.10 Statistical evaluation

Data are presented as mean ± S.D. from triplicate parallel experiments unless otherwise indicated. Statistical analysis was performed using one-way ANOVA. Least Significant Difference test and Tukey's HSD test were used for the one-way ANOVA analyses.

5.2.4 *In-vivo* Study

5.2.4.1 *In vivo* tumor growth assay

Female athymic BALB/c nude mice (35-40 days old) with body weight ranging from 18 to 22 g were supplied by the Academy of Military Medical Sciences of the Chinese People's Liberation Army (Certificate No. SYXK-(Su)2016-0010). The animals were kept at 22 ± 2 °C and 55-65% humidity in stainless steel cages under controlled lights (12 h light/day) and were fed with standard laboratory food and water. Animal care was conducted in accordance with the recommendations of the Guide for the Care and Use of Laboratory Animals published by the National Institute of Health, USA. This experiment was conducted in accordance with the guidelines issued by the State Food and Drug Administration (SFDA of China).

Forty nude mice were inoculated subcutaneously with 1×10^7 MDA-MB-231 or MCF-7 cells into the right axilla. After 12 days of growth, tumor sizes were determined using micrometer calipers. Mice with similar tumor volumes (mice with tumors that were too large or too small were eliminated) were randomly divided into the following five groups (6 mice per group): saline control, GL-V9 (20 mg/kg, i.v., every 2 days), wogonin (6 mg/kg, i.v., every 2 days), and Taxol (8 mg/kg, i.v., twice a week). Tumor sizes were measured every 3 days using micrometer calipers and tumor volume was calculated using the following formula: TV (mm^3) =$d^2 \times$ D/2, where d and D were the shortest and the longest diameter, respectively. Mice were sacrificed on day 21, and tumor tissues were used for immunofluorescence and immunohistochemistry assays.

5.2.4.2 Immunohistochemistry & Immunofluorescence for tumor tissue

The expressions of GSK3β, p-GSK3β, AKT, p-AKT in the tumor tissue were assessed by the SP immunohistochemical method using a rabbit-antihuman monoclonal antibody and an Ultra-Sensitive SP kit (kit 9710 MAIXIN, Maixin-Bio Co., Fujian, China). Tissue sections (4-mm thick) were placed onto treated slides (Vectabond, Vector Laboratories, Burlingame, CA, USA). Sections were heat-fixed, deparaffinized, and rehydrated through a graded alcohol series (100, 95, 85, 75%) to distilled water. Tissue sections were boiled in citrate buffer at high temperature for antigen retrieval, and treated with 3% hydrogen peroxide to block endogenous peroxidase activity. The slides were incubated with a protein-blocking agent (kit 9710 MAIXIN, Maixin-Bio Co., Fuzhou, Fujian) prior to the application of the primary antibody, and then incubated with the primary antibody at 4 °C overnight. The tissues were then incubated with the secondary biotinylated antispecies antibody and labeled using a modified staining procedure based on avidin-biotin complex immunoperoxidase following the instructions provided by the manufacturer of the Ultra-Sensitive SP kit.

For immunofluorescence of tumor tissue, Tissue sections were processed to incubation with primary antibodies overnight at 4 °C as the same as the instruction of immunohistochemistry. Then the slides were washed exposed to FITC-conjugated and PE-conjugated secondary antibodies (1:1000, Invitrogen, CA, USA). A laser scanning confocal microscope FV10-ASW [Ver 2.1] (Olympus Corp, MPE FV1000) was used for co-localization analysis.

5.3 Results & Discussion

5.3.1 GL-V9 had potent anticancer activity in breast cancer cells via mitochondrial-mediated apoptosis

As shown in Figure 5.6, GL-V9 was a novel synthetic flavonoid derived from the natural product wogonin that inhibited the growth and induced apoptosis of various turner cells [115-117]. In previous studies, we have demonstrated that GL-V9 could inhibit the invasion of human breast carcinoma cells [111]. However, the inhibitory effect of GL-V9 on the growth of breast cancer has not been reported. As shown in Figure 5.7, compared with wogonin, GL-V9 has stronger capcity to inhibit the growth of human breast cancer cells. IC50 values of 36 h GL-V9 treatment were 14.90 ± 1.26 μM and 17.81 ± 2.08 μM for MDA-MB-231 and MCF-7 cells, respectively. And for wogonin, the IC_{50} values were 109.22 ± 4.08 μM in MDA-MB-231 cells and 98.53 ± 2.23 μM in MCF-7 cells.
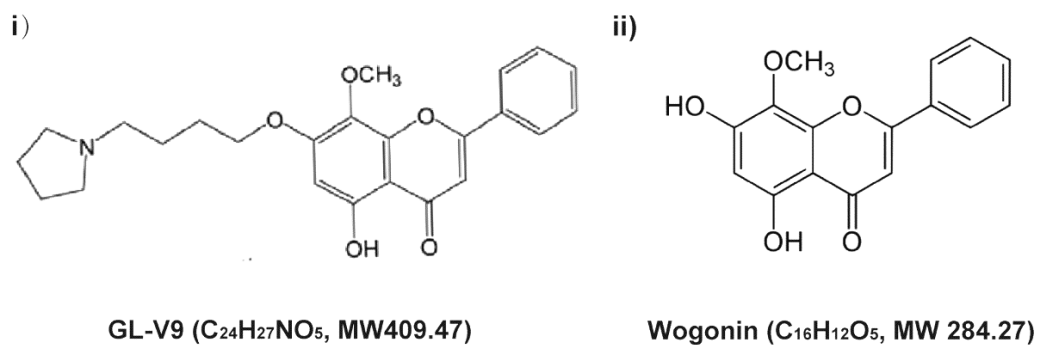
Figure 5.6 Chemical structure of GL-V9 and Wogonin. i) GL-V9 (5-hydroxy-8-methoxy-7-(4-(pyrrolidin-1-yl)butoxy)-4H-chromen-4-one, $C_{24}H_{27}NO_5$). ii) wogonin (5,7-Dihydroxy-8-methoxy-2-phenyl-4H-chromen-4-one, $C_{16}H_{12}O_5$).
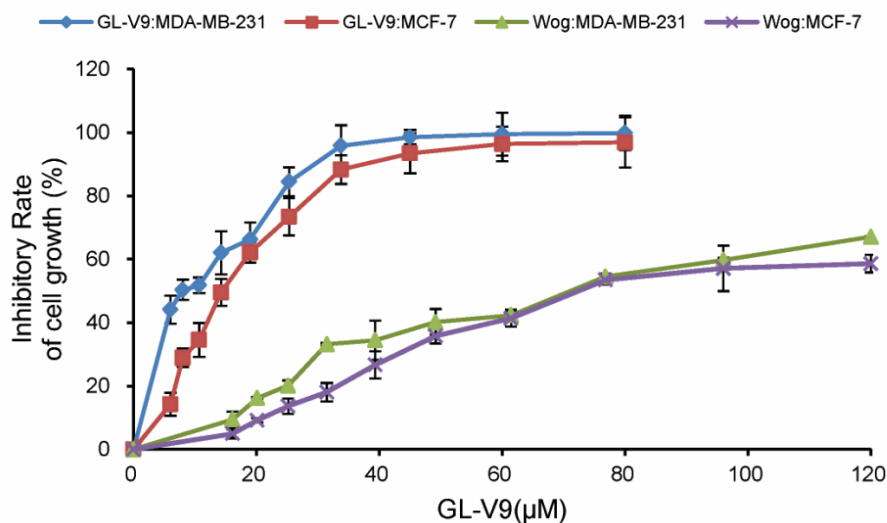
Figure 5.7 Cell growth inhibition as assayed by MTT. Bars represent SD (±).

To investigate the effect of GL-V9 on inducing apoptosis, fluorescent microscope was employed. It is observed that untreated MDA-MB-231 and MCF-7 cells stained equally with blue fluorescence, demonstrating steady chromatinic distribution in nucleolus. After treatment with 10 μM GL-V9, cells showed an early symptom of apoptosis and emitted bright fluorescence due to chromatin agglutination and nucleolus pyknosis. At concentrations of 20 and 30 μM GL-V9, cellular nucleus disintegrated and formed many nuclear fragments in both cells (Figure 5.8). Upon 30 μM wogonin, only MCF-7 cells showed nuclear fragments, instead MDA-MB-231 not. As shown in Figure 5.9, the extent of GL-V9 induced apoptosis in MDA-MB-231 and MCF-7 cells is directly correlated to the concentration of the compound used. Compared to wogonin, GL-V9 is more than 3 time more efficient in promoting apoptosis in MDA-MB-231 and MCF-7 cells.
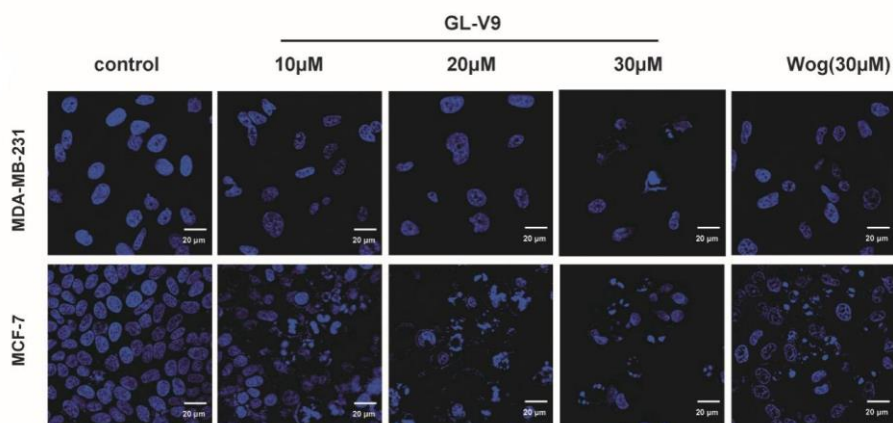
Figure 5.8 Nucleolus morphologic changes induced by wogonin observed under fluorescent microscope (400×).
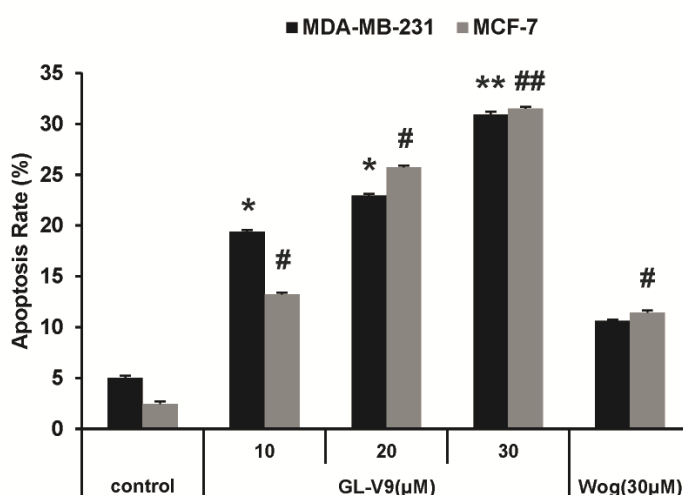
Figure 5.9 Annexin-V/PI double-staining assay. Histograms of apoptosis rates were quantitated using both early and late apoptotic rates. Bars represent SD, $^*p<0.05$ or $^{**}p<0.01$ versus non-treated control of MDA-MB-231 cells, $^{\#}p<0.05$ or $^{\#\#}p<0.01$ versus non-treated control of MCF-7 cells.

To further study the mechanisms of GL-V9 induced apoptosis, we measured the expression of key apoptosis proteins in MDA-MB-231 and MCF-7 cells. As shown in Figure 5.10, upon treatment with GL-V9, caspase 3 was proteolytically activated, and the expression of caspase 9, Bcl-2 and Bcl-xl was notably decreased, while Bax was increased. And GL-V9 induced the loss of mitochondrial membrane potential (MMP) in the two breast cancer cell lines (Figure 5.11). Moreover, the amount of Cyt c

decreased in mitochondria but increased in the cytosol following GL-V9 treatment (Figure 5.12), and ROS level was increased as well (Figure 5.13). Little effects on these mitochondrial apoptosis indexes were observed in the two cancer cell lines when treated with comparable concentrations (30 μM) of the parent compound wogonin. These results suggested that GL-V9, more effective than wogonin, inhibited growth and induced mitochondrial-mediated apoptosis in human breast cancer cells.
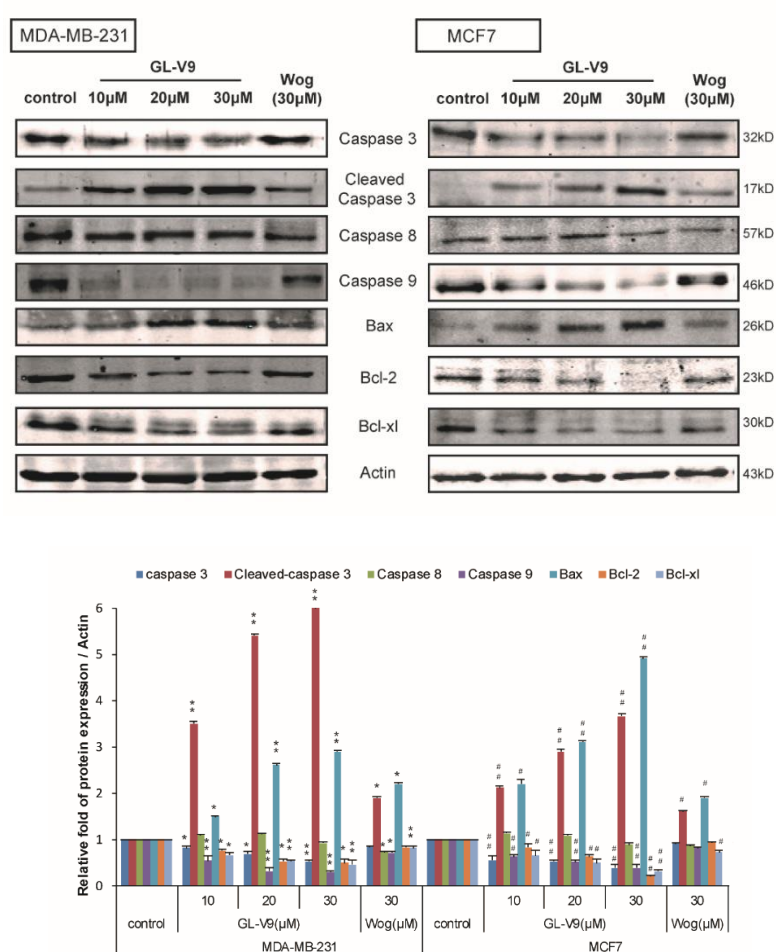
Figure 5.10 Western blot assays for the expressions of apoptosis-associated proteins. The changes of protein expressions were quantified. Bars represent SD, *p<0.05 or **p<0.01 versus non-treated control of MDA-MB-231 cells, #p<0.05 or ##p<0.01 versus non-treated control of MCF-7 cells.
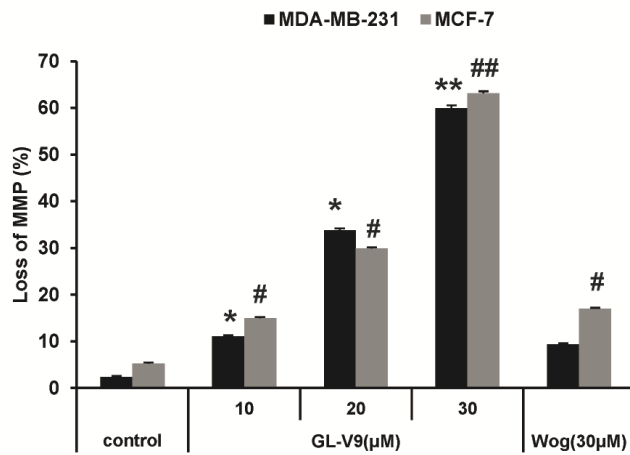
Figure 5.11 JC-1 assay was analyzed by flow cytometry. The percentages of the loss of MMP were represented by histograms. Bars represent SD, $^*p<0.05$ or $^{**}p<0.01$ versus non-treated control of MDA-MB-231 cells, $^\#p<0.05$ or $^{\#\#}p<0.01$ versus non-treated control of MCF-7 cells.
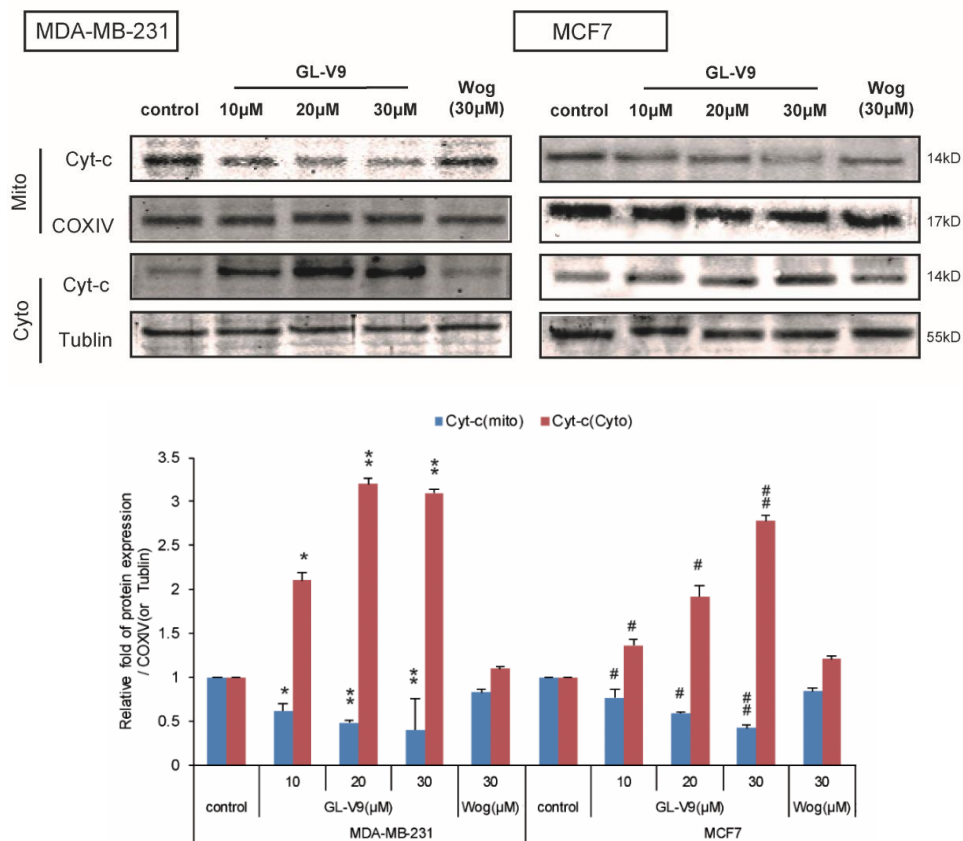
Figure 5.12 Western blot assays were used to examine the expressions of cyt-c in mitochondrial and cytosolic fractions. The changes of protein expressions were quantified. Bars represent SD, $^*p<0.05$ or $^{**}p<0.01$ versus non-treated control of MDA-MB-231 cells, $^\#p<0.05$ or $^{\#\#}p<0.01$ versus non-treated control of MCF-7 cells.

106
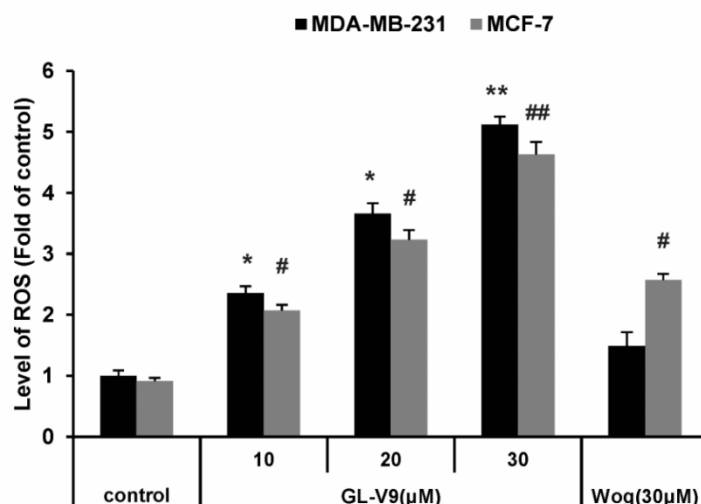
Figure 5.13 The level of ROS detected by flow cytometry (Ex/Em = 488 nm/525 nm). Bars represent SD, $^*p<0.05$ or $^{**}p<0.01$ versus non-treated control of MDA-MB-231 cells, $^#p<0.05$ or $^{##}p<0.01$ versus non-treated control of MCF-7 cells.

5.3.2 GL-V9 suppressed glycolysis of human breast cancer cells

Since GL-V9 induced mitochondrial dysfunction in breast cancer cells, it may influence other mitochondrial functions, especially energy metabolism. Energy exhaustion was a significant reason for the inhibition of rapidly growing cancer cells. Cancer cells show an increased dependence on glycolysis to meet their energy needs, regardless of whether they were well-oxygenated or not. Here, we investigate the influence of GL-V9 on the aerobic glycolysis in human breast cancer cell lines MDA-MB-231 and MCF-7. To exclude the influence of apoptotic death in metabolic evaluation, we performed a kinetic analysis of cell death and cell growth inhibition from 12 h to 36 h. As shown in Figure 5.14, no obvious cell death of MDA-MB-231 and MCF-7 cells happened within 24 h treatment of GL-V9. After 24h treatment, cell survial ratios were rapidly decreased, especially upon 30 μM GL-V9. We further assayed the apoptosis rates induced by 24 h treatment of GL-V9. The result showed

that the apoptosis rates were all less than 10% upon 10 μM, 20 μM and 30 μM GL-V9

in both cell lines (Figure 5.15). Thus, we conducted metabolic evaluation upon 24 h

GL-V9 treatment, which inhibited cell growth, but did not induce apoptotic cell death.
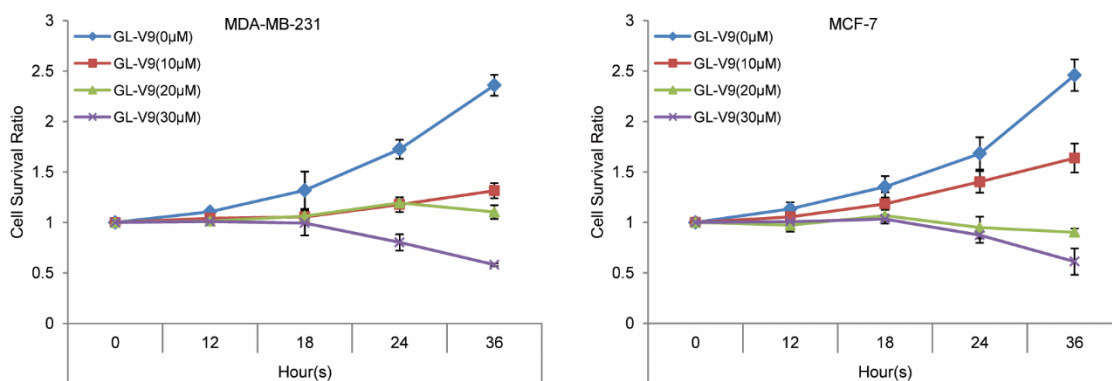
Figure 5.14 Growth inhibition of MDA-MB-231 and MCF-7 cells treated by GL-V9 druing 0-36 h were assayed by MTT. Bars represent SD (±).
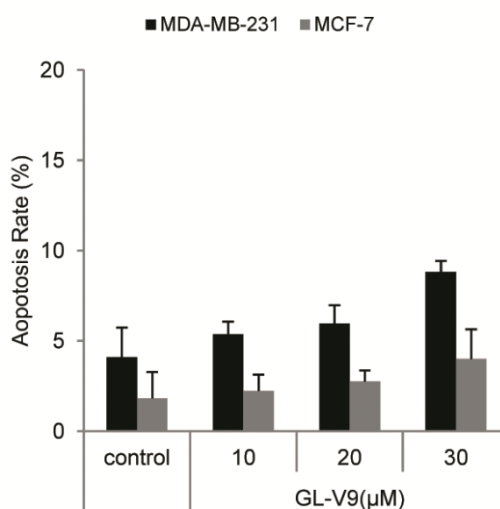
Figure 5.15 Annexin-V/PI double-staining assay of MDA-MB-231 and MCF-7 cells treated by GL-V9 for 24 h.

After treatment with GL-V9 for 24 h, the lactate generation, glucose uptake and ATP

production of MDA-MB-231 and MCF-7 cells were all decreased (Figure 5.16, 5.17

and 5.18). The degree of reduction in these glycolysis indexes depends strongly on the

concentration of GL-V9. Finally, it is noticed that treatment with GL-V9 significantly promoted the oxygen consumption of human breast cancer cells between 12 h to 36 h (Figure 5.19). These results indicated that GL-V9 suppressed glycolysis of breast cancer cells.
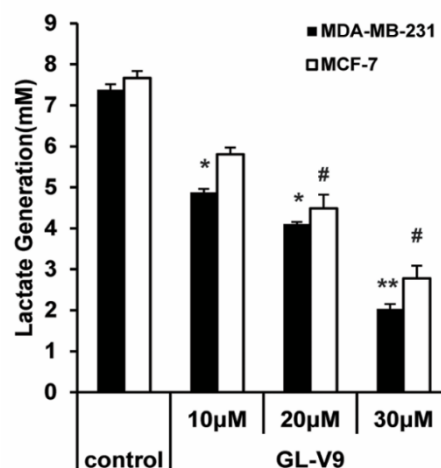
Figure 5.16 Production of lactic acid as assayed with a Lactic Acid production Detection kit. Bars represent SD, $^{*}p<0.05$ or $^{**}p<0.01$ versus non-treated control of MDA-MB-231 cells, $^{#}p<0.05$ or $^{##}p<0.01$ versus non-treated control of MCF-7 cells.
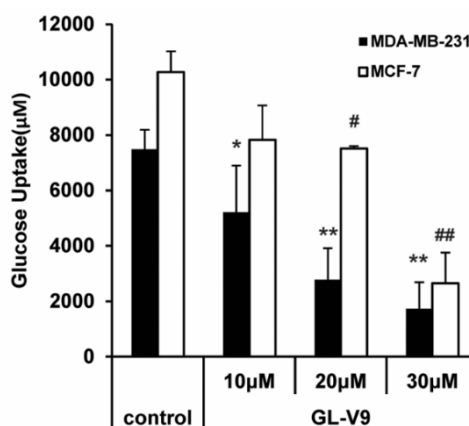
Figure 5.17 Glucose uptake measured using the Amplex Red assay. Bars represent SD, $^{*}p<0.05$ or $^{**}p<0.01$ versus non-treated control of MDA-MB-231 cells, $^{#}p<0.05$ or $^{##}p<0.01$ versus non-treated control of MCF-7 cells.
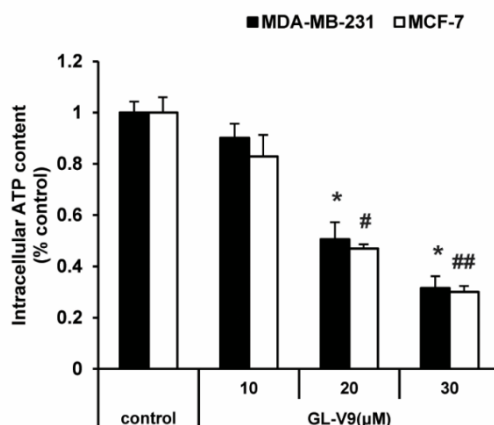
Figure 5.18 Quantification of ATP generation detected by the luminometer Orion II. Bars represent SD, $^*p<0.05$ or $^{**}p<0.01$ versus non-treated control of MDA-MB-231 cells, $^#p<0.05$ or $^{##}p<0.01$ versus non-treated control of MCF-7 cells.
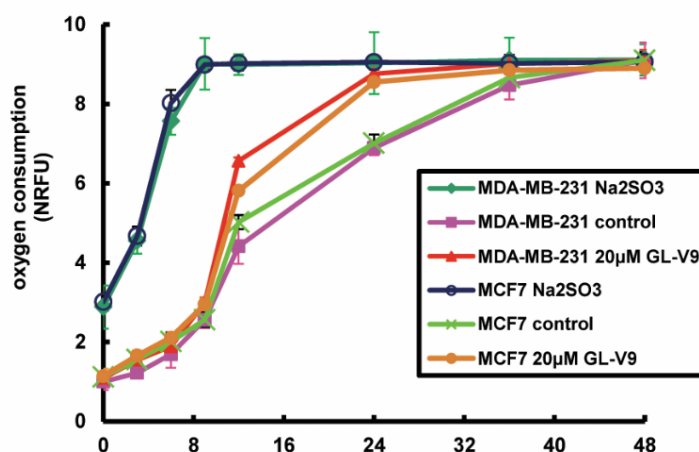

Figure 5.19 Oxygen consumption detected by BD Oxygen Biosensor System plate. Bars represent SD.

5.3.3 The dissociation of HK II from mitochondria accounts for GL-V9 induced mitochondrial dysfunction and apoptosis

The data above demonstrated that GL-V9 could induce mitochondrial-mediated apoptosis and inhibit glycolysis. Whether there were some relationships between the apoptosis-inducing effect and glycolysis modulation? It has been reported that HK II plays a significant role in both glycolysis and mitochondrial homeostasis [104]. Therefore, we investigated the influence of GL-V9 on mitochondrial HKII in human breast cancer cell lines MDA-MB-231 and MCF-7. 2-deoxy-D-glucose (2-DG), a

110

proven inhibitor that preferentially interfere with the glycolytic pathway in human breast cancer cells by modulating mitochondria HKII [118], was used as a positive control. 15 mM 2-DG for 36 h could induced obvious apoptosis in MDA-MB-231 and MCF-7 cells (Figure 5.20). As shown in Figure 5.21, the level of total and mitochondrial HKII were both decreased notably with 20 and 30 μM GL-V9 treatment for 36 h. Little changes on HKII and VDAC were observed for cells treated with 10 μM GL-V9. Whereas, 15 mM 2-DG only decreased mitochondrial HKII.
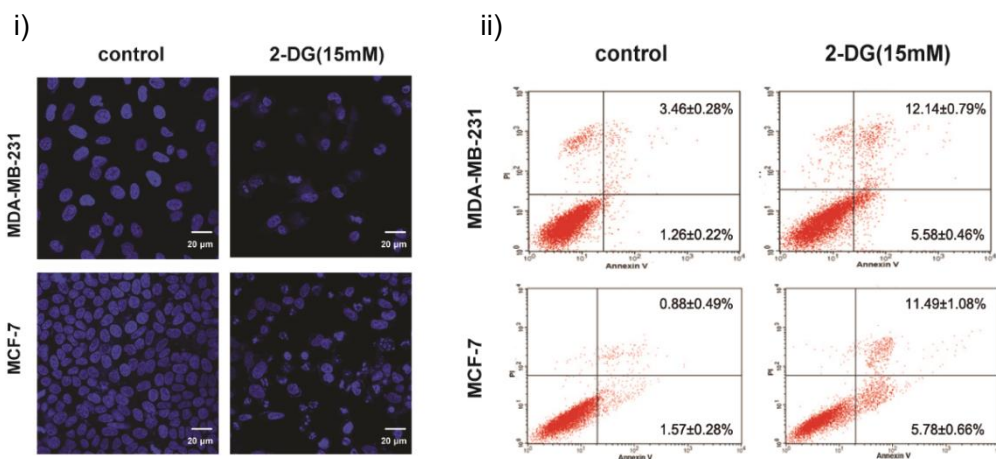
Figure 5.20 Apoptosis induced by 2-DG in human breast cancer cell. 15 mM 2-DG for 36 h could induced obvious apoptosis in MDA-MB-231 and MCF-7 cells. i) Nucleolus morphologic changes induced by 2-DG. ii) Annexin-V/PI double-staining assay of MDA-MB-231 and MCF-7 cells treated by 2-DG.
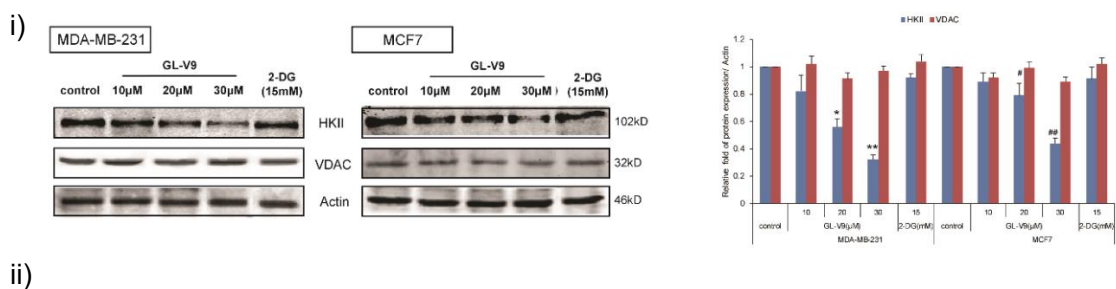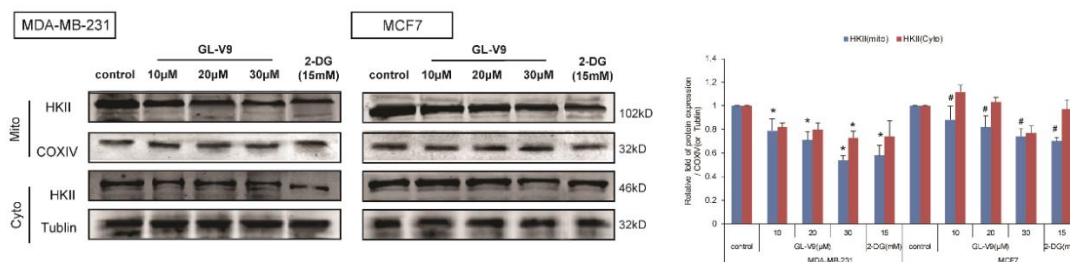
Figure 5.21 Changes in HK expression in GL-V9 treated human breast cancer cells. i) The total amount of HKII and VDAC. ii)Mitochondrial and cytosolic fractions of HK II after treatment. The changes of protein levels were quantified. Bars represent SD, $^*p<0.05$ or $^{**}p<0.01$ versus non-treated control of MDA-MB-231 cells, $^#p<0.05$ or $^{##}p<0.01$ versus non-treated control of MCF-7 cells.

Moreover, the co-localization of HKII with VDAC in human breast cancer cells was detected by immunofluorescence assay (Figure 5.22). In untreated cells, intense staining of HKII was detected and co-localized with mitochondrial marker TOMM20. After GL-V9 and 2-DG treatment, faint diffuse staining of HKII was detected in the cytosol, indicative of weaker co-localization of HKII with mitochondria. The subcellular localization of HKII was interdependent, to a large extent, on the interaction strength of HKII/VDAC[119]. Therefore, to further verify whether the decrease of mitochondrial HKII was caused by an influence of total protein level or a decrease in its binding ability with VDAC in mitochondria, we detected the binding of mitochondrial HKII and VDAC by immunoprecipitation assay. It is found that GL-V9 effectively suppressed the binding of HKII with VDAC in mitochondrial (Figure 5.23).
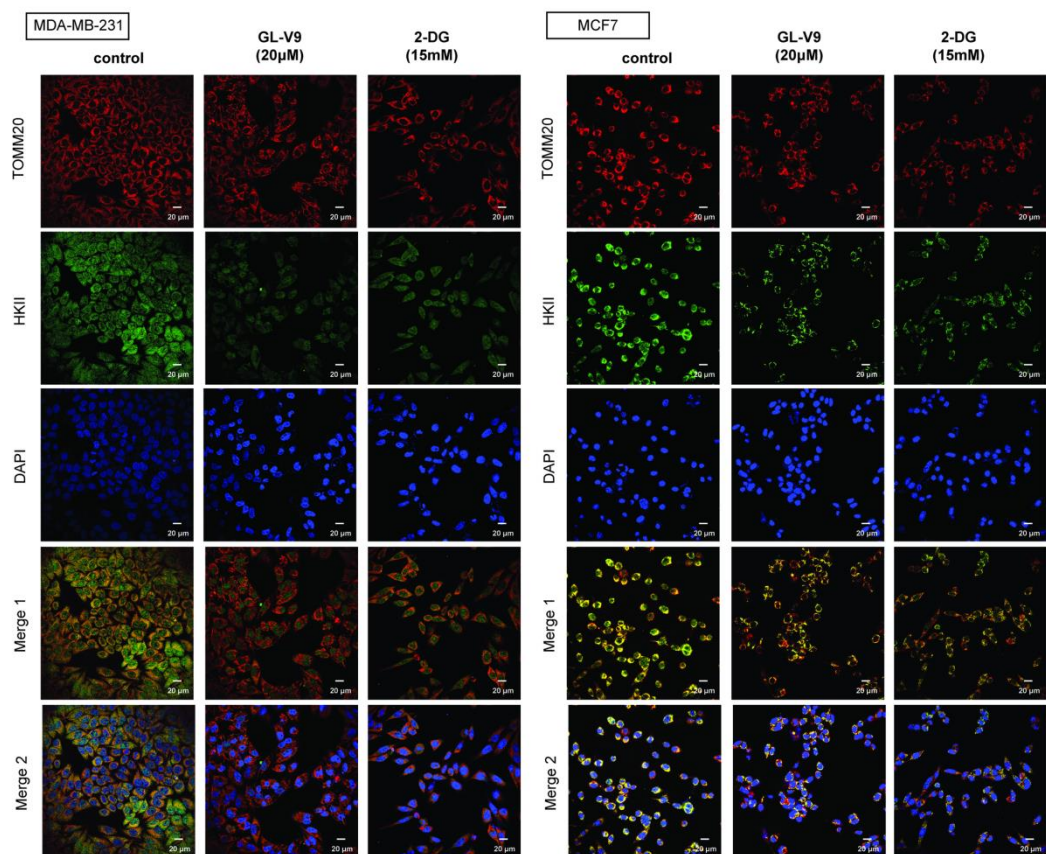
Figure 5.22 The co-localization of HKII with VDAC in human breast cancer cells detected by immunofluorescence assay.
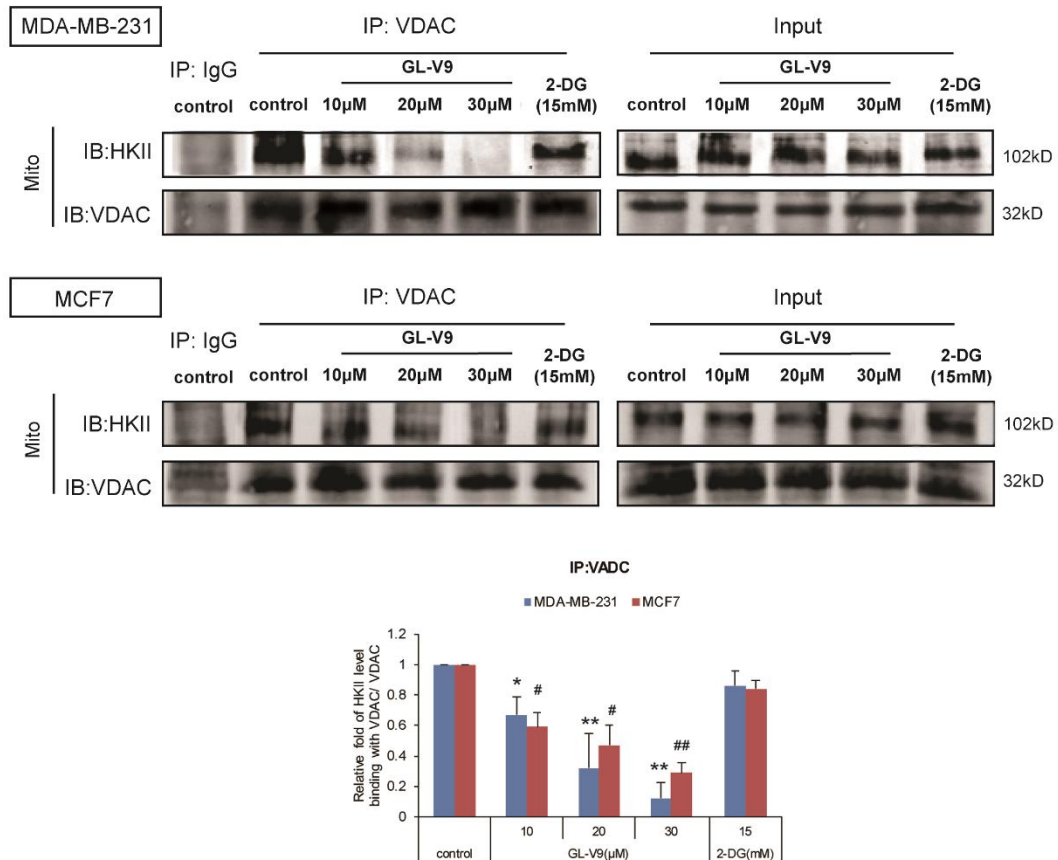
Figure 5.23 The binding of mitochondrial HKII and VDAC detected by immunoprecipitation assay. Western blot assays were performed for HK II and VDAC. The changes of protein levels were quantified. Bars represent SD, $^*p<0.05$ or $^{**}p<0.01$ versus non-treated control of MDA-MB-231 cells, $^{\#}p<0.05$ or $^{\#\#}p<0.01$ versus non-treated control of MCF-7 cells.

5.3.4 The phosphorylation of VDAC by GSK-3β was involved in GL-V9-induced dissociation of HKII from mitochondria

The interaction of hexokinase with mitochondria is regulated to facilitate apoptotic effects [14]. We used LiCl (a GSK-3β inhibitor which can induce the autophosphorylation of GSK-3β) to investigate the roles of GSK-3β in the binding of HKII to mitochondria. As shown in Figure 5.24, LiCl inhibited the interaction between HKII and VDAC in both MDA-MB-231 and MCF-7 cells. Although both total and mitochondrial GSK-3β levels were increased with GL-V9 treatment, phosphorylated

GSK-3β (GSK-3β(S9)) was actually decreased (Figure 5.25). These results implicated

that GSK-3β was involved in GL-V9-induced dissociation of HK II from VDAC.
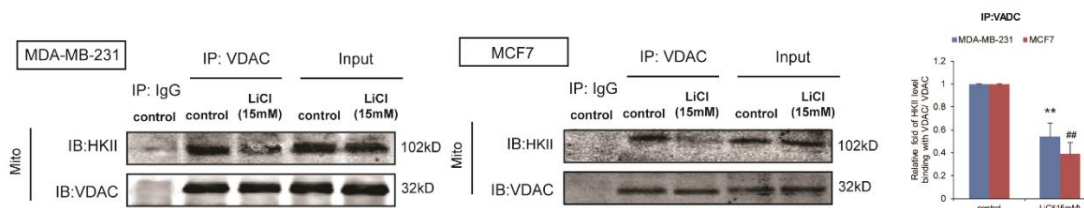
Figure 5.24 The influence of LiCl in interaction between HKII and VDAC. Mitochondria were isolated after LiCl treatment and HK II was immunoprecipitated using VDAC antibody. Western blot assays were performed for HK II and VDAC. The changes of protein levels were quantified. Bars represent SD, $^*p<0.05$ or $^{**}p<0.01$ versus non-treated control of MDA-MB-231 cells, $^\#p<0.05$ or $^{\#\#}p<0.01$ versus non-treated control of MCF-7 cells.
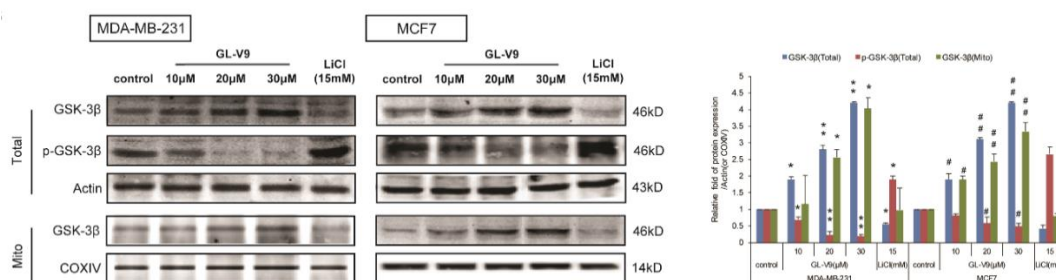

Figure 5.25 The influences of GL-V9 in the expressions of GSK-3β and phosphorylated GSK-3β (GSK-3β(s9)). The expressions of GSK-3β and p-GSK-3β in total proteins and mitochondrial were assayed by Western blot. The changes of protein levels were quantified. Bars represent SD, $^*p<0.05$ or $^{**}p<0.01$ versus non-treated control of MDA-MB-231 cells, $^\#p<0.05$ or $^{\#\#}p<0.01$ versus non-treated control of MCF-7 cells.

This implication is corroborated by our immunoprecipitation experiment that

confirms the binding of GSK-3β with VDAC in mitochondria instead of HKII (Figure

5.26). As shown in Figure 5.27, GL-V9 promoted the binding of mitochondrial GSK-

3β with VDAC, and phosphorylation of GSK-3β induced by LiCl reversed the effects

of GL-V9. All these results suggested that GL-V9 promoted the binding of GSK-3β

with VDAC in mitochondria, facilitating the phosphorylation of VDAC and consequently, the dissociation of HK II from VDCA.
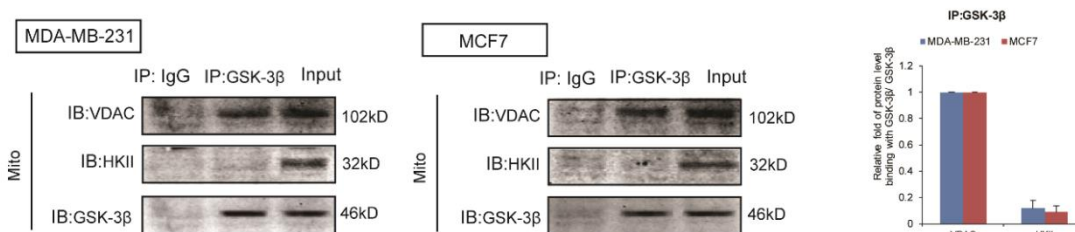
Figure 5.26 The binding of GSK-3β with VDAC and HKII in mitochondria. Mitochondria were isolated and HK II as well as VDAC was immunoprecipitated using GSK-3β antibody. Western blot assays were performed for HK II, VDAC and GSK-3β. The changes of protein levels were quantified. Bars represent SD, $^*p<0.05$ or $^{**}p<0.01$ versus non-treated control of MDA-MB-231 cells, $^\#p<0.05$ or $^{\#\#}p<0.01$ versus non-treated control of MCF-7 cells.
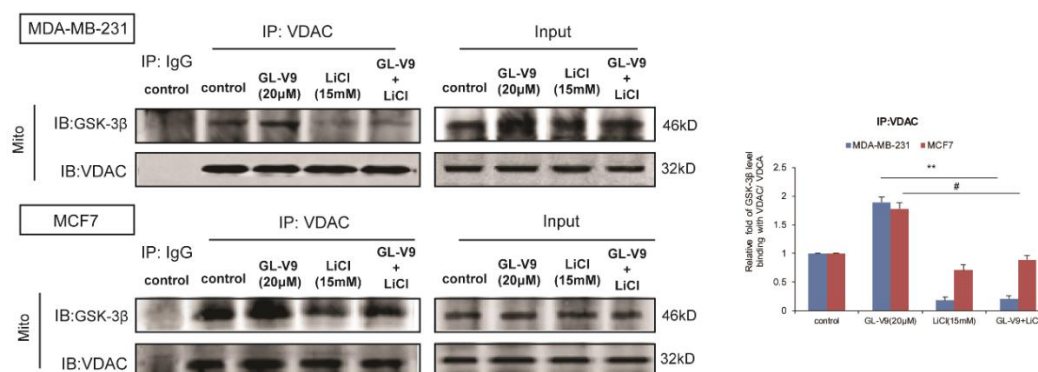
Figure 5.27 The influence of LiCl in the binding of mitochondrial GSK-3β with VDAC that was promoted by GL-V9. Mitochondria were isolated after GL-V9 with/without LiCl treatment and VDAC was immunoprecipitated using GSK-3β antibody. Western blot assays were performed for VDAC and GSK3β. The changes of protein levels were quantified. Bars represent SD, $^*p<0.05$ or $^{**}p<0.01$ versus non-treated control of MDA-MB-231 cells, $^\#p<0.05$ or $^{\#\#}p<0.01$ versus non-treated control of MCF-7 cells.

5.3.5 GL-V9 activated GSK-3β in mitochondria via inhibition of AKT

It has been reported that AKT inhibits the activity of GSK-3β in human neuroblastoma cells by changing its phosphorylation state (phosphorylating Ser9) [120]. Therefore, we investigated the influence of AKT on GSK-3β in human breast cancer

cells. As shown in Figure 5.28, in human breast cancer cells, insulin-like growth factor 1 (IGF1, an AKT activator) promoted the phosphorylation of GSK-3β,whereas MK-2206 (MK, an AKT inhibitor) inhibited the phosphorylation of GSK-3β, in good agreement with literature report [121]. We further noted that IGF blocked the binding of GSK-3β with VDAC in mitochondria (Figure 5.29).
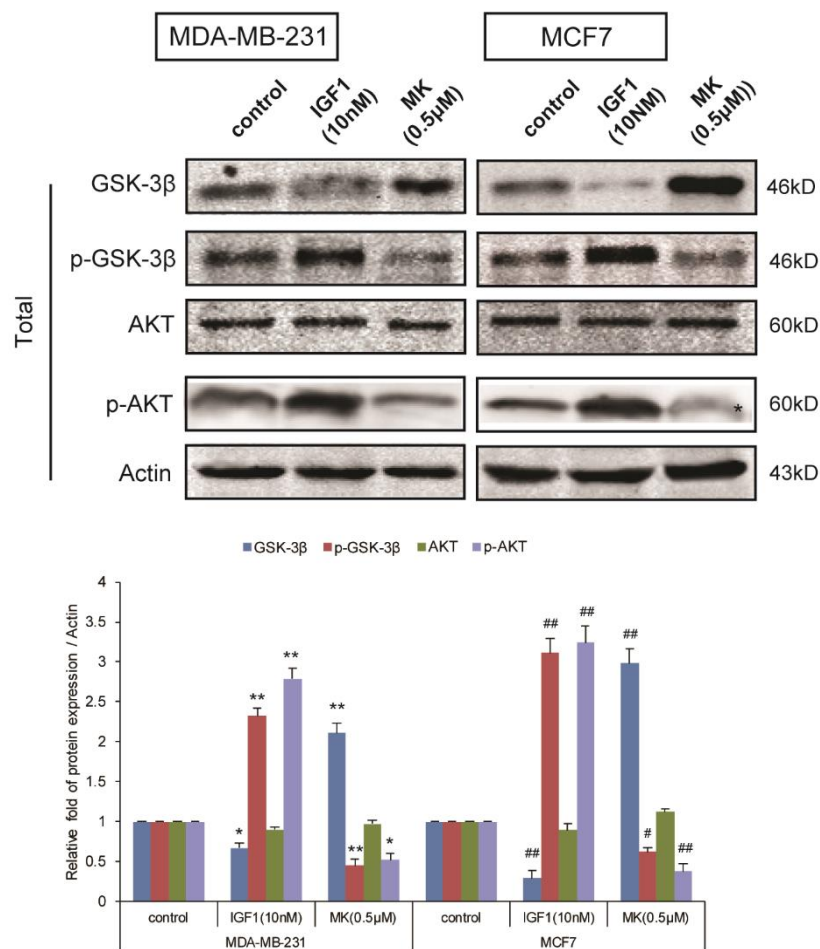
Figure 5.28 The influences of IGF-1 and MK in the activation of AKT and GSK-3β. (A) MDA-MB-231 and MCF-7 treated with AKT activator (IGF-1) or inhibitor (MK). Western blot assays for AKT, p-AKT, GSK-3β and p-GSK-3β. The changes of protein levels were quantified. Bars represent SD, *p<0.05 or **p<0.01 versus non-treated control of MDA-MB-231 cells, #p<0.05 or ##p<0.01 versus non-treated control of MCF-7 cells.
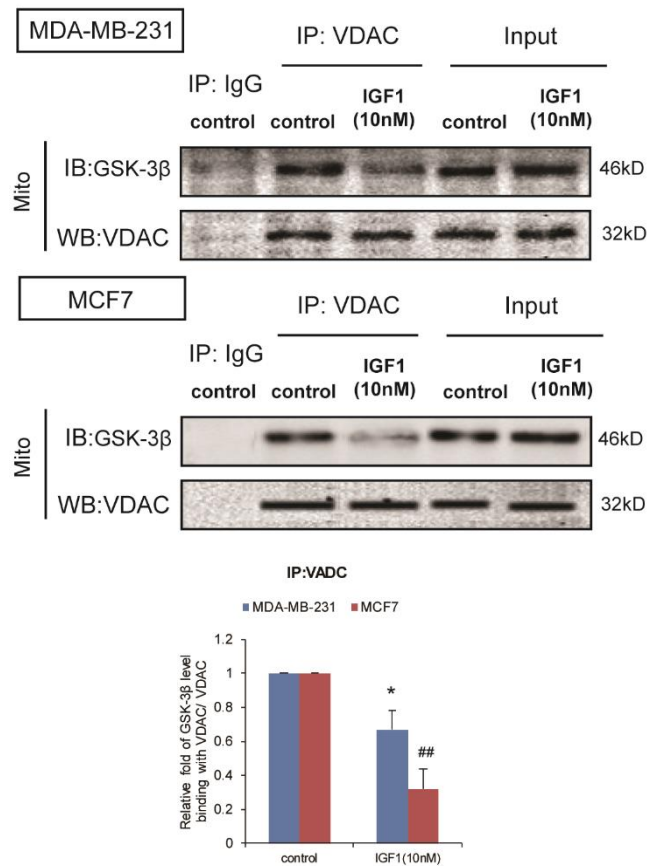
Figure 5.29 The influence of IGF in the binding of GSK-3β with VDAC in mitochondria. Mitochondria were isolated after AKT activator treatment and GSK-3β was immunoprecipitated using VDAC antibody. Western blot assays were performed for GSK-3β and VDAC. The changes of protein levels were quantified. Bars represent SD, $^*p<0.05$ or $^{**}p<0.01$ versus non-treated control of MDA-MB-231 cells, $^\#p<0.05$ or $^{\#\#}p<0.01$ versus non-treated control of MCF-7 cells.

Results shown in Figure 5.30 revealed that GL-V9 not only decreased the expression of AKT but also suppressed its activation, no matter whether GL-V9 induced apoptosis (36 h treatment) or not (24 h treatment). In the presence of IGF, GL-V9-enhanced binding of GSK-3β to VDAC in mitochondria was disturbed (Figure 5.31). These results indicated that inactivation of AKT played important roles in GL-V9-induced activation of GSK-3β in and the dissociation of HKII from mitochondria.

118
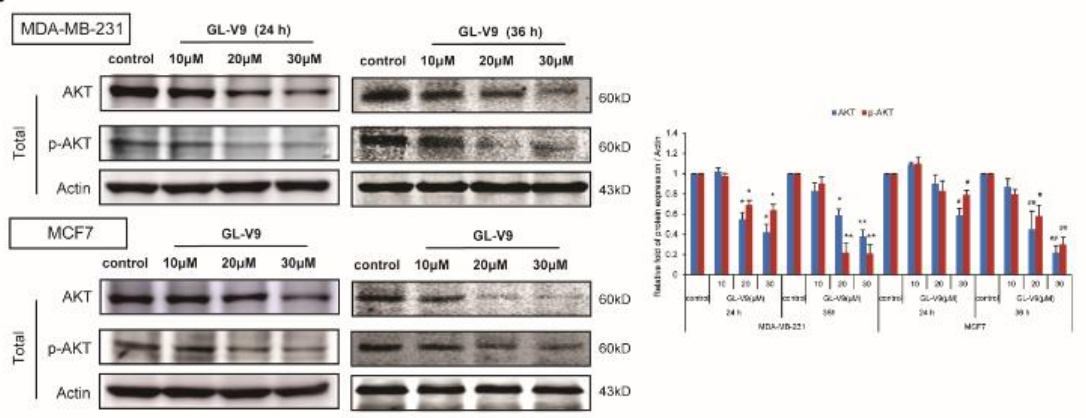
Figure 5.30 The influences of GL-V9 in the expression and activation of AKT. The expressions of AKT and p-AKT (total proteins) upon GL-V9 treatment assayed by Western blot. The changes of protein levels were quantified. Bars represent SD, *p<0.05 or **p<0.01 versus non-treated control of MDA-MB-231 cells, #p<0.05 or ##p<0.01 versus non-treated control of MCF-7 cells.
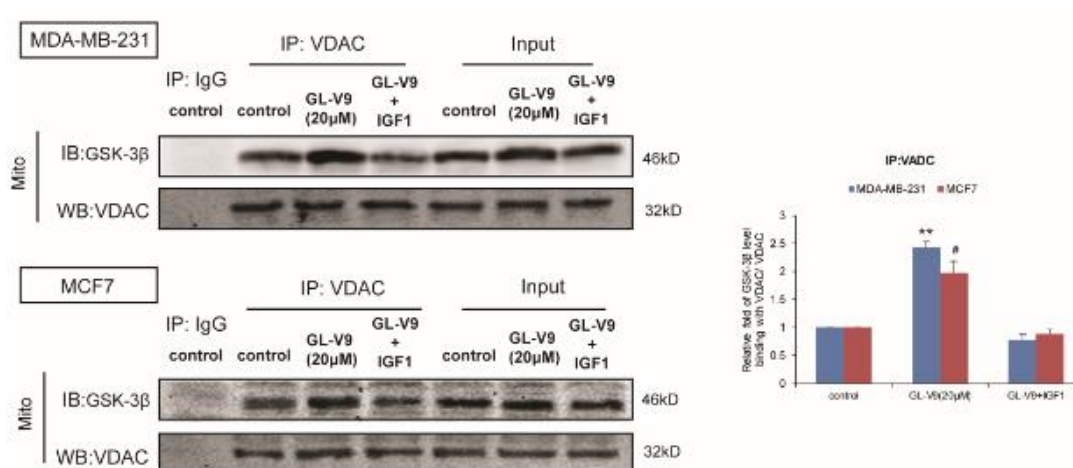
**Figure 5.31 The influence of IGF in GL-V9-enhanced binding of GSK-3β to VDAC in mitochondria. Mitochondria were isolated after GL-V9 with/without IGF-1 treatment and GSK-3β was immunoprecipitated using VDCA antibody. Western blot were performed for VDAC and GSK-3β. The changes of protein levels were quantified. Bars represent SD, *p<0.05 or **p<0.01 versus non-treated control of MDA-MB-231 cells, #p<0.05 or ##p<0.01 versus non-treated control of MCF-7 cells.**

5.3.6 GL-V9 inhibited the growth of tumor via activation of GSK-3β and inactivation of AKT *in vivo*

To verify the results from our *in vitro* studies, we investigated the anticancer effects of GL-V9 on the growth of tumor xenograft models with human MDA-MB-231 or MCF-7 cell lines. As shown in Figure 5.32-5.34, GL-V9 significantly inhibited the

119

growth of tumor in nude mice inoculated with MDA-MB-231 and MCF-7 cells. It is observed that both GL-V9 and wogonin were as effective as positive drug Taxol for tumor inoculated with MDA-MB-231 cells. In mice inoculated with MCF-7 cells, GL-V9 has similar inhibitory effect with Taxol, but more effective than wogonin. It is worth mentioning that GL-V9 treatments had little influence on body weight of the animals (Figure 5.35).
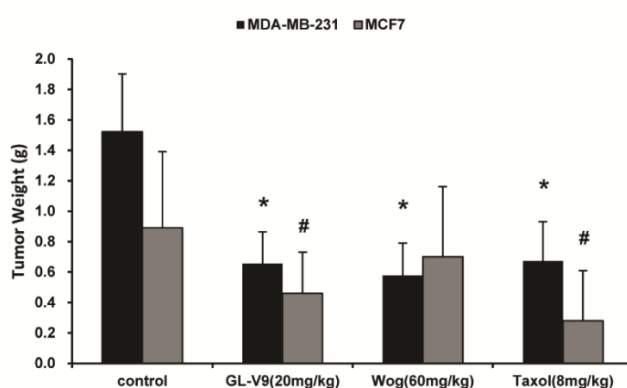
Figure 5.32 The tumor weight of nude mice inoculated with MDA-MB-231 or MCF-7 cells were treated with saline control, GL-V9, wogonin and Taxol. Bars represent SD, $^*p<0.05$ or $^{**}p<0.01$ versus non-treated control group inoculated with MDA-MB-231 cells, $^\#p<0.05$ or $^{\#\#}p<0.01$ versus non-treated control group inoculated with MCF-7 cells.
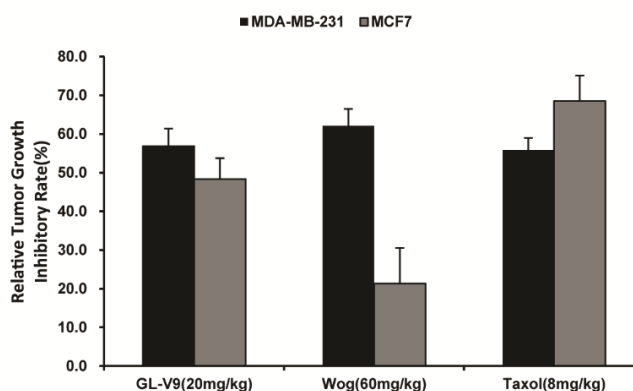
Figure 5.33 The relative tumor growth inhibitory rate of nude mice inoculated with MDA-MB-231 or MCF-7 cells were treated with saline control, GL-V9, wogonin and Taxol.
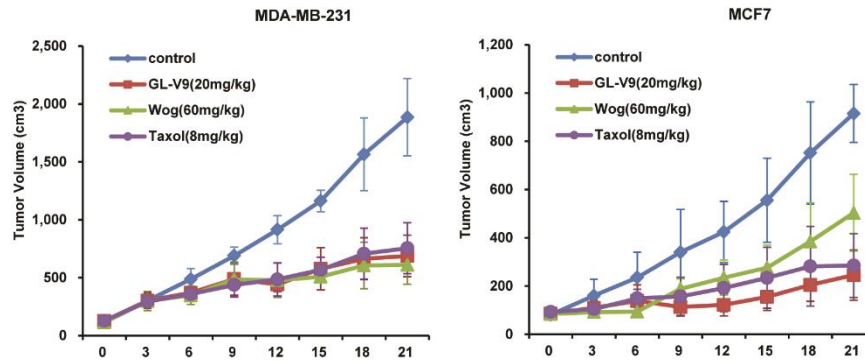
Figure 5.34 The tumor volume of nude mice inoculated with MDA-MB-231 or MCF-7 cells were treated with saline control, GL-V9, wogonin and Taxol. Bars represent SD.
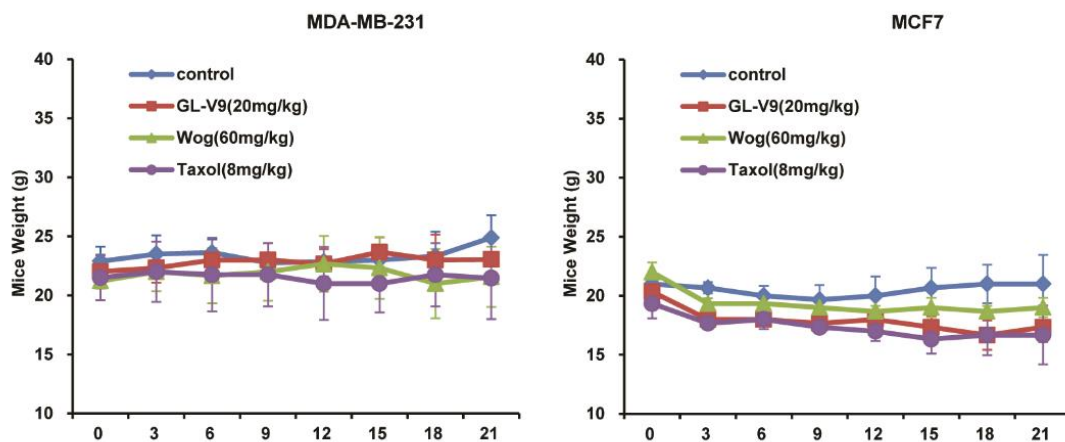
Figure 5.35 The weight of nude mice inoculated with MDA-MB-231 or MCF-7 cells were treated with saline control, GL-V9, wogonin and Taxol. Bars represent SD.

Hematoxylin and eosin (HE) staining showed that GL-V9-treated group displayed stronger infiltration and fewer vessels than the control group (Figure 5.36, Table 5.1 and 5.2). Immunohistochemistry (IHC) assay showed that GL-V9 inhibited the phosphorylation of GSK-3β and the activation of AKT (Figure 5.37), corroborating with our *in vitro* studies described in the previous paragraph.
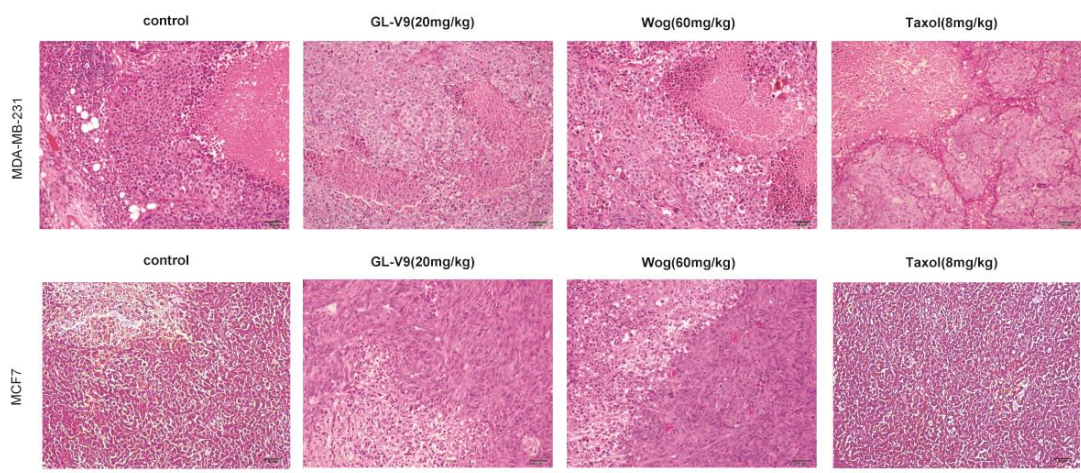
Figure 5.36 Histological analysis were photographed (×100).

Table 5.1 Pathology microscopic examination table for the xenograft tissue of MDA-MB-231 cells.

Treated Groups	Necrosis	Stroma		Infiltration	Score
		Vessel	Hemorrhage		
control	1	1	0.5	1	3.5
GL-V9	0.5	0.5	0.5		1.5
Taxol	1	0.5	0.5		2
Wognin	1	1	1		3

The tumor tissue were assessed by histological analysis. The tags in the table represent the severity :

Minor "±", Mild "1+", Annual "2+", Severe "3+", Extremely severe "4+", and Normal "-" . (H)

Histological analysis were photographed (×100).

Table 5.2 Pathology microscopic examination table for the xenograft tissue of MCF-7 cells.

Treated Groups	Necrosis	Stroma		Infiltration	Score
		Vessel	Hemorrhage		
control	1	1	0.5	1	3.5
GL-V9	1	0.5		0.5	2
Taxol	1	1			2
Wognin	2	0.5			2.5

The tumor tissue were assessed by histological analysis. The tags in the table represent the severity :

Minor "±", Mild "1+", Annual "2+", Severe "3+", Extremely severe "4+", and Normal "-" . (H)

Histological analysis were photographed (×100).
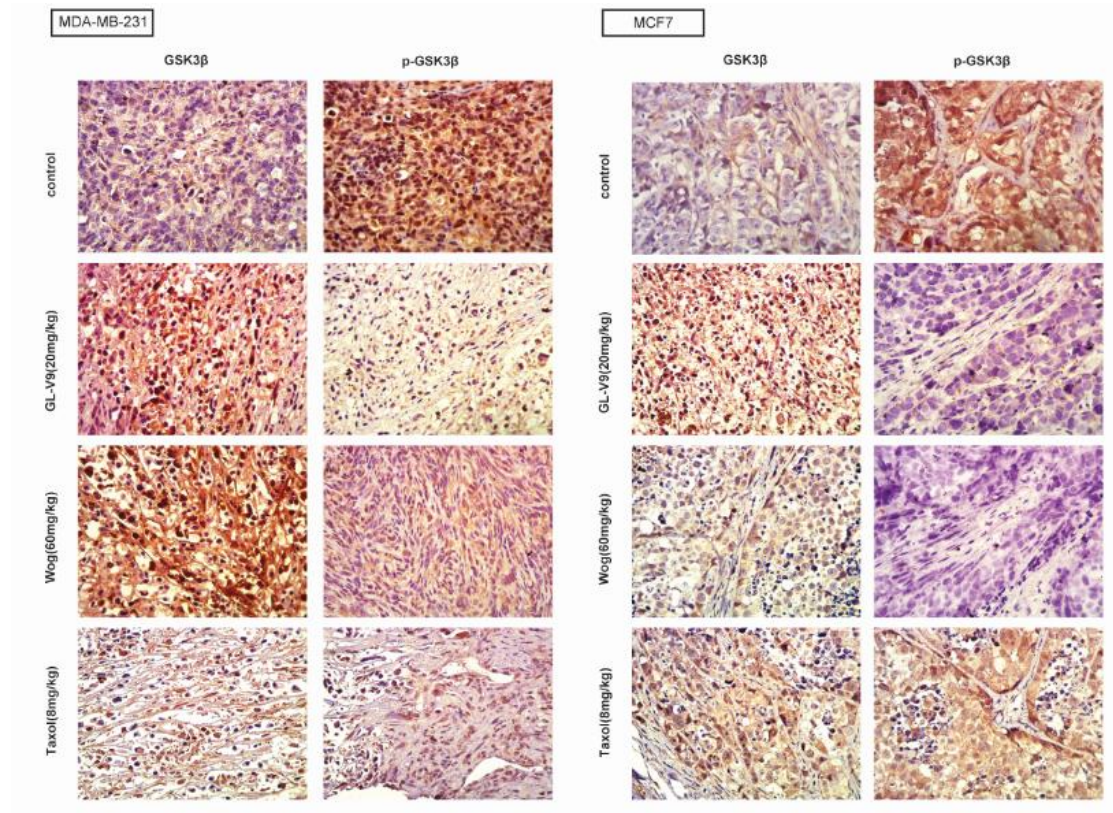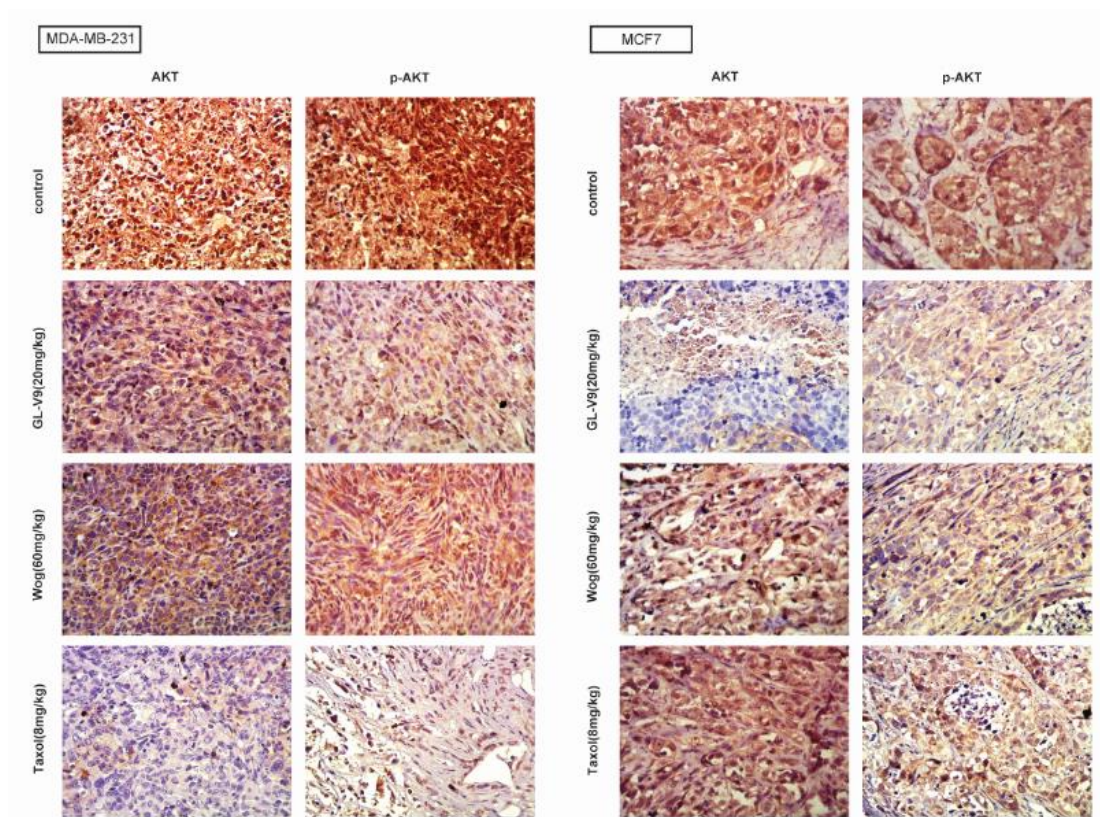
Figure 5.37 Proteins expressions in breast tumor tissue were assessed by immunohistochemistry.

5.4 Conclusion

In this work, we investigated the mechanisms of a newly synthesized flavonoid named GL-V9 in the inhibition of glycolysis and the induction of apoptosis of human breast cancer cell lines MDA-MB-231 and MCF-7 cells. We find that hexokinase II (HKII) plays important roles in the anticancer effects of GL-V9. GL-V9 not only downregulate the expression of HKII in MDA-MB-231 and MCF-7 cells, but also induce dissociation of HKII from voltage-dependent anion channel (VDAC) in mitochondria, resulting in glycolytic inhibition and mitochondrial-mediated apoptosis. The dissociation of HKII from mitochondria is attributed to GSK-3β-induced

phosphorylation of mitochondrial VDAC. Moreover, activation of GSK-3β by GL-V9

was resulted from the direct effect of GL-V9 as well as the inactivation of AKT. Our *in*

vivo experiments also show that GL-V9 significantly inhibits the growth of human

breast cancer due to activation of GSK-3β and inactivation of AKT. Thus, GL-V9

induces cytotoxicity via regulation of HKII binding to mitochondria. Our work

demonstrates the significance of metabolic regulator in cancer growth and offers fresh

insight into the molecular basis for the development of flavonoid as novel agents for

the treatment of breast carcinoma.
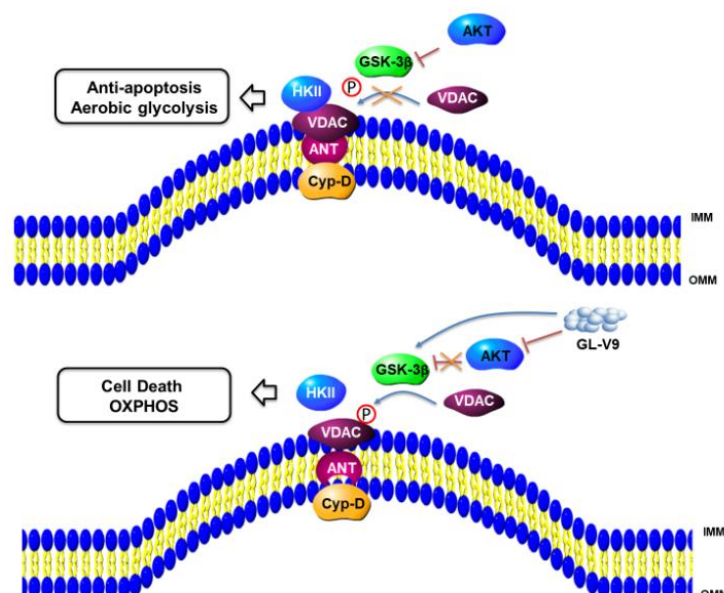
Figure 5.38 Schematic diagram of GL-V9-induced inhibition aerobic glycolysis and apoptosis in human breast cancer cells through GSKβ-mediated disruption of the binding of HKII to mitochondria. The inhibition of Akt causes the activation of GSK3β which could phosphorylate VDAC. VDAC phosphorylated by GSK3β is unable to bind HK II in OMM, thus causing the structural change of mitochondria permeability transition pore, which was composed by VDAC, Cyp-D and ANT. These changes increased outer mitochondrial membrane permeability and resulted in the metabolism switch from glycolysis to OXPHOS. The anticancer effects of GL-V9 is potentiated by detachment of HK II from VDAC, mediated either by inhibition of AKT and the subsequent activation of GSK3β. Cyp-D, cyclophilin D; ANT, adenine nucleotide translocator; IMM, inner mitochondrial membrane; OMM, outer mitochondrial membrane.

In summary, the present study demonstrated that GL-V9 induced apoptosis and inhibited aerobic glycolysis by blocking the binding of mitochondrial HKII with VDAC in human breast cancer cells. The inactivation of AKT and the phosphorylation of VDAC by GSK-3β were responsible for the disassociation of HKII from mitochondria. This work provide mechanistic evidence that GL-V9 is a novel candidate for breast cancer treatment and a potential adjunctive agent for tumor chemotherapy.

The interaction between HKII and mitochondria plays a more important role in regulating apoptotic responsiveness of cells than merely catalyzing metabolic reactions. Notably, investigations have showed that upregulated HK2 expression are associated with drug resistance phenotypes in breast cancer cells [122]. Therefore, HKII may be a genetic modifier of drug resistance that can be therapeutically exploited. And a better understanding of the functional differences of HKII in cancer tissue and normal tissues will undoubtedly contribute to better cancer therapies.

REFERENCES

1. Aoun, S., Chebli, C., and Baloulene, M., *Noncovalent immobilization of chloroperoxidase onto talc: Catalytic properties of a new biocatalyst.* Enzyme And Microbial Technology, 1998. **23**(6): p. 380-385.

2. Aburto, J., Ayala, M., Bustos-Jaimes, I., et al., *Stability and catalytic properties of chloroperoxidase immobilized on SBA-16 mesoporous materials.* Microporous And Mesoporous Materials, 2005. **83**(1-3): p. 193-200.

3. Lakner, F.J. and Hager, L.P., *Chloroperoxidase as enantioselective epoxidation catalyst: An efficient synthesis of (R)-(-)-mevalonolactone.* Journal Of Organic Chemistry, 1996. **61**(11): p. 3923-3925.

4. Bertini, I., Luchinat, C., and Parigi, G., *Magnetic susceptibility in paramagnetic NMR.* Progress In Nuclear Magnetic Resonance Spectroscopy, 2002. **40**(3): p. 249-273.

5. Bertini, I., Luchinat, C., Parigi, G., et al., *NMR spectroscopy of paramagnetic metalloproteins.* Chembiochem, 2005. **6**(9): p. 1536-1549.

6. deRopp, J.S., Mandal, P., Brauer, S.L., et al., *Solution NMR study of the electronic and molecular structure of the heme cavity in high-spin, resting state horseradish peroxidase.* Journal Of the American Chemical Society, 1997. **119**(20): p. 4732-4739.

7. Allain, E.J., Hager, L.P., Deng, L., et al., *Highly Enantioselective Epoxidation Of Disubstituted Alkenes with Hydrogen-Peroxide Catalyzed by Chloroperoxidase.* Journal Of the American Chemical Society, 1993. **115**(10): p. 4415-4416.

8. Omura, T., *Structural diversity of cytochrome P450 enzyme system.* Journal Of Biochemistry, 2010. **147**(3): p. 297-306.

9. Morris, D.R. and Hager, L.P., *Chloroperoxidase. I. Isolation and properties of the crystalline glycoprotein.* J Biol Chem, 1966. **241**(8): p. 1763-1768.

10. Zaks, A. and Dodds, D.R., *Chloroperoxidase-Catalyzed Asymmetric Oxidations - Substrate-Specificity And Mechanistic Study.* Journal Of the American Chemical Society, 1995. **117**(42): p. 10419-10424.

11. Pesic, M., Lopez, C., Alvaro, G., et al., *A novel immobilized chloroperoxidase biocatalyst with improved stability for the oxidation of amino alcohols to amino aldehydes.* Journal Of Molecular Catalysis B-Enzymatic, 2012. **84**: p. 144-151.

12. Zaks, A., Yabannavar, A.V., Dodds, D.R., et al., *A novel application of chloroperoxidase: Preparation of gem-halonitro compounds.* Journal Of Organic Chemistry, 1996. **61**(24): p. 8692-8695.

13. Fu, Y.C., Callaway, Z., Lum, J., et al., *Exploiting Enzyme Catalysis in Ultra-Low Ion Strength Media for Impedance Biosensing of Avian Influenza Virus Using a Bare Interdigitated Electrode.* Analytical Chemistry, 2014. **86**(4): p. 1965-1971.

14. Smith, A.T., Pazicni, S., Marvin, K.A., et al., *Functional Divergence of Heme-Thiolate Proteins: A Classification Based on Spectroscopic Attributes.* Chemical Reviews, 2015. **115**(7): p. 2532-2558.

15. Li, X.L., Zhang, J., Jiang, Y.C., et al., *Highly Efficient Biodecolorization/Degradation of Congo Red and Alizarin Yellow R by Chloroperoxidase from Caldariomyces fumago: Catalytic Mechanism and Degradation Pathway.* Industrial & Engineering Chemistry Research, 2013. **52**(38): p. 13572-13579.

16. Hernandez, K., Berenguer-Murcia, A., Rodrigues, R.C., et al., *Hydrogen Peroxide in Biocatalysis. A Dangerous Liaison.* Current Organic Chemistry, 2012. **16**(22): p. 2652-2672.

17. Sheldon, R.A. and van Pelt, S., *Enzyme immobilisation in biocatalysis: why, what and how.* Chemical Society Reviews, 2013. **42**(15): p. 6223-6235.

18. Barbosa, O., Ortiz, C., Berenguer-Murcia, A., et al., *Strategies for the one-step immobilization-purification of enzymes as industrial biocatalysts.* Biotechnology Advances, 2015. **33**(5): p. 435-456.

19. Garcia-Galan, C., Berenguer-Murcia, A., Fernandez-Lafuente, R., et al., *Potential of Different Enzyme Immobilization Strategies to Improve Enzyme Performance.* Advanced Synthesis & Catalysis, 2011. **353**(16): p. 2885-2904.

20. Liese, A. and Hilterhaus, L., *Evaluation of immobilized enzymes for industrial applications.* Chemical Society Reviews, 2013. **42**(15): p. 6236-6249.

21. Peirce, S., Virgen-Ortiz, J.J., Tacias-Pascacio, V.G., et al., *Development of simple protocols to solve the problems of enzyme coimmobilization. Application to coimmobilize a lipase and a beta-galactosidase.* Rsc Advances, 2016. **6**(66): p. 61707-61715.

22. Singh, R.K., Tiwari, M.K., Singh, R., et al., *Immobilization of L-arabinitol dehydrogenase on aldehyde-functionalized silicon oxide nanoparticles for L-xylulose production.* Applied Microbiology And Biotechnology, 2014. **98**(3): p. 1095-1104.

23. Sundaramoorthy, M., Terner, J., and Poulos, T.L., *Stereochemistry of the chloroperoxidase active site: crystallographic and molecular-modeling studies.* Chemistry & Biology, 1998. **5**(9): p. 461-473.

24. Aitken, M.D., Massey, I.J., Chen, T.P., et al., *Characterization Of Reaction-Products From the Enzyme-Catalyzed Oxidation Of Phenolic Pollutants.* Water Research, 1994. **28**(9): p. 1879-1889.

25. Littlechild, J., *Haloperoxidases and their role in biotransformation reactions.* Current Opinion In Chemical Biology, 1999. **3**(1): p. 28-34.

26. Karam, J. and Nicell, J.A., *Potential applications of enzymes in waste treatment.* Journal Of Chemical Technology And Biotechnology, 1997. **69**(2): p. 141-153.

27. Scarsi, K.K., Olaitan, O.O., Rawizza, H.E., et al., *Building capacity through implementation of a clinical pharmacy training model for HIV medicine.* Pharmacotherapy, 2015. **35**(11): p. E241-E241.

28. Pandey, A., Lee, D.J., Mohan, S.V., et al., *Preface-1st International Conference on Bioresource Technology for Bioenergy, Bioproducts & Environmental Sustainability (BIORESTEC).* Renewable Energy, 2018. **129**: p. 677-677.

29. Hager, L.P., Lakner, F.J., and Basavapathruni, A., *Chiral synthons via chloroperoxidase catalysis.* Journal Of Molecular Catalysis B-Enzymatic, 1998. **5**(1-4): p. 95-101.

30. Huynh, D.L., Sharma, N., Singh, A.K., et al., *Anti-tumor activity of wogonin, an extract from Scutellaria baicalensis, through regulating different signaling pathways.* Chinese Journal Of Natural Medicines, 2017. **15**(1): p. 15-40.

31. Wu, X., Zhang, H.J., Salmani, J.M.M., et al., *Advances of wogonin, an extract from Scutellaria baicalensis, for the treatment of multiple tumors.* Oncotargets And Therapy, 2016. **9**: p. 2935-2943.

32. Zhi, L.F., Jiang, Y.C., Wang, Y.S., et al., *Effects of additives on the thermostability of chloroperoxidase.* Biotechnology Progress, 2007. **23**(3): p. 729-733.

33. Hager, L.P., Morris, D.R., Brown, F.S., et al., *Chloroperoxidase. II. Utilization of halogen anions.* J Biol Chem, 1966. **241**(8): p. 1769-1777.

34. Dai, K., Lu, L.H., Liu, Q., et al., *Sonication assisted preparation of graphene oxide/graphitic-C3N4 nanosheet hybrid with reinforced photocurrent for photocatalyst applications.* Dalton Transactions, 2014. **43**(17): p. 6295-6299.

35. Mandal, P. and Chattopadhyay, A.P., *Excellent catalytic activity of magnetically recoverable Fe3O4-graphene oxide nanocomposites prepared by a simple method.* Dalton Transactions, 2015. **44**(25): p. 11444-11456.

36. Zhang, J., Feng, M.Y., Jiang, Y.C., et al., *Efficient decolorization/degradation of aqueous azo dyes using buffered H2O2 oxidation catalyzed by a dosage below ppm level of chloroperoxidase.* Chemical Engineering Journal, 2012. **191**: p. 236-242.

37. Jiao, R.J., Tan, Y., Jiang, Y.C., et al., *Ordered Mesoporous Silica Matrix for Immobilization of Chloroperoxidase with Enhanced Biocatalytic Performance for Oxidative Decolorization of Azo Dye.* Industrial & Engineering Chemistry Research, 2014. **53**(31): p. 12201-12208.

38. Zhang, J.T., Jiang, J.W., and Zhao, X.S., *Synthesis and Capacitive Properties of Manganese Oxide Nanosheets Dispersed on Functionalized Graphene Sheets.* Journal Of Physical Chemistry C, 2011. **115**(14): p. 6448-6454.

39. Li, Q.Z., Fan, F., Wang, Y., et al., *Enzyme Immobilization on Carboxyl-Functionalized Graphene Oxide for Catalysis in Organic Solvent.* Industrial & Engineering Chemistry Research, 2013. **52**(19): p. 6343-6348.

40. Thy, L.T.M., Thuong, N.H., Tu, T.H., et al., *Synthesis of magnetic iron oxide/graphene oxide nanocomposites for removal of cadmium ions from water.* Advances in Natural Sciences: Nanoscience and Nanotechnology, 2019. **10**(2): p. 025006.

41. Kassaee, M.Z., Motamedi, E., and Majdi, M., *Magnetic Fe3O4-graphene oxide/polystyrene: Fabrication and characterization of a promising nanocomposite.* Chemical Engineering Journal, 2011. **172**(1): p. 540-549.

42. Jung, D., Streb, C., and Hartmann, M., *Oxidation of indole using chloroperoxidase and glucose oxidase immobilized on SBA-15 as tandem biocatalyst.* Microporous And Mesoporous Materials, 2008. **113**(1-3): p. 523-529.

43.   Holzinger, M., Singh, M., and Cosnier, S., *Biotin-beta-Cyclodextrin: A New Host Guest System for the Immobilization of Biomolecules.* Langmuir, 2012. **28**(34): p. 12569-12574.

44.   Srejber, M., Navratilova, V., Paloncyova, M., et al., *Membrane-attached mammalian cytochromes P450: An overview of the membrane's effects on structure, drug binding, and interactions with redox partners.* Journal Of Inorganic Biochemistry, 2018. **183**: p. 117-136.

45.   Dai, Y.J., Zhen, J., Zhang, X.L., et al., *Analysis of the complex formation, interaction and electron transfer pathway between the "open" conformation of NADPH-cytochrome P450 reductase and aromatase.* Steroids, 2015. **101**: p. 116-124.

46.   Yang, C.Q., Lu, S., Mao, Y.B., et al., *Characterization of two NADPH: Cytochrome P450 reductases from cotton (Gossypium hirsutum).* Phytochemistry, 2010. **71**(1): p. 27-35.

47.   Li, X.H., Zhu, H., Feng, J., et al., *One-pot polylol synthesis of graphene decorated with size- and density-tunable Fe3O4 nanoparticles for porcine pancreatic lipase immobilization.* Carbon, 2013. **60**: p. 488-497.

48.   De Matteis, L., Germani, R., Mancini, M.V., et al., *Encapsulation of chloroperoxidase in novel hybrid polysaccharide-silica biocomposites: Catalytic efficiency, re-use and thermal stability.* Applied Catalysis a-General, 2015. **492**: p. 23-30.

49.   Bayramoglu, G., Kiralp, S., Yilmaz, M., et al., *Covalent immobilization of chloroperoxidase onto magnetic beads: Catalytic properties and stability.* Biochemical Engineering Journal, 2008. **38**(2): p. 180-188.

50.   Perez, D.I., van Rantwijk, F., and Sheldon, R.A., *Cross-Linked Enzyme Aggregates of Chloroperoxidase: Synthesis, Optimization and Characterization.* Advanced Synthesis & Catalysis, 2009. **351**(13): p. 2133-2139.

51.   Wang, W., Xu, Y., Wang, D.I.C., et al., *Recyclable Nanobiocatalyst for Enantioselective Sulfoxidation: Facile Fabrication and High Performance of Chloroperoxidase-Coated Magnetic Nanoparticles with Iron Oxide Core and Polymer Shell.* Journal Of the American Chemical Society, 2009. **131**(36): p. 12892-+.

52.   Wu, L.T., Wu, S.S., Xu, Z., et al., *Modified nanoporous titanium dioxide as a novel carrier for enzyme immobilization.* Biosensors & Bioelectronics, 2016. **80**: p. 59-66.

53.   Palucki, M., Pospisil, P.J., Zhang, W., et al., *Highly Enantioselective, Low-Temperature Epoxidation Of Styrene.* Journal Of the American Chemical Society, 1994. **116**(20): p. 9333-9334.

54.   Kiljunen, E. and Kanerva, L.T., *Chloroperoxidase-catalysed oxidation of alcohols to aldehydes.* Journal Of Molecular Catalysis B-Enzymatic, 2000. **9**(4-6): p. 163-172.

55.   China, H., Okada, Y., and Dohi, T., *The Multiple Reactions in the Monochlorodimedone Assay: Discovery of Unique Dehalolactonizations under Mild Conditions.* Asian Journal Of Organic Chemistry, 2015. **4**(10): p. 1065-1074.

56.   Vold, R.L., Waugh, J.S., Klein, M.P., et al., *Measurement of Spin Relaxation in Complex Systems.* The Journal of Chemical Physics, 1968. **48**(8): p. 3831-3832.

57.   Rea, V., Kolkman, A.J., Vottero, E., et al., *Active Site Substitution A82W Improves the Regioselectivity of Steroid Hydroxylation by Cytochrome P450 BM3 Mutants As Rationalized by Spin Relaxation Nuclear Magnetic Resonance Studies.* Biochemistry, 2012. **51**(3): p. 750-760.

58.   Buyukcelik, A., Yalcin, B., and Utkan, G., *Multidisciplinary management of lung cancer.* New England Journal Of Medicine, 2004. **350**(19): p. 2009-2009.

59.   Jemal, A., Bray, F., Center, M.M., et al., *Global Cancer Statistics.* Ca-a Cancer Journal for Clinicians, 2011. **61**(2): p. 69-90.

60.   Gridelli, C., Rossi, A., Carbone, D.P., et al., *Non-small-cell lung cancer.* Nature Reviews Disease Primers, 2015. **1**.

61.   Ferlay, J., Soerjomataram, I., Dikshit, R., et al., *Cancer incidence and mortality worldwide: Sources, methods and major patterns in GLOBOCAN 2012.* International Journal Of Cancer, 2015. **136**(5): p. E359-E386.

62.   Govindan, R., Page, N., Morgensztern, D., et al., *Changing epidemiology of small-cell lung cancer in the United States over the last 30 years: Analysis of the surveillance, epidemiologic, and end results database.* Journal Of Clinical Oncology, 2006. **24**(28): p. 4539-4544.

63. Travis, W.D., Brambilla, E., and Riely, G.J., *New Pathologic Classification of Lung Cancer: Relevance for Clinical Practice and Clinical Trials.* Journal Of Clinical Oncology, 2013. **31**(8): p. 992-1001.

64. Shi, L., Zhang, B., Sun, X., et al., *MiR-204 inhibits human NSCLC metastasis through suppression of NUAK1.* British Journal Of Cancer, 2014. **111**(12): p. 2316-2327.

65. Adams, J.M. and Cory, S., *The Bcl-2 apoptotic switch in cancer development and therapy.* Oncogene, 2007. **26**(9): p. 1324-1337.

66. Meng, J.R., Fang, B.L., Liao, Y., et al., *Apoptosis Induction by MEK Inhibition in Human Lung Cancer Cells Is Mediated by Bim.* Plos One, 2010. **5**(9).

67. Zhang, L.N., Li, J.Y., and Xu, W., *A review of the role of Puma, Noxa and Bim in the tumorigenesis, therapy and drug resistance of chronic lymphocytic leukemia.* Cancer Gene Therapy, 2013. **20**(1): p. 1-7.

68. Nordigarden, A., Kraft, M., Eliasson, P., et al., *BH3-only protein Bim more critical than Puma in tyrosine kinase inhibitor-induced apoptosis of human leukemic cells and transduced hematopoietic progenitors carrying oncogenic FLT3.* Blood, 2009. **113**(10): p. 2302-2311.

69. Cragg, M.S., Kuroda, J., Puthalakath, H., et al., *Gefitinib-induced killing of NSCLC cell lines expressing mutant EGFR requires BIM and can be enhanced by BH3 mimetics.* Plos Medicine, 2007. **4**(10): p. 1681-1690.

70. Croce, C.M. and Reed, J.C., *Finally, An Apoptosis-Targeting Therapeutic for Cancer.* Cancer Research, 2016. **76**(20): p. 5914-5920.

71. Calnan, D.R. and Brunet, A., *The FoxO code.* Oncogene, 2008. **27**(16): p. 2276-2288.

72. Yang, J.Y., Xia, W., and Hu, M.C.T., *Ionizing radiation activates expression of FOXO3a, Fas ligand, and Bim, and induces cell apoptosis.* International Journal Of Oncology, 2006. **29**(3): p. 643-648.

73. Schmidt, M., de Mattos, S.F., van der Horst, A., et al., *Cell cycle inhibition by FoxO forkhead transcription factors involves downregulation of cyclin D.* Molecular And Cellular Biology, 2002. **22**(22): p. 7842-7852.

74. Medema, R.H., Kops, G.J.P.L., Bos, J.L., et al., *AFX-like Forkhead transcription factors mediate cell-cycle regulation by Ras and PKB through p27(kip1)*. Nature, 2000. **404**(6779): p. 782-787.

75. Tran, H., Brunet, A., Grenier, J.M., et al., *DNA repair pathway stimulated by the forkhead transcription factor FOXO3a through the Gadd45 protein*. Science, 2002. **296**(5567): p. 530-534.

76. Brunet, A., Bonni, A., Zigmond, M.J., et al., *Akt promotes cell survival by phosphorylating and inhibiting a forkhead transcription factor*. Cell, 1999. **96**(6): p. 857-868.

77. Qiang, W., Sui, F., Ma, J.J., et al., *Proteasome inhibitor MG132 induces thyroid cancer cell apoptosis by modulating the activity of transcription factor FOXO3a*. Endocrine, 2017. **56**(1): p. 98-108.

78. Fitzwalter, B.E., Towers, C.G., Sullivan, K.D., et al., *Autophagy Inhibition Mediates Apoptosis Sensitization in Cancer Therapy by Relieving FOXO3a Turnover*. Developmental Cell, 2018. **44**(5): p. 555-+.

79. van der Horst, A. and Burgering, B.M.T., *Stressing the role of FoxO proteins in lifespan and disease*. Nature Reviews Molecular Cell Biology, 2007. **8**(6): p. 440-450.

80. Mcguirk, P.R., Jefson, M.R., Mann, D.D., et al., *Synthesis And Structure-Activity-Relationships Of 7-Diazabicycloalkylquinolones, Including Danofloxacin, a New Quinolone Antibacterial Agent for Veterinary-Medicine*. Journal Of Medicinal Chemistry, 1992. **35**(4): p. 611-620.

81. Knoll, U., Glunder, G., and Kietzmann, M., *Comparative study of the plasma pharmacokinetics and tissue concentrations of danofloxacin and enrofloxacin in broiler chickens*. Journal Of Veterinary Pharmacology And Therapeutics, 1999. **22**(4): p. 239-246.

82. Sappal, R., Chaudhary, R.K., Sandhu, H.S., et al., *Pharmacokinetics, urinary excretion and plasma protein binding of danofloxacin following intravenous administration in buffalo calves (Bubalus bubalis)*. Veterinary Research Communications, 2009. **33**(7): p. 659-667.

83. Qiang, L., Yang, Y., You, Q.D., et al., *Inhibition of glioblastoma growth and angiogenesis by garnbogic acid: An in vitro and in vivo study*. Biochemical Pharmacology, 2008. **75**(5): p. 1083-1092.

84. Zhang, X.P., Chen, J., Graham, S.H., et al., *Intranuclear localization of apoptosis-inducing factor (AIF) and large scale dna fragmentation after traumatic brain injury in rats and in neuronal cultures exposed to peroxynitrite.* Journal Of Neurochemistry, 2002. **82**(1): p. 181-191.

85. Tao, L., Fu, R., Wang, X.P., et al., *LL-202, a newly synthesized flavonoid, inhibits tumor growth via inducing G(2)/M phase arrest and cell apoptosis in MCF-7 humanbreast cancer cells in vitro and in vivo.* Toxicology Letters, 2014. **228**(1): p. 1-12.

86. Abu-Hamad, S., Zaid, H., Israelson, A., et al., *Hexokinase-I protection against apoptotic cell death is mediated via interaction with the voltage-dependent anion channel-1 - Mapping the site of binding.* Journal Of Biological Chemistry, 2008. **283**(19): p. 13482-13490.

87. Zhao, Y., Guo, Q.L., Zhao, K., et al., *Small molecule GL-V9 protects against colitis-associated colorectal cancer by limiting NLRP3 inflammasome through autophagy.* Oncoimmunology, 2018. **7**(1).

88. DeSantis, C.E., Ma, J., Sauer, A.G., et al., *Breast cancer statistics, 2017, racial disparity in mortality by state.* Ca-a Cancer Journal for Clinicians, 2017. **67**(6): p. 439-448.

89. Zheng, R.S., Zeng, H.M., Zhang, S.W., et al., *Estimates of cancer incidence and mortality in China, 2013.* Chinese Journal Of Cancer, 2017. **36**.

90. Picon-Ruiz, M., Morata-Tarifa, C., Valle-Goffin, J.J., et al., *Obesity and Adverse Breast Cancer Risk and Outcome: Mechanistic Insights and Strategies for Intervention.* Ca-a Cancer Journal for Clinicians, 2017. **67**(5): p. 379-397.

91. Pierobon, M. and Frankenfeld, C.L., *Obesity as a risk factor for triple-negative breast cancers: a systematic review and meta-analysis.* Breast Cancer Research And Treatment, 2013. **137**(1): p. 307-314.

92. Bray, F., Ferlay, J., Soerjomataram, I., et al., *Global cancer statistics 2018: GLOBOCAN estimates of incidence and mortality worldwide for 36 cancers in 185 countries.* Ca-a Cancer Journal for Clinicians, 2018. **68**(6): p. 394-424.

93. Warburg, O., *On the origin of cancer cells.* Science, 1956. **123**(3191): p. 309-314.

94. Hanahan, D. and Weinberg, R.A., *Hallmarks of cancer: the next generation.* Cell, 2011. **144**(5): p. 646-674.

95. Zhivotovsky, B. and Orrenius, S., *The Warburg Effect returns to the cancer stage.* Semin Cancer Biol, 2009. **19**(1): p. 1-3.

96. Mathupala, S.P., Ko, Y.H., and Pedersen, P.L., *Hexokinase II: Cancer's double-edged sword acting as both facilitator and gatekeeper of malignancy when bound to mitochondria.* Oncogene, 2006. **25**(34): p. 4777-4786.

97. Hamanaka, R.B. and Chandel, N.S., *Warburg Effect and Redox Balance.* Science, 2011. **334**(6060): p. 1219-1220.

98. Rosano, C., *Molecular model of hexokinase binding to the outer mitochondrial membrane porin (VDAC1): Implication for the design of new cancer therapies.* Mitochondrion, 2011. **11**(3): p. 513-519.

99. Heiden, M.G.V., Cantley, L.C., and Thompson, C.B., *Understanding the Warburg Effect: The Metabolic Requirements of Cell Proliferation.* Science, 2009. **324**(5930): p. 1029-1033.

100. Bustamante, E. and Pedersen, P.L., *High aerobic glycolysis of rat hepatoma cells in culture: role of mitochondrial hexokinase.* Proc Natl Acad Sci U S A, 1977. **74**(9): p. 3735-3739.

101. Pastorino, J.G. and Hoek, J.B., *Regulation of hexokinase binding to VDAC.* J Bioenerg Biomembr, 2008. **40**(3): p. 171-182.

102. Hashimoto, M. and Wilson, J.E., *Membrane potential-dependent conformational changes in mitochondrially bound hexokinase of brain.* Archives Of Biochemistry And Biophysics, 2000. **384**(1): p. 163-173.

103. Patra, K.C., Wang, Q., Bhaskar, P.T., et al., *Hexokinase 2 Is Required for Tumor Initiation and Maintenance and Its Systemic Deletion Is Therapeutic in Mouse Models of Cancer.* Cancer Cell, 2013. **24**(2): p. 213-228.

104. Shulga, N., Wilson-Smith, R., and Pastorino, J.G., *Sirtuin-3 deacetylation of cyclophilin D induces dissociation of hexokinase II from the mitochondria.* Journal Of Cell Science, 2010. **123**(6): p. 894-902.

105. Pastorino, J.G. and Hoek, J.B., *Hexokinase II: The integration of energy metabolism and control of apoptosis.* Current Medicinal Chemistry, 2003. **10**(16): p. 1535-1551.

106. Vara, J.A.F., Casado, E., de Castro, J., et al., *PI3K/Akt signalling pathway and cancer.* Cancer Treatment Reviews, 2004. **30**(2): p. 193-204.

107. Miyamoto, S., Murphy, A.N., and Brown, J.H., *Akt mediates mitochondrial protection in cardiomyocytes through phosphorylation of mitochondrial hexokinase-II.* Faseb Journal, 2008. **22**.

108. Watcharasit, P., Bijur, G.N., Song, L., et al., *Glycogen synthase kinase-3 beta (GSK3 beta) binds to and promotes the actions of p53.* Journal Of Biological Chemistry, 2003. **278**(49): p. 48872-48879.

109. Robey, R.B. and Hay, N., *Mitochondrial hexokinases, novel mediators of the antiapoptotic effects of growth factors and Akt.* Oncogene, 2006. **25**(34): p. 4683-4696.

110. Pastorino, J.G. and Hoek, J.B., *Regulation of hexokinase binding to VDAC.* Journal Of Bioenergetics And Biomembranes, 2008. **40**(3): p. 171-182.

111. Li, L.W., Chen, P., Ling, Y., et al., *Inhibitory effects of GL-V9 on the invasion of human breast carcinoma cells by downregulating the expression and activity of matrix metalloproteinase-2/9.* European Journal Of Pharmaceutical Sciences, 2011. **43**(5): p. 393-399.

112. Li, L.W., Lu, N., Dai, Q.S., et al., *GL-V9, a newly synthetic flavonoid derivative, induces mitochondrial-mediated apoptosis and G2/M cell cycle arrest in human hepatocellular carcinoma HepG2 cells.* European Journal Of Pharmacology, 2011. **670**(1): p. 13-21.

113. Zhao, L., Li, W., Zhou, Y.X., et al., *The overexpression and nuclear translocation of Trx-1 during hypoxia confers on HepG2 cells resistance to DDP, and GL-V9 reverses the resistance by suppressing the Trx-1/Ref-1 axis.* Free Radical Biology And Medicine, 2015. **82**: p. 29-41.

114. Wei, L., Lu, N., Dai, Q., et al., *Different apoptotic effects of wogonin via induction of H(2)O(2) generation and Ca(2+) overload in malignant hepatoma and normal hepatic cells.* J Cell Biochem, 2010. **111**(6): p. 1629-1641.

115. Wei, L.B., Lu, N., Dai, Q.S., et al., *Different Apoptotic Effects of Wogonin Via Induction of H2O2 Generation and Ca2+ Overload in Malignant Hepatoma and Normal Hepatic Cells.* Journal Of Cellular Biochemistry, 2010. **111**(6): p. 1629-1641.

116. He, L.C., Lu, N., Dai, Q.S., et al., *Wogonin induced G1 cell cycle arrest by regulating Wnt/beta-catenin signaling pathway and inactivating CDK8 in human colorectal cancer carcinoma cells.* Toxicology, 2013. **312**: p. 36-47.

117. Xu, X.F., Zhang, Y., Li, W., et al., *Wogonin reverses multi-drug resistance of human myelogenous leukemia K562/A02 cells via downregulation of MRP1 expression by inhibiting Nrf2/ARE signaling pathway.* Biochemical Pharmacology, 2014. **92**(2): p. 220-234.

118. Ganapathy-Kanniappan, S. and Geschwind, J.F.H., *Tumor glycolysis as a target for cancer therapy: progress and prospects.* Molecular Cancer, 2013. **12**.

119. Chiara, F., Castellaro, D., Marin, O., et al., *Hexokinase II Detachment from Mitochondria Triggers Apoptosis through the Permeability Transition Pore Independent of Voltage-Dependent Anion Channels.* Plos One, 2008. **3**(3).

120. Lee, J.E., Kang, J.S., Ki, Y.W., et al., *Akt/GSK3 beta signaling is involved in fipronil-induced apoptotic cell death of human neuroblastoma SH-SY5Y cells.* Toxicology Letters, 2011. **202**(2): p. 133-141.

121. Ma, X.M. and Bai, Y.R., *IGF-1 activates the P13K/AKT signaling pathway via upregulation of secretory clusterin.* Molecular Medicine Reports, 2012. **6**(6): p. 1433-1437.

122. Komurov, K., Tseng, J.T., Muller, M., et al., *The glucose-deprivation network counteracts lapatinib-induced toxicity in resistant ErbB2-positive breast cancer cells.* Molecular Systems Biology, 2012. **8**.

APPENDIX

Figure A1. DNA sequence of full-length WT CPO gene.
ATGTTCTCCAAGGTCCTTCCCTTCGTGGGAGCGGTTGCCGCCCTCCCTCAC
TCCGTCCGTCAGGAGCCTGGCTCCGGCATTGGCTACCCATACGACAACAAC
ACCCTGCCATATGTCGCCCCAGGTCCTACCGACTCTCGTGCTCCTTGCCCAG
CTCTGAACGCTCTTGCCAACCACGGTTACATTCCTCACGATGGCCGTGCCA
TCAGCAGGGAGACCCTCCAGAACGCTTTCCTCAACCACATGGGTATTGCCA
ACTCCGTCATTGAGCTTGCTCTGACCAACGCCTTCGTCGTCTGCGAGTACG
TTACTGGCTCCGACTGTGGTGACAGCCTTGTCAACCTGACTCTGCTCGCCG
AGCCCCACGCTTTCGAGCACGACCACTCCTTCTCCCGCAAGGATTACAAGC
AGGGTGTCGCCAACTCCAACGACTTCATCGACAACAGGAACTTCGATGCC
GAGACCTTCCAGACCTCTCTGGATGTCGTTGCAGGCAAGACCCACTTCGAC
TATGCCGACATGAACGAGATCCGCCTTCAGCGCGAGTCCCTCTCCAACGAG
CTTGACTTCCCCGGTTGGTTCACCGAGTCCAAGCCAATCCAGAACGTCGAG
TCTGGCTTCATCTTCGCCCTTGTCTCTGACTTCAACCTGCCCGACAACGATG
AGAACCCTCTGGTTCGCATTGACTGGTGGAAGTACTGGTTCACCAACGAGT
CCTTCCCATACCACCTCGGCTGGCACCCCCGTCTCCAGCCAGGGAGATCG
AGTTCGTCACCTCCGCCTCCTCCGCTGTCCTGGCTGCCTCTGTCACCTCTAC
TCCATCTTCCCTTCCATCCGGTGCCATCGGCCCAGGTGCCGAGGCTGTCCCT
CTCTCCTTCGCCTCCACCATGACCCCATTCCTCCTCGCCACCAATGCTCCTT
ACTACGCCCAGGACCCAACTCTCGGCCCCAACGACAAGCGTGAGGCTGCC
CCAGCTGCCACCACCTCCATGGCCGTCTTCAAGAACCCATACCTCGAGGCC
ATTGGCACCCAGGACATCAAGAACCAGCAGGCTTACGTCAGCTCCAAGGC
TGCTGCCATGGCCTCTGCCATGGCCGCCAACAAGGCCCGCAACCTTTAA

YONGJIAN GUO

2009-2012	Mississippi College Clinton, Mississippi
2012-2013	B.A., Chemistry Florida International University Miami, Florida
2014-2018	Teaching Assistant Florida International University Miami, Florida
2018-2019	Doctoral Candidate Florida International University Miami, Florida
2018-2019	Research Assistant Florida International University Miami, Florida

PUBLICATIONS AND PRESENTATIONS

Gao, F., Guo, Y., Fan, X., Hu, M., Li, S., Zhai, Q., ... & Wang, X. (2019). Enhancing the catalytic performance of chloroperoxidase by co-immobilization with glucose oxidase on magnetic graphene oxide. *Biochemical engineering journal*, *143*, 101-109.

Guo, Y., Zhao, Y., Zhou, Y., Tang, X., Li, Z., & Wang, X. (2019). LZ-101, a novel derivative of danofloxacin, induces mitochondrial apoptosis by stabilizing FOXO3a via blocking autophagy flux in NSCLC cells. *Cell death & disease*, *10*(7), 484.

Dai, Q., Yin, Q., Wei, L., Zhou, Y., Qiao, C., Guo, Y., ... & Lu, N. (2016). Oroxylin A regulates glucose metabolism in response to hypoxic stress with the involvement of Hypoxia-inducible factor-1 in human hepatoma HepG2 cells. *Molecular carcinogenesis*, *55*(8), 1275-1289.

Tu, J., Xing, Y., Guo, Y., Tang, F., Guo, L., & Xi, T. (2012). TanshinoneIIA ameliorates inflammatory microenvironment of colon cancer cells via repression of microRNA-155. *International immunopharmacology*, *14*(4), 353-361.